

Exploitation of Nonlinear Behavior to Improve the Performance of a Magnetic Sensor

A Thesis
Presented to
The Academic Faculty

by

Stephen Reiman

In Partial Fulfillment
of the Requirements for the Degree
Masters of Science in Mechanical Engineering

School of Mechanical Engineering
Georgia Institute of Technology
April 2004

Exploitation of Nonlinear Behavior to Improve the Performance of a Magnetic Sensor

Approved by:

Professor Wenjing Ye, Advisor

Professor Mark G. Allen
(Electrical and Computer Engineering)

Professor Bert Bras

Date Approved: 9 April 2004

ACKNOWLEDGEMENTS

I would like to thank my adviser, Dr. Wenjing Ye, for all of the help and guidance provided throughout my research. Thanks also to my committee members Dr. Mark G. Allen and Dr. Bert Bras.

I would like to thank Dr. Charles Pezeshki and Dr. Walter Grantham for their discussions with me regarding graduate school.

I would like to thank my parents, Richard and Edda Reiman, for all of their support, encouragement, guidance throughout my life.

Finally, I would like to thank Jesus Christ for all he has done for me.

NOMENCLATURE

Symbol	Definition
\mathbf{A}	vector of coefficients for harmonics in \mathbf{C} for nearby state
ΔA	vector of coefficients for harmonics in \mathbf{C}
A_c	beam cross-sectional area
α	misalignment of the two interacting magnetic fields
B	magnetic field strength
B_{magnet}	Magnetic field strength of the permanent magnet
$B_{external}$	magnetic field strength of external field
BEM	boundary element method
\mathbf{C}	vector of unit of harmonics
C	capacitance between to objects
C_0, C_1, C_2, C_3	coefficients to describe shaped comb drive geometry
Ci_1, Ci_2	desired coefficients for C1 and C2
δ_y	deflection of beam tip in y direction
Δ_{ext}	extension of deflecting beam due to tip motion
Δ_{bend}	change in beam length due to bending
Duffing	Oscillator with linear and cubic stiffness
E	elastic modulus
ϵ_0	permissivity of free space
FEM	finite element method
h	height of sensor and beams
\mathbf{H}	magnetic field near and object
HelmHoltz-Duffing	Oscillator with linear, quadratic, and cubic stiffness
$HBNR$	Harmonic Balance Newton-Raphson
I	polar moment of inertia of magnetic sensor
I_{cf}	inertia of comb finger supports
I_d	inertia of disk
IHB	Incremental Harmonic Balance
I_y	moment of inertia of beam cross-section relative to y-axis
I_m	inertia of magnet
I_z	moment of inertia of beam cross-section relative to z-axis

Symbol	Definition
K_C	cubic coefficient of restoring torques within sensor
K_{CombC}	cubic contribution of a shaped comb drive
K_{CombL}	linear contribution of a shaped comb drive
K_{CombQ}	quadratic contribution of a shaped comb drive
K_{Cp}	cubic coefficient of P
K_{Cs}	cubic coefficient of S
K_L	linear coefficient of restoring torques within sensor
K_{Lp}	linear coefficient of P
K_{Ls}	linear coefficient of S
K_Q	quadratic coefficient of restoring torques within sensor
K_{Qp}	quadratic coefficient of P
K_{Qs}	quadratic coefficient of S
L	beam length
<i>Lateral Deflection</i>	deflection in y-direction
M	restoring torque to M_0
\mathbf{M}	magnetization of a material
M_0	moment at beam-disk interface
M_A	moment at the beam anchor support
M_{AC}	cubic coefficient of M_A
M_{AL}	linear coefficient of M_A
M_{AQ}	quadratic coefficient of M_A
M_C	cubic coefficient of M_0
MEMS	microelectromechanical system
M_L	linear coefficient of M_0
M_Q	quadratic coefficient due to M_0
M_P	restoring torque due to lateral beam stiffness
M_S	restoring torque due to axial beam stiffness
μ	damping coefficient with the sensor
μ_0	permeability of free space
M_y	moment on beam cross-section relative to y-axis
M_z	moment on beam cross-section relative to z-axis
P	lateral deflection force at beam-disk interface
Q-factor	quality factor
R	radius of central disk within sensor
R_m	7 radius of magnet
R_{cf}	radius of comb finger supports
ρ_d	density of silicon structure
ρ_m	density of magnet
S	- axial force at beam-disk interface
SQP	Sequential Quadratic Programming
σ_{bend}	bending stress
σ_{axial}	axial stress
<i>Sens</i>	sensitivity of the magnetic sensor near $\alpha = \pm \frac{\pi}{2}$

Symbol	Definition
T_E	excitation torque due to comb drives
T_L, T_Q	equivalent torque coefficients for shaped comb drives
t_m	thickness of the magnet
T_{mag}	magnetic torque due to magnetic field misalignments
τ	dimensionless variable for IHB solution
θ_0	static equilibrium rotation of disk
θ_d	dynamic rotation of disk due to excitation
θ_{d0}	Nearby steady-state solution to nonlinear vibration of system
$\Delta\theta_d$	incremental change in system response from nearby solution
u	interim variable in the force-deflection derivation of a beam
U_e	potential energy of an electrostatic field
V	Voltage / potential
ν	interim variable for force-deflection derivation for a beam
w	beam width
W	weight of magnet, central disk, and comb drives
ω_0	linear natural frequency
ω_{nb}	nearby excitation frequency in IHB technique

TABLE OF CONTENTS

ACKNOWLEDGEMENTS	iii
NOMENCLATURE	iv
LIST OF TABLES	x
LIST OF FIGURES	xi
SUMMARY	xiv
CHAPTER I : INTRODUCTION	1
CHAPTER II : MEMS SENSORS REVIEW	4
2.1 MEMS resonators	6
2.2 MEMS Magnetic Sensors	6
2.2.1 MEMS Magnetic Resonators	7
CHAPTER III : MAGNETIC SENSOR MODELING	9
3.1 Governing Equations	11
3.2 Component Modeling	12
3.2.1 Beam Mechanics	12
3.2.1.1 Related Work	12
3.2.1.2 Nonlinear Beam Model	13
3.2.2 Inertia	19
3.2.3 Magnetism	20
3.2.4 Comb Drive Excitation	21
3.3 Sensor Dynamics	23
3.4 Linear Vibration	26
3.5 Nonlinear Vibration	28
3.5.1 Incremental Harmonic Balance Method	29
3.5.2 Mechanics Modeling Example	32
3.5.3 Magnetic Sensor Example	35

3.6	Conclusion	38
CHAPTER IV : DESIGN OF PASSIVE SENSOR COMPONENTS		39
4.1	Parameter Sensitivity Study	39
4.2	Beam Geometry Optimization	44
4.2.1	Objective Function	44
4.2.2	Constraints	45
4.3	Results and Conclusion	51
CHAPTER V : DESIGN OF ACTIVE SENSOR COMPONENTS		55
5.1	Related Work	55
5.2	Principles of Shaped Comb Drives	57
5.2.1	Analytical Model Limitations	60
5.3	Application to the Magnetic Sensor	63
5.3.1	Comb Drive Shape Sensitivity Study	64
5.4	Design of a Variable Shaped Comb Drive	69
5.4.1	Shaped Comb Finger Constraints	70
5.4.2	Objective Function	72
5.4.3	Optimization Routine	73
5.5	Results and Conclusion	77
CHAPTER VI : SYSTEM CHARACTERIZATION THROUGH NON- LINEAR VIBRATION		81
6.1	Related Work	82
6.2	Nonlinear Vibration Analysis	84
6.3	Insensitivity to Noise	86
6.4	Insensitivity to Quality-Factor	90
6.5	Technique Applicability	93
6.6	Conclusions	95
CHAPTER VII : CONCLUSIONS AND FUTURE WORK		96
7.1	Conclusions	96

7.2 Future Work	97
APPENDIX A : BEAM DEFLECTION CODE	99
APPENDIX B : EXAMPLE DEVICE DIMENSIONS	101
B.1 Resonator without Magnet	101
B.2 Resonator with Magnet	101
APPENDIX C : OPTIMAL SHAPED COMB DRIVE PARAME- TERS	103
APPENDIX D : MAGNETIC SENSOR OPTIMIZATION CODE WITH SHAPED COMB DRIVE	105
APPENDIX E : INCREMENTAL HARMONIC BALANCE CODE	119
REFERENCES	123

LIST OF TABLES

Table 1	Magnetic Sensor Constraints	50
Table 2	Comparison of Sensor Resolutions.	54
Table 3	System Parameters for a Linear Stiffening Comb Drive.	58
Table 4	System Parameters for a Quadratic Stiffening Comb Drive.	59
Table 5	System Parameters for a Cubic Stiffening Comb Drive.	60
Table 6	System Parameters for a Constant Force Comb Drive.	61
Table 7	Comparison of Sensitivity with Shaped Comb Drive Contributions .	66
Table 8	Shaped Comb Drive Objective Function and Constraints	75
Table 9	Comparison of Sensitivity with Shaped Comb Drive Contributions .	76
Table 10	Comparison of Sensor Resolutions.	79
Table 11	Comparison of Jump-Up Frequencies.	93
Table 12	Significant Device Dimenions	101
Table 13	Significant Device Dimenions	102
Table 14	Gap Parameters for an Optimized Shaped Comb Drive.	104

LIST OF FIGURES

Figure 1	Magnetic Sensor Example.	11
Figure 2	Example of MEMS Resonating Device.	12
Figure 3	Beam Undergoing Deflection, Extension, and Rotation.	13
Figure 4	Free Body Diagram of Beam in Deflection.	13
Figure 5	ANSYS Simulation Results of a Beam Tip Deflecting, Extending, and Rotating.	16
Figure 6	ANSYS Simluation versus Analytical Model.	18
Figure 7	ANSYS Simluation versus Analytical Model: M_0 vs. δ_y	18
Figure 8	Torque Diagram from Magnetic Field Interaction.	20
Figure 9	Geometry of a Constant Gap Comb Drive.	22
Figure 10	Example for Implementation of T_E Curve Fitting.	34
Figure 11	Comparison of Analytical Model to Experimental Data.	35
Figure 12	Simulated Response of Magnetic Sensor.	36
Figure 13	Comparison of System Coefficients versus α	37
Figure 14	K_L versus α	37
Figure 15	Diagram of Beam Dimensions.	40
Figure 16	Comparison of System Behavior with Variations in Width and Height: Sensitivity Curve.	42
Figure 17	Comparison of System Behavior with Variations in Width and Height: Deflection (θ_0).	42
Figure 18	Comparison of System Behavior with Variations in Width and Length: Sensitivity Curve.	43
Figure 19	Comparison of System Behavior with Variations in Height and Length: Sensitivity Curve.	43
Figure 20	Beam Cross-Section with Bending Moments.	46
Figure 21	Free-Body Diagram of a Beam in Z-Axis Bending.	47
Figure 22	Diagram of Z-direction Sensor Motion.	50
Figure 23	Objective Function Results for Sensor Optimization of Beam Height.	51

Figure 24	Comparison of System Performance due to Beam Optimization. . .	52
Figure 25	Scanning Electron Microscope Picture of a Comb Drive Actuator [13].	56
Figure 26	Proposed Addition of Comb Drive Elements to Sensor Design. . . .	56
Figure 27	Linear Comb Drive.	58
Figure 28	Quadratic Comb Drive.	59
Figure 29	Cubic Comb Drive.	60
Figure 30	Insertion Distance Limitation of the Analytical Model.	61
Figure 31	Poor Height Aspect Ratio: Analytical Model versus Numerical Simulation.	62
Figure 32	Limitation of the Analytical Model due to Finger Length: Constant Force Profile.	63
Figure 33	Mass-Spring-Damper Representation of the Magnetic Sensor. . . .	64
Figure 34	Variations in Linear Stiffness.	67
Figure 35	Variations in Quadratic Stiffness.	67
Figure 36	Variations in Cubic Stiffness.	67
Figure 37	Comparison of Changes in Natural Frequency for Multiple Comb Drive Combinations.	68
Figure 38	Gap Constraints for a Shaped Comb Finger.	70
Figure 39	Diagram of Radius Evaluation for Comb Fingers.	71
Figure 40	Flowchart of Comb Drive Optimization Code.	75
Figure 41	Optimal Gap Profile for Sensor in Section 4.	76
Figure 42	Flowchart of Sensor Optimization.	78
Figure 43	Geometric Optimization with Shaped Comb Drives.	79
Figure 44	Frequency Sweeping and Correlation to Jump Phenomena.	84
Figure 45	Frequency versus Orientation of External Field.	86
Figure 46	Vibration Response of Example to Parametric Excitation.	87
Figure 47	Steady-State Response near Resonance with Noise.	88
Figure 48	FFT of Linear Vibration near Resonance with Noise.	88
Figure 49	Steady-State Response near the Jump-Up Frequency with Noise. . .	91
Figure 50	FFT of nonlinear Vibration near the Jump-Up Frequency with Noise.	91

Figure 51	Effect of Damping on Linear Vibration Behavior.	92
Figure 52	Nonlinear Vibration Response of Example System with Variations in Damping.	93
Figure 53	Autocad Drawing of Magnetic Sensor.	102

SUMMARY

While nonlinear behavior in mechanical systems typically degrades the behavior and performance the devices, the presence of system nonlinearities can sometimes improve the quality of the system. A reason for avoiding nonlinearities within a device is the difficulty in controlling the device due to the effects of the nonlinearities on system behavior. However, careful analysis of nonlinear systems can allow for one to take advantage of the nonlinear behavior to improve system performance.

The objective of this thesis is to exploit the use of nonlinearities to enhance system performance, specifically the sensitivity of a micromachined magnetic sensor. The goal for the sensor is to detect the orientation and the strength of the earth's magnetic field, which is on the order of $30 \mu T$. A device design will be presented that is similar to a prototype that has been fabricated by a student within the Electrical and Computer Engineering Department at Georgia Tech. The operating principle of the device is that changes in the orientation and the strength of an external magnetic field will result in changes in the dynamic behavior of the sensor. While previous device provided a proof of the design concept, it was unable to achieve a sensitivity that would allow for its use as a compass. Improvements in the sensitivity of the sensor are achieved through the modeling and optimization of the magnetic sensor. The optimization and redesign of the magnetic sensor will improve the quality of the device and provide another step towards the commercialization of the sensor. A new design that incorporates the use of variable force comb drives will be proposed that will further improve the sensitivity of the device by modifying the dynamic behavior of the sensor.

Another approach that is presented to exploit the nonlinear behavior of the magnetic sensor involves a frequency detection scheme that uses nonlinear vibrations to characterize sensor behavior. Some benefits of this detection technique are that it is insensitive to noise in the vibration of the sensor and is also independent of the damping present within the system. Both of these effects limit the sensor resolution that can be achieved with the use of conventional frequency detection methods. In addition, the implementation of this sensing technique can be readily applied to variety of sensors types without the redesign of a system or the addition of complex components such as vacuum packaging or signal processing electronics.

CHAPTER I

INTRODUCTION

Nonlinear behavior is seen in a variety of engineering systems and can sometimes be detrimental to the behavior of the devices during operation. The design of devices to operate in regions of nonlinearity is generally avoided due to the difficulty implementing control schemes due to such things as the of multiple static equilibrium positions and chaotic behavior in system response. One way to avoid the negative effects of the nonlinearities is to design devices that operate in the regions of linear behavior. While avoiding regions of nonlinear behavior can reduce the complexity of a device model and behavior, some devices have been shown to achieve better performance by taking advantage of the nonlinear system qualities in the system.

The presence of nonlinear behavior was shown to increase the ability of the adaptive controller to converge to the proper plant model in [31]. The use of nonlinear behavior in automotive suspension systems has been shown to increase the performance of shock absorbers as nonlinear dampers are more resistant to compression due to stiffening of the system from the nonlinearities [2]. Adams proposed a methodology to the design of nonlinear system to ensure that the benefits of the nonlinear properties are used to improve system performance as much as possible [2]. Through smart design of the nonlinear behavior it was demonstrated that the consideration of the nonlinearities could result in internal feedback to improve the controllability of certain systems.

The goal of this thesis is to improve MEMS sensors by exploring and taking advantage the nonlinearities in device behavior to increase the resolution and sensitivity

of these devices. The example studied in this thesis is a micromachined magnetic sensor. A prototype was previously constructed in [28] that uses changes in the linear natural frequency to detect changes in the orientation of external magnetic fields. The primary goal of the sensor was to develop a low power magnetic sensor that could be used as a compass to detect the orientation of earth's magnetic field. However, the resolution of the sensor was shown to be poor for resolution of .2618 radians, or 15° , when the sensor was excited to resonance with a voltage of 37.5 V. Increasing the sensitivity of the sensor will allow for the device to be effectively used as a compass to detect the orientation of the earth's magnetic field. The improvement will come through the optimization of system parameters from an improved system model and the addition of a shaped comb drives to modify the nonlinear behavior of the sensor.

This thesis is organized as follows: Chapter 2 will provide a review of the benefits of MEMS technology and present some examples of MEMS sensors that have been developed. Chapter 3 will focus on the development of an analytical model of the magnetic sensor. Chapter 3 will also provide an explanation of how to solve the system model and analyze the response of the sensor to parametric excitation. Chapter 4 will show that increasing the nonlinearity of the sensor device will result in improvements in the performance of the sensor. The chapter will address the optimization of the beam geometry in the sensor to increase the contribution of nonlinearities to system behavior. The addition of shaped comb drives to the sensor to increase system nonlinearity and sensitivity will be presented in Chapter 5. Chapter 6 will look at the use of nonlinear vibration of the sensor as a means to enhance the sensitivity of MEMS resonators. Chapter 7 will summarize the work that is presented in this thesis and present future tasks to be investigated.

Some expected contributions from this thesis are:

- The development of an analytical model of a micromachined resonant magnetic

sensor.

- The use of shaped comb drives to enhance the performance of the magnetic sensor by increasing the nonlinear behavior of the sensor.

- Proposal of frequency sensing technique that uses nonlinear vibration as a means of improving sensor resolution. The technique will make the system characterization less sensitive to noise and also reduce the dependence of resolution on the damping present in the system.

CHAPTER II

MEMS SENSORS REVIEW

Substantial research is being conducted to make use of MEMS technology to improve the performance of sensors by providing a higher precision of measurement over current technology. This chapter will provide an overview of the benefits of the application of MEMS technology to improve the ability to detect a wide variety of physical properties over conventional macro-scale sensors. Many types of MEMS sensors have been developed that are able to detect a wide range of physical properties such as surface imaging [36], frequency-selective filters for communications applications [38], optical scanners [19], magnetometers [5], and accelerometers [33]. A review of magnetic resonators will also be presented to highlight the disadvantages of pursuing further research in devices other than the sensor in [28] to increase performance through improved modeling and optimization.

Because of the small dimensions of MEMS devices, they are often able to achieve more precise measurements than their macro-scale counterparts. Due to their small masses and feature sizes, MEMS sensors are able to detect very small changes in system parameters such as the adhesion of individual molecules to their surface. A further benefit of the small dimensions of MEMS devices is the ability to measure the properties of macro-scale objects without significantly modifying the behavior of the object due to their presence.

Additionally, MEMS technology possesses the ability to construct the mechanical elements of a sensor on the same silicon chip as the electrical circuits that will be used to process changes in the mechanical elements. By implementing complementary metal oxide semiconductor, CMOS, compatible principles and processes it

is possible to construct the mechanical element of a MEMS device on the same chip as the electrical components of the device [9]. The inclusion of mechanical structures and electrical circuits on the same chip can reduce the overall complexity of the device and the manufacturing process required to fabricate the device. The ability to fabricate both mechanical and electrical components on the same base also allows for batch fabrication of MEMS devices which leads to further cost reductions in the manufacturing of the devices.

Despite the potential for cost reductions, the current development of MEMS technology has required large investments in research and development in order to gain insight and understanding on how devices work on the micro-scale. Due to the behavior of materials on the micro-scale it is often inefficient to scale down system components from the macro-world for use in the MEMS devices. Different structures and techniques are often used instead of macro-scale concepts to achieve the same type of system functionality on the micro-scale level. By designing components specifically for the micro-scale, it is possible to exploit material and geometric behavior that would not be functional on the macro-scale. Brenner developed a new type of MEMS torsional spring for use to measure small torques in MEMS devices that would not be efficient if constructed on the macro-scale [10]. The unconventional spring would be cumbersome and inefficient on the macro-scale; however on the micro-scale it is more effective than the typical torsional springs used within macro-scale systems. By implementing tensural pivots, Masters was able to develop a new mechanism for use in micro-scale switching applications that would achieve the same motion as a macro-scale pivot without the requirement for complex fabrication techniques or performance reduction if the macro-scale pivot had been applied on the micro-scale [34].

2.1 MEMS resonators

Silicon resonators have been used in a wide variety of MEMS applications as sensors for a variety of physical properties and have the potential for much higher sensitivity than standard analog deformation sensors especially when applied to MEMS sensors [44]. Another advantage of resonant sensors is that they can be readily integrated with digital electronics and digital signal processing techniques because of the periodic nature of vibrations. One example of the use of MEMS resonators to detect changes in the surrounding environment is use as a pressure sensor [14]. A variety of MEMS chemical sensors have also been developed that measure changes in resonant frequencies through changes in mass as molecules attach to the surface of the resonating device [47]. Vibration has also been used in position sensors to scan a surface and characterize the features located on the surface [15]. Resonant behavior has also been used in the development of quartz temperature sensors that use vibration as a means of thermal detection [27].

2.2 MEMS Magnetic Sensors

Many different types of devices have been developed to detect the strength and direction of electromagnetic fields [30]. One device uses the Hall effect of plasma electrons as a means of detecting magnetic field strength [43]. Another technique makes use of Lorentz forces such that the external magnetic field interacts with a current carrying U shaped-cantilever loop and causes it to deflect. Strain gages located near the cantilever anchors are used to measure the deflection caused by the external field [5]. The main disadvantage of this sensor for commercialization is the large amount of power required for deformation of the cantilever to occur. Another technique has been presented that measures the static deformation of elements in the sensor due to interactions of external fields with ferromagnetic materials within the device [5]. The advantage of this sensor is that no power is required to generate the magnet field

located on the sensor and the signal processing circuit is the only portion of the device that requires electrical power during operation. However, the resolution of the device is fairly low due to the low sensitivity of the strain gages used to measure deflections.

2.2.1 MEMS Magnetic Resonators

Resonant techniques have also been applied to magnetic sensors to increase the sensitivity of the devices and improve their resolution. A resonant detection technique was used in [29] to measure the magnetic properties of an external magnetic field that involved relating changes in the stiffness of a cantilever beam to properties of the external field. This technique was shown to result in much higher resolutions than with the detection of static deformation with strain gages [5]. The results of the paper show that sensing changes in the resonant frequency of the sensor will result in dramatically improved sensor resolution over the direct measurement of static deflection to detect variations in magnetic field properties.

The device presented in [8] makes use of magnetostrictive materials built into the surface of a device to cause the deformation of the structure. A magnetostrictive material is a material that elastically deforms in the presence of a magnetic field. By subjecting the device to magnetic fields at different orientations, the authors were able to vary the axial and torsional modes of vibration of the device. The disadvantage of this application is that the external magnetic field properties will not consistently affect the same mode of the device, which means that no precise comparison can be made with the sensor behavior that directly relates to changes in the magnetic field properties.

Another type of MEMS device that has been developed to sense magnetic properties through vibration makes use of a magnetized ferromagnetic bar supported by two torsional beams [52]. When the permanent magnet is exposed to an external magnetic field, the interaction causes a change in the angular orientation of the magnet which

is directly related to the external magnetic field. The rotation of the magnet causes a change in the strain of the beams which is detected through changes in the resonant frequency of the system. Properties of the external magnetic field such as direction and magnitude can be determined based upon the frequency response of the system.

A similar device was presented in [28] that used deflection of beams due to forces applied to their tip instead of the torsional behavior of the beams within the magnetic resonator. The advantages of this device are that it is simple to modify the stiffness coefficients of the beams through changes in the length, width and height of the beams and also to modify other parameters of the sensor through design. Further research in the modeling and design of this device has been performed in order to improve its sensitivity beyond what was achieved in [28].

A few of the benefits of the use of MEMS devices have been presented that show the need to pursue improvements in the sensitivity of MEMS devices as sensors. At the present time most devices within the literature are in the prototype phase and suffer from complex fabrication processes and low performance that prevent the mass commercialization of the devices.

CHAPTER III

MAGNETIC SENSOR MODELING

Among various modeling and simulation approaches available, analytical models are often preferred because of the physical insights one can quickly gain from them. By investigating the analytical model of a system, one may quickly see the dependence of system response on multiple variables and adjust them accordingly to achieve desired performance improvement without the expense of running simulations. It is particularly important to have an analytical model in the early stage of the design process when the effects of different design parameters on system responses needs to be determined quickly.

Generating analytical models for MEMS systems can prove to be difficult due to the need for multi-physics modeling to analyze the performance of the devices. It is not uncommon for a device to include the coupling of electrostatic, structural, thermal and fluidic effects. One way to solve is through the use of finite element, FEM, or boundary element methods, BEM. There are many commercial packages available that are able to handle multi-physics problems of varying complexity. Some are well suited to handle complex models with only a few physical effects are models together such as thermal and fluidic analysis and also structural analysis coupled with electromagnetics due to the techniques that are used to model and solve the FEM or BEM simulations.

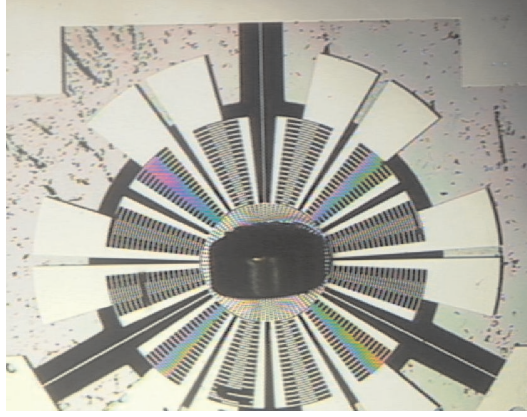
If individual components within a device do not experience coupling between multiple physical properties, combining analytical models each of the components together can allow for their contributions on system behavior to be easily seen within an analytical model. Another major advantage of this approach over numerical methods

is the speed at which the solution for system behavior can be found. Due to the reduction of variables used to describe system behavior, solutions can typically be found faster with the use of analytical models than with FEM or BEM simulations.

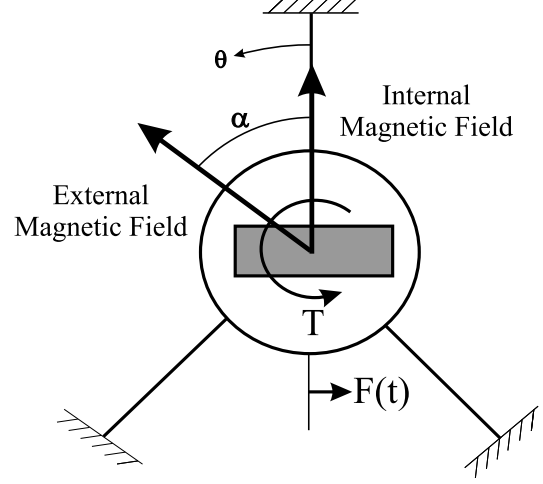
Individual modeling of the various components within the magnetic sensor is possible because the coupling between different physical properties is weak. The technique can be applied since there are no components within the sensor that require multi-physics modeling, but instead the component behaviors only involve structural, electrostatic, and electromagnetic effects. By modeling the elements separately and then combining the torsional effects of the elements together into a common dynamics equation, it is possible to determine device behavior with fewer terms in the base equation and quickly see how changes to different components of the model will affect system performance.

The quicker simulation time is related to a reduction of the number of variables within the system equation and the ability to evaluate the behavior of different components separate from the overall system simulation. Since the behavior of system components can be analyzed individually, a change in one component does not require repeating the computations to determine the behavior of the rest of the components within the model. This approach helps to speed up investigation of changes of system parameters on the behavior of the device by reducing the number of computations that must be performed during each simulation iteration.

By simplifying the model and developing an equation of torques on the system, the sensor from [28] shown in Figure 1(a) can be modeled as a HelmHoltz-Duffing oscillator [42]. The behavior of the sensor beams can be represented as nonlinear springs within the sensor model. The electromagnetic effects of the magnetic field interactions are modeled as a variable torques in the dynamic equation. The electrostatics effects of the comb drives are represented as an excitation torque on the



(a) Picture of Magnetic Sensor to be Modeled.



(b) Magnetic Sensor Diagram.

Figure 1: Magnetic Sensor Example.

system. By solving for the complex behavior of the components separately and applying their solutions to a conventional dynamic equation, it is easier to solve for system behavior through the use established techniques present in the literature.

3.1 Governing Equations

The magnetic sensor studied in this thesis uses the rotational mode of vibration to detect the changes in the resonant behavior of the device due to changes in the external magnetic field. To model the torsional mode of vibration for the sensor, the rotation of the central disk will be used as the generalized coordinate for the model. The dynamics equation for torsional motion of the sensor as shown in Figure 1(a) is:

$$I \cdot \frac{d^2\theta}{dt^2} + \mu \cdot \frac{d\theta}{dt} + K_L \cdot \theta + K_Q \cdot \theta^2 + K_C \cdot \theta^3 = T_E(t) + T_{mag}(\alpha, \theta), \quad (1)$$

where K_L is the linear stiffness, K_Q is the quadratic stiffness coefficient, and K_C is the cubic stiffness coefficient due to the beams in the sensor. I is the polar moment of inertia of the sensor, μ is the damping coefficient of the system and T_{mag} is torque that is applied to the disk from magnetic field interactions and is a function of the external field orientation, α , and the rotation of the sensor, θ . The magnitude of T_E

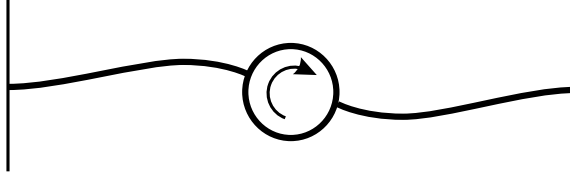


Figure 2: Example of MEMS Resonating Device.

is related to the actuation torque due to the comb drives used to excite the system into vibration.

It is very difficult to model damping within engineering systems due to the many sources of energy losses that are present. Structural damping within the silicon and viscous damping from air are the main sources of energy loss within MEMS devices and expected to effect the behavior of the magnetic sensor [9]. Thermal and acoustic energy can also be lost as the system resonates and are also difficult to model both analytically and numerically. Therefore the value for the damping coefficient μ will be found experimentally.

3.2 Component Modeling

3.2.1 Beam Mechanics

3.2.1.1 *Related Work*

Clamped-clamped beams are commonly used as structural and spring elements within MEMS and accurate modeling of nonlinear behavior of the beams is crucial in determining the performance of MEMS devices. A unique feature about the beams used in MEMS applications is that a geometrical nonlinearity is often present in the behavior of the beams while the material still stays in the linear regime. One end of the beam is often attached to a fixed anchor point while the other is attached to a moving structure as shown in Figure 2.

The existing literature for beams primarily focuses on the study of cantilever beams and few studies have been done to model the performance of beams with

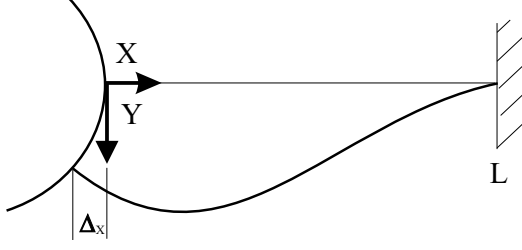


Figure 3: Beam Undergoing Deflection, Extension, and Rotation.

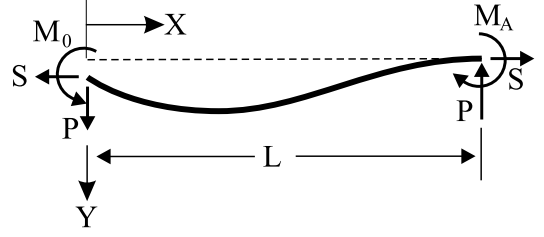


Figure 4: Free Body Diagram of Beam in Deflection.

clamped-clamped boundary conditions. Bisshop used approximations of elliptic integrals to solve for the large deflection behavior for a cantilever beam with a load at its tip [7]. Changes in behavior for a beam that was initial deflected and extended was investigated in [49]. Frisch-Fay developed an analytical model for a clamped-clamped beam in deflection [18]. However, no consideration was taken for a change in rotation of the beam at a boundary or an extension of the beam tip. There has been no work present in the literature for an analytical model of a beam undergoing deflection, extension and tip rotation concurrently. A model will be presented to describe the behavior of a beam that undergoes the extension, rotation, and lateral deflection of its moving tip which represents the behavior of the beams within the magnetic sensor.

3.2.1.2 *Nonlinear Beam Model*

Figure 3 shows a diagram of the beams from the magnetic sensor in [28]. Each beam in the figure is simultaneously undergoing deflection, extension, and tip rotation caused by the rotation of the disk. The linear model of force versus deflection is sufficient when the beam undergoes deflections that are much less than its width. However, when a beam undergoes deflection the same order as its width, a nonlinear model must be developed to incorporate the contribution of axial forces to the deformation of the beam. The coordinate that will be used to describe the behavior of the beams is the lateral deflection, δ_y , of the beam tip. This approach will allow for the

development of a relationship between the moment, axial force, and lateral forces at the beam tip with its linear deflection. In Section 3.3 the relationships will be converted for use with in describing beam behavior as it relates to the rotation of the sensor by:

$$\delta_y = R \cdot \sin(\theta) \quad (2)$$

where R is the radius of the disk within the sensor that supports the magnet and θ is the rotation of the disk.

A clamped-clamped beam that experiences deflection as shown in Figure 3 will experience a larger axial force than a cantilever beam that undergoes similar deflection [18]. Due to the small ratio between the deflection and the length of the beam, linear elastic material properties are assumed and the Bernoulli-Euler model is used to describe the deformation of the beam. Since the deflection of the beam is much less than its length, superposition can be used to combine the effects of the force required to deflect the beam tip and the moment needed to maintain the boundary conditions. For deflections where axial deformation is negligible it is possible to neglect the contribution of axial forces to beam curvature. The beam is modeled as a prismatic beam that is composed of an isotropic, linear elastic material. The width of the beam is much less than the length of the beam therefore it is assumed that there is no shear deformation in the planes of bending.

The equation of motion for the beam is developed from the free body diagram shown in Figure 4, which is:

$$M_0 = EI_z \frac{\partial^2 \delta_y}{\partial x^2} = S \cdot \delta_y + M_A - P(L - x), \quad (3)$$

where I_z is the moment of inertia for the cross-section of the beam and δ_y is the deflection of the beam in the y direction. The moment of inertia for a rectangular cross-section of width w and height h is:

$$I_z = \frac{1}{12} \cdot w \cdot h^3. \quad (4)$$

The beam is modeled as having clamped-clamped boundary conditions therefore the rotation of the tip of the beam is the same as that of the disk. The boundary conditions for the beam in Figure 3 are:

$$y(x)|_{x=L} = 0 \quad (5)$$

$$\frac{\partial y}{\partial x}|_{x=L} = 0 \quad (6)$$

$$y(x)|_{x=0} = \delta_y \quad (7)$$

$$\frac{\partial y}{\partial x}|_{x=0} = \frac{\delta_y}{\sqrt{R^2 - \delta_y^2}}. \quad (8)$$

The general solution to (3) is:

$$y(x) = C_1 \cdot \sinh(\nu \cdot x) + C_2 \cdot \cosh(\nu \cdot x) + \frac{P \cdot (L - x) - M_A}{S} \quad (9)$$

where $\nu = \sqrt{\frac{S}{EI}}$.

By substituting boundary conditions into equation (9), the unknowns C_1 , C_2 , and M_A can be expressed in terms of δ_y , P , and S and an equation that relates δ_y , P , and S results through the solution of the unknowns. In order to obtain a relationship solely between P and δ_y or S and δ_y , an additional equation that relates S , P , and δ_y must be established. This equation is found by considering the relationship between the axial forces, S , and the axial strain developed from deformation.

The length of the beam, L , after deformation can be calculated by applying the arc length formula:

$$L = \int_0^{L_0 + \Delta_{ext}} \sqrt{1 + \left(\frac{dy}{dx}\right)^2} dx, \quad (10)$$

where L_0 is the original length of the beam and Δ_{ext} is the horizontal displacement of the tip caused by the rotation, which can be calculated as $\Delta_{ext} = R - \sqrt{R^2 - \delta_y^2}$. With the assumption of $\frac{dy}{dx} \ll 1$ the beam length can be approximated as:

$$L = L_0 + \Delta_{ext} + \frac{1}{2} \int_0^{L_0 + \Delta_{ext}} \left(\frac{dy}{dx}\right)^2 dx. \quad (11)$$

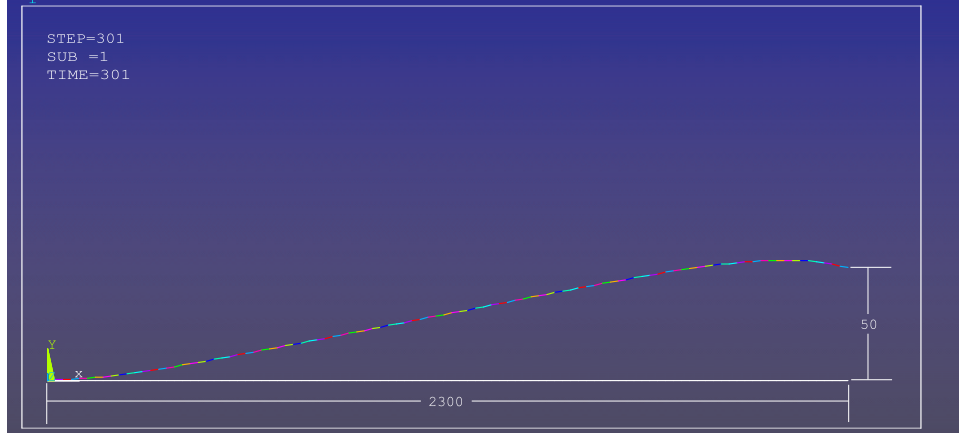


Figure 5: ANSYS Simulation Results of a Beam Tip Deflecting, Extending, and Rotating.

The third term in equation (11) is the change in the beam length due to bending. It can be further simplified as

$$\Delta_{bend} = \frac{1}{2} \int_0^{L_0} \left(\frac{dy}{dx} \right)^2 dx. \quad (12)$$

Thus, the total change in beam length is:

$$\Delta = \Delta_{bend} + \Delta_{ext} = \frac{1}{2} \int_0^L \left(\frac{dy}{dx} \right)^2 dx + R - \sqrt{R^2 - \delta_y^2}. \quad (13)$$

S is modeled as acting through the centroid of cross-sectional area of the beam and constant throughout the length of the beam, is related to the axial strain through the following relationship:

$$S = \frac{A_c \cdot E \cdot \Delta}{L}, \quad (14)$$

where A_c is the area of the beam cross-section and E is the elastic modulus of the beam material. This equation combined with the equation derived from (9) to generate a relationship that is solely between P and δ_y . The relationships between S , M_0 , M_A and δ_y can then be found using the relationship for P that has been developed.

A simulation was developed in ANSYS to verify the developed analytical model. Since ANSYS does not use beam behavior approximations in the same fashion as

the analytical model, it is possible to investigate the error induced in the model due to linear approximations by comparing beams of similar properties. The ANSYS simulations made use of the large deflection static solver to develop the relationships of P , S , and M_0 with δ_y .

Multiple static simulations were run in ANSYS for a beam with dimensions ($h \times w \times L$) of $140 \mu m \times 20 \mu m \times 2300 \mu m$ to compare with the analytical method. The material used in the model has an elastic modulus of 4.5 GPa, which is similar to Su-8 as used in [45]. To reduce the effect of numerical error on the solution results, the beam was simulated on the micron scale and the beam dimensions were entered as $140 \times 20 \times 2300$. The elastic modulus was also scaled to the micron scale and entered as $4.5 * 10^3$. The *beam3* element was used in the simulation due to its tension, compression and bending simulation capabilities, which are the primary physical effects within the beam. A convergence study was done to determine the minimal amount of beam elements that would be needed in the simulation to simulate the behavior of the beam. It was found once the beam was simulated with 100 elements there was no noticeable change in the values for P , S , and M_0 when the number of elements was further increased. Therefore it was decided to use 100 elements to simulate the beam since the solution time was found to greatly increase when the number of elements increased. The beam tip attached to the stationary anchor was modeled as ideally clamped and underwent no change in position or rotation during the simulation. Within each ANSYS iteration, the deflection of the tip of the beam was entered into the simulation and the value for P , S , and M_0 required to achieve the deflection were recorded. Figure 5 shows an example of the beam as simulated within ANSYS and all dimensions are in microns.

The relationship of P to the lateral beam deflection δ_y was developed using the data collected from the simulation and can be seen in Figure 6(a). A comparison of the results for S versus δ_y and M_0 versus δ_y are shown in Figures 6(b) and 7

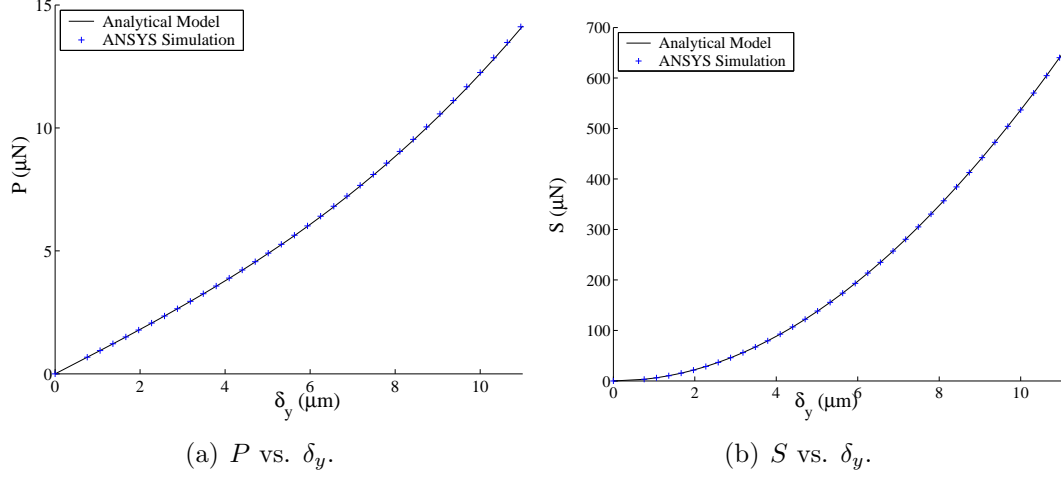


Figure 6: ANSYS Simulation versus Analytical Model.

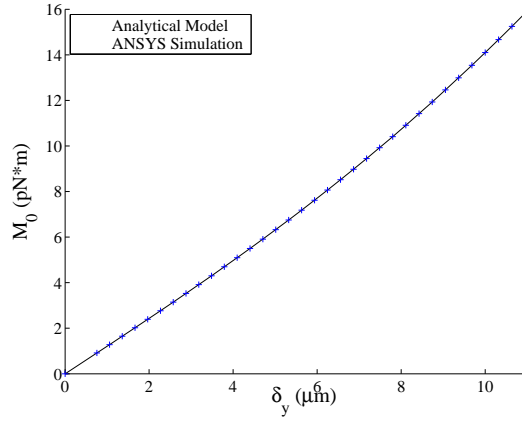


Figure 7: ANSYS Simulation versus Analytical Model: M_0 vs. δ_y .

respectively. Even though the beam experiences linear elastic behavior of the material, the nonlinear stiffness present in the beam can clearly be seen in the figures. The maximum difference of between the lateral force P predicted by the two methods is 0.52%. The maximum differences are .7% and .12% for S and M_0 respectively. Due to the agreement of the analytical solution to the ANSYS simulation, this beam model was used to generate a MATLAB function that would determine the coefficients for a polynomial relationship of P , S , and M_0 and δ_y for use in the magnetic sensor model where:

$$P = K_{Lp}\delta_y + K_{Qp}\delta_y^2 + K_{Cp}\delta_y^3 \quad (15)$$

$$S = K_{Ls}\delta_y + K_{Qs}\delta_y^2 + K_{Cs}\delta_y^3 \quad (16)$$

$$M_0 = M_L\delta_y + M_Q\delta_y^2 + M_C\delta_y^3 \quad (17)$$

3.2.2 Inertia

Since the torsional mode of vibration is used within the magnetic sensor to sense changes in the orientation of the external magnetic field, the rotational moment of inertia is used in the dynamic equation of system behavior in place of sensor mass. The rotational moment of inertia for the sensor is the sum of the moments from the magnet, central disk, comb drives. The moment of inertia of the springs has been calculated to be much smaller than the rest of the sensor and is ignored.

The moment of inertia for the magnet is based upon equation for a cylinder such that [21]:

$$I_m = \frac{\rho_m \cdot \pi}{12} \cdot R_m^2 \cdot t_m (3 \cdot R_m^2 + t_m^2), \quad (18)$$

where ρ_m is the density of the magnetic, R_m its radius, and t_m is its thickness.

The moment of inertia of the disk supporting the magnet is:

$$I_d = \frac{\rho_d \cdot \pi}{2} \cdot h \cdot R^4, \quad (19)$$

where ρ_d is the density of the silicon structure, h is the height of the structure, and R is the radius of the central disk that supports the magnet.

The contribution of the comb drives to the moment of the inertia of the system is found by analyzing the effects of the comb fingers separately from the comb finger supports. The twelve comb drives located on the sensor are of equal radius and are modeled together as $\frac{1}{10}$ of a ring. The combined inertia for the comb drive supports is:

$$I_{cf} = \frac{\rho_d \cdot \pi}{10} \cdot h (R_{cf}^4 - R^4), \quad (20)$$

where R_{cf} is the outer radius of the comb finger supports.

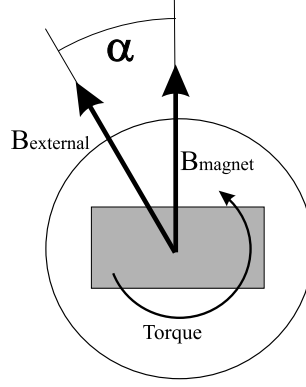


Figure 8: Torque Diagram from Magnetic Field Interaction.

There are eighteen comb fingers in each comb drive and the effective moments of inertia found in a fashion similar as the inertia to the supports such that:

$$\sum_{I=1}^{18} I_{fI} = \frac{8 \cdot \rho_d \cdot \pi}{15} \cdot h \left(R_{oI}^4 - R_{iI}^4 \right), \quad (21)$$

where R_{iI} and R_{oI} are the inner and outer radii of each finger, and $\frac{8}{15}$ is the portion of a complete ring the the comb fingers represent when the contributions from the eight comb drives are added together.

The total moment of inertia of the system is the sum of inertias of the components and is:

$$I = I_m + I_d + I_{cf} + \sum_{I=1}^{18} I_{fI} \quad (22)$$

3.2.3 Magnetism

The purpose of modeling the magnetic behavior in the system is to relate the magnetic field interaction into mechanical torque that will modify the behavior of the sensor.

The magnetic field strength of an object is given by [26]:

$$B = \mu_0 (\mathbf{M} + \mathbf{H}). \quad (23)$$

In this equation μ_0 represents the permeability of free space, \mathbf{M} is the magnetization material, and \mathbf{H} is the magnetization of the object.

When the magnetic field of the magnet interacts with an external field a torque is generated such that the sensor magnet attempts to align itself with the external field such that:

$$T_{mag} = B_{magnet} \cdot B_{external} \cdot \sin(\alpha) = T \sin(\alpha - \theta) \quad (24)$$

where α is the angle between the two magnetic fields as shown in Figure 8. The value of T can be calculated based upon the magnetic properties of the material and equation (23), but has shown substantially vary from the values found from experiment [28]. Magnets of the same type as used in [28] will be used within the magnetic sensor described in this thesis. Therefore for the purposes of modeling within this thesis, a value of $7.2 \times 10^{-8} \text{ N} \cdot \text{m}$ will be used to represent the magnitude of the torque due to magnetic field interaction, which is the value that was experimentally determined in [28].

3.2.4 Comb Drive Excitation

The excitation elements of the magnetic sensor that drive it into resonance and constant force comb drives. The physical principle behind comb drive operation is that the electrostatic attraction between two bodies of different charge will cause a force to develop between them. The force from the interaction is related to the voltage across the two bodies and can be derived from the stored potential energy in the electrostatic field of the system such that [46]:

$$U_e = \frac{1}{2} \cdot C \cdot V^2 \quad (25)$$

where C is the capacitance between the two bodies and V is the voltage. The force exerted between the bodies is the gradient of (25) such that:

$$F = -\nabla U_E \quad (26)$$

For the lateral motion of the two body sets that are seen in a comb drive, the

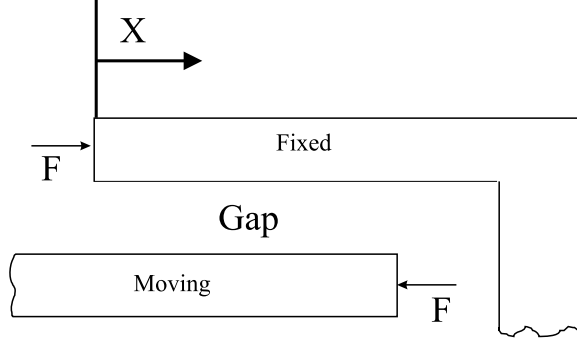


Figure 9: Geometry of a Constant Gap Comb Drive.

approximate force within for a comb drive is [51]:

$$F \approx \epsilon_0 \frac{h \cdot V^2}{gap} \quad (27)$$

where ϵ_0 is the permissivity of free space, h is height of the overlap between the two bodies, and gap is the perpendicular distance of the overlap. The variable h used to describe the force of the comb drives is the same as the height of the disk within the device due to the fabrication method used for the magnetic sensor. The analytical model has been validated through both simulation and experiments in [25].

By applying a harmonic voltage across a comb drive, the resulting force generated by the comb drive will also be harmonic. However, the frequency of the applied force will vary from that of the input voltage. Frequency doubling will be seen when a sinusoidal voltage is applied to the comb drive. This behavior can be seen by substituting the sine signal into to equation(27) with the application of trigonometric identity:

$$\sin^2(\omega \cdot t) = \frac{1}{2} + \frac{\cos(2\omega \cdot t)}{2} \quad (28)$$

Therefore the excitation force of comb drive drive with constant gap can be modeled as:

$$F(t) = \epsilon_0 \frac{h \cdot \sin^2(\omega \cdot t)}{gap} = \epsilon_0 \frac{h \cdot (1 + \cos(2\omega \cdot t))}{2 \cdot gap}. \quad (29)$$

The excitation torque is related to comb drive force and the radius of the central disk

in the sensor such that:

$$T_E(t) = F(t) \cdot R. \quad (30)$$

3.3 Sensor Dynamics

Now that all of the components within the sensor have been modeled separately, the results from each model can be combined into an equation to predict the dynamic behavior of the magnetic sensor during harmonic excitation. The base equation for the dynamics of the magnetic sensor with comb drive excitation is:

$$I \cdot \frac{d^2\theta_d}{dt^2} + \mu \frac{d\theta_d}{dt} + 3 \cdot (T_p + T_s + M_0) = T_E(t) + T_{mag}(\alpha, \theta_0, \theta_d), \quad (31)$$

where T_p , T_s , and M_0 are the restoring torques in the system due to the beams within the device and:

$$T_p = [K_{Lp}R \sin(\theta) + K_{Qp}R^2 \sin^2(\theta) + K_{Cp}R^3 \sin^3(\theta)] R \cos(\theta) \quad (32)$$

$$T_s = [K_{Ls}R \sin(\theta) + K_{Qs}R^2 \sin^2(\theta) + K_{Cs}R^3 \sin^3(\theta)] R \sin(\theta) \quad (33)$$

$$M_0 = M_L R \sin(\theta) + M_Q R^2 \sin^2(\theta) + M_C R^3 \sin^3(\theta) \quad (34)$$

The sources for K_{xP} , K_{xs} , and M_x are the coefficients from the beams within the sensor derived in Section (3.2.1.2).

For a specified magnetic torque, the system will reach an equilibrium angle, θ_0 , such that the restoring torque of the beams will balance the torque exerted by the magnetic field interactions. The equation to determine the static equilibrium angle of the system is:

$$0 = T \cdot \sin(\alpha - \theta_0) - 3 \cdot R \cdot (K_L \cdot (\theta_0) + K_Q (\theta_0)^2 + K_C \cdot (\theta_0)^3), \quad (35)$$

where T is the magnitude of the magnetic torque and the values of K_L , K_Q , and K_C are the stiffness of the sensor related to the spring elements of the sensor through a combination of the results from equations (32), (33), and (34).

The value for θ_0 that satisfies the equation can be found through a numerical root finding technique such as the Bisection method, Fibonacci method, or the method of Golden Sections [4]. The equation has been implemented in MATLAB with the use of the *fzero* function which uses a combination of bisection, secant, and inverse quadratic interpolation search techniques to solve for the equilibrium angle for a specific orientation and magnitude of the external magnetic field [35].

The initial rotation of the disk modifies the behavior of the magnetic sensor and its effects must be included in the dynamic equation for the sensor. The substitution of $\theta = \theta_d + \theta_0$ is made in equation (31) to account for the effects of the static rotation on the dynamic behavior of the sensor where θ_d is the rotation of the central disk due to system excitation with respect to its static equilibrium position of θ_0 . The dynamic equation of the sensor becomes:

$$I \cdot \frac{d\theta_d^2}{dt^2} + \mu \cdot \frac{d\theta_d}{dt} + 3 \cdot (T_P + T_S + M_0) = T_E(t) + T_{mag}(\alpha, \theta_0, \theta_d). \quad (36)$$

The corresponding values for the restoring torques in the sensor are:

$$\begin{aligned} T_p &= \left[K_{Lp} R \sin(\theta_d + \theta_0) + K_{Qp} R^2 \sin^2(\theta_d + \theta_0) + K_{Cp} R^3 \sin^3(\theta_d + \theta_0) \right] R \cos(\theta_d + \theta_0) \\ T_s &= \left[K_{Ls} R \sin(\theta_d + \theta_0) + K_{Qs} R^2 \sin^2(\theta_d + \theta_0) + K_{Cs} R^3 \sin^3(\theta) \right] R \sin(\theta_d + \theta_0) \\ M_0 &= M_L R \sin(\theta_d + \theta_0) + M_Q R^2 \sin^2(\theta_d + \theta_0) + M_C R^3 \sin^3(\theta_d + \theta_0) \end{aligned}$$

Substitution of the new equations for M_p , M_s , and M into (36) will result in a highly nonlinear equation containing many *sine* and *cosine* terms after full expansion of the squared and cubic terms. The resulting equation is simplified through the substitution of the Taylor series expansions of *sine* and *cosine* to the equation.

The Taylor expansion of *sine* is:

$$\sin(x) = \sum_{n=0}^{\infty} \frac{(-1)^n}{(2 \cdot n + 1)!} x^{2 \cdot n + 1} \quad (37)$$

and the corresponding Taylor expansion of *cosine* is:

$$\cos(x) = \sum_{n=0}^{\infty} \frac{(-1)^n}{(2 \cdot n)!} x^{2 \cdot n} \quad (38)$$

The first two terms of the expansions are substituted in (36) and the values for *sine* and *cosine* become:

$$\begin{aligned} \text{sine}(\theta) &= \theta - \frac{\theta^3}{3!} \\ \text{cosine}(\theta) &= 1 - \frac{\theta^2}{4!} \end{aligned}$$

For small values of θ_d and θ_0 , higher orders θ_d and θ_0 greater than cubics can be ignored. However, the small angle assumption does not mean that nonlinearities will not affect the dynamic behavior of the sensor. The final form of the dynamics equation for the magnetic sensor is:

$$I \cdot \frac{d\theta_d^2}{dt^2} + \mu \cdot \frac{d\theta_d}{dt} + K_L \theta_d + K_Q \theta_d^2 + K_C \theta_d^3 = T_E(t) + T_{mag}(\alpha, \theta_0) \quad (39)$$

where:

$$K_L = K_{L3} \cdot \theta_0^3 + K_{L2} \cdot \theta_0^2 + K_{L1} \cdot \theta_0 + K_{L0} + T \cos(\alpha) \quad (40)$$

$$K_Q = K_{Q3} \cdot \theta_0^3 + K_{Q2} \cdot \theta_0^2 + K_{Q1} \cdot \theta_0 + K_{Q0} + \frac{1}{24} T \sin(\alpha) \quad (41)$$

$$K_C = K_{C3} \cdot \theta_0^3 + K_{C2} \cdot \theta_0^2 + K_{C1} \cdot \theta_0 + K_{C0} - \frac{1}{6} T \cos(\alpha) \quad (42)$$

and

$$\begin{aligned}
K_{L0} &= 3M_L R + 3K_{Lp} R^2 \\
K_{L1} &= 6K_{Ls} R^2 + 6M_Q R^2 + 6K_{Qp} R^3 + T \sin(\alpha) \\
K_{L2} &= 9 \left(K_{Cs} R^4 - \frac{1}{36} M_L R + K_{Qs} R^3 - \frac{7}{18} K_{Lp} R^2 + M_C R^3 + K_{Cp} R^4 - \frac{1}{108} T \cos(\alpha) \right) \\
K_{L3} &= -\frac{3}{2} M_Q R^2 - 5K_{Qp} R^3 - \frac{3}{2} K_{Ls} R^2 - \frac{1}{6} T \sin(\alpha) \\
K_{Q0} &= 3K_{Qp} R^3 + 3K_{Ls} R^2 + 3M_Q R^2 \\
K_{Q1} &= 9 \left(K_{Qs} R^3 + M_C R^3 + K_{Cs} R^4 + K_{Cp} R^4 - \frac{1}{72} M_L R - \frac{13}{36} K_{Lp} R^2 - \frac{1}{24} T \cos(\alpha) \right) \\
K_{Q2} &= \frac{3}{4} \left(-M_Q R^2 - K_{Ls} R^2 - \frac{19}{2} K_{Qp} R^3 - \frac{1}{216} T \sin(\alpha) \right) \\
K_{Q3} &= -\frac{53}{4} K_{Cp} R^4 - \frac{27}{8} (M_C R^3 - K_{Qs} R^3 - K_{Cs} R^4) + \frac{1}{48} M_L R + \frac{13}{16} K_{Lp} R^2 + \frac{1}{144} T \cos(\alpha) \\
K_{C0} &= 3K_{Cs} R^4 + 3K_{Cp} R^4 - \frac{1}{2} M_L R + 3M_C R^3 - \frac{5}{8} K_{Lp} R^2 + 3K_{Qs} R^3 \\
K_{C1} &= -\frac{5}{4} K_{Ls} R^2 - \frac{9}{2} K_{Qp} R^3 - \frac{5}{4} M_Q R^2 + \frac{1}{6} T \sin(\alpha) \\
K_{C2} &= -3K_{Cs} R^4 - 3M_C R^3 + \frac{35}{48} K_{Lp} R^2 - \frac{101}{8} K_{Cp} R^4 + \frac{1}{24} M_L R - 3K_{Qs} R^3 + \frac{1}{72} T \cos(\alpha) \\
K_{C3} &= \frac{5}{16} K_{Ls} R^2 + \frac{9}{4} K_{Qp} R^3 + \frac{5}{16} M_Q R^2 + \frac{1}{36} T \sin(\alpha)
\end{aligned}$$

With the substitution of the coefficients into equation (39) the dynamic equation of the sensor is in the form of a HelmHoltz-Duffing resonator and solution techniques from the literature can be applied to solve for the vibration behavior of the sensor [42].

3.4 Linear Vibration

When the sensor is excited by a very small excitation force, the amplitude of vibration for the sensor will be very small and the device will experience linear vibration. For sufficiently small rotations of θ_d , the contributions of the nonlinear terms due to θ_d to the dynamic behavior of the system is negligible and the dynamic equation of the system is no longer in the form of a HelmHoltz-Duffing resonator. Excitation of the sensor will result in linear vibration and the equation for sensor dynamics becomes:

$$I \cdot \frac{d^2 \theta_d}{dt^2} + \mu \cdot \frac{d \theta_d}{dt} + K_L \cdot \theta_d = T_E(t) + T_{mag}(\alpha, \theta_0), \quad (43)$$

where the values for I , T_{mag} , and K_L are calculated using the component models presented in the previous sections. The linear natural frequency for the magnetic sensor is:

$$w_0 = \sqrt{\frac{K_L}{I}}$$

where

$$K_L = K_{L3} \cdot \theta_0^3 + K_{L2} \cdot \theta_0^2 + K_{L1} \cdot \theta_0 + K_{L0} + T \cos(\alpha). \quad (44)$$

Even when the system experiences linear vibration, system nonlinearities contribute to the vibration response through the coefficients K_{L3} , K_{L2} , and K_{L1} . T represents the magnitude of the magnetic torque due to T_{mag} .

The linear natural frequency of the sensor is then calculated to be:

$$w_0 = \sqrt{\frac{K_{L3} \cdot \theta_0^3 + K_{L2} \cdot \theta_0^2 + K_{L1} \cdot \theta_0 + K_{L0} + T \cos(\alpha)}{I}}. \quad (45)$$

The dependence of the linear natural frequency of the sensor upon the orientation of the external magnetic field, α , can be seen along with the dependence on θ_0 , which is functions of α and the stiffness of the spring elements within the sensor. It is important to note that the nonlinear restoring torques in the sensor will affect the system response even when it is excited into linear vibration. For the special cases where $\alpha = 0$ and $\alpha = \pi$, the value for θ_0 will be zero and the linear natural frequency for the magnetic sensor will be:

$$w_0|_{\alpha=0} = \sqrt{\frac{K_{L0} + T}{I}} = \sqrt{\frac{3 \cdot M_L R + 3 \cdot K_{Lp} R^2 + T}{I}} \quad (46)$$

$$w_0|_{\alpha=\pi} = \sqrt{\frac{K_{L0} - T}{I}} = \sqrt{\frac{3 \cdot M_L R + 3 \cdot K_{Lp} R^2 - T}{I}} \quad (47)$$

The linear natural frequency will be used in Chapters 4 and 5 to characterize the sensitivity of the magnetic sensor to changes in α .

3.5 Nonlinear Vibration

For large excitation forces, the magnetic sensor will enter the realm of nonlinear vibration and a separate solution method is required to determine the response of the system. The analysis of the nonlinear vibration behavior of the sensor is presented here because it will be used in the proposal of a new frequency detection scheme in chapter 6 to characterize the change in the sensor behavior due to changes in α .

Several techniques have been developed generate the frequency response curves for nonlinear systems [37]. The analytical methods generally involve analyzing the behavior of the system by perturbing the system over small increments, ϵ , of time. The dynamic equation is modified through a variable transformation to generate a set of linear differential equations that can be readily solved by hand. The primary perturbation methods that are presented in literature are the Lindstedt-Poincare and the Method of Multiple Scales [37].

Another technique that has been applied to solve for the response of nonlinear systems to parametric excitation is the harmonic balance method. In this technique the form of the solution is assumed to be a trigonometric series with multiple harmonics. The assumed solution is substituted into the initial differential equation and terms with a common harmonic are collected. The harmonic balance method lends itself to the application of numerical computation and research has been conducted to increase the efficiency of finding the series coefficients through the use of computational methods. A method that has been used to speed up the solution finding process is to apply the Newton-Raphson Method to the algebraic equations, HBNR [16]. By switching the order at which the Newton-Raphson and Harmonic Balance methods are applied to the differential equation, the Incremental Harmonic Balance method has been developed [12].

3.5.1 Incremental Harmonic Balance Method

The method chosen to simulate the frequency response of magnetic sensor is the Incremental Harmonic Balance Method, IHB, presented in [12]. This technique was chosen due to the speed at finding the solution and the generality of the solution procedure to all forms of nonlinear dynamic equations. The method presented in [12] has been modified to include the quadratic nonlinearity that is seen in dynamic model of the sensor. The solution procedure involves the application of the Newton-Raphson procedure to the dynamic equation of the sensor followed by the application of the Galerkin averaging method to find the solution of the differential equation. The accuracy of the solution can be increased by the increasing the number of harmonics that are present in the assumed solution for the response.

The first step in the IHB method is to perform a change of variables to transform the equation from the time domain to a dimensionless domain with the substitution:

$$\tau = \omega \cdot t. \quad (48)$$

Equation (39) now takes the dimensionless time form of:

$$\omega^2 \cdot I \cdot \frac{d\theta_d^2}{d\tau^2} + \omega \cdot \mu \cdot \frac{d\theta_d}{d\tau} + (K_L + \bar{K}_Q + \bar{K}_C) \cdot \theta_d = T \cdot \cos(\tau). \quad (49)$$

The values of \bar{K}_Q and \bar{K}_C are:

$$\bar{K}_Q = K_Q \cdot \theta_d \quad (50)$$

$$\bar{K}_C = K_C \cdot \theta_d^2 \quad (51)$$

A substitution is then made for θ such that:

$$\theta_d = \theta_{d0} + \Delta\theta_d \quad (52)$$

$$\omega = \omega_n b + \Delta\omega \quad (53)$$

where θ_{d0} is related to the response of a nearby state of excitation at $\omega_n b$ and $\Delta\theta_d$ is the difference in the response between the two states when the excitation frequency is changed by $\Delta\omega$.

By substituting (52) and (53) into equation (49) the following incremental equation is derived.

$$\omega_0 I \frac{\partial^2 \Delta \theta_d}{\partial \tau^2} + \omega_0 \mu \frac{\partial \Delta \theta_d}{\partial \tau} + (K_L + 2\bar{K}_Q + 3\bar{K}_C) \Delta \theta_d = R - \left(\omega_0 I \frac{\partial^2 \theta_d}{\partial \tau^2} + \mu \frac{\partial \theta_d}{\partial \tau} \right) \Delta \omega \quad (54)$$

$$R = T \cos(\tau) - \left(\omega_0^2 \cdot I \frac{\partial^2 \theta_{d0}}{\partial \tau^2} + \omega_0 \cdot \mu \frac{\partial \theta_{d0}}{\partial \tau} + (K_L + \bar{K}_Q + \bar{K}_C) \cdot \theta_{d0} \right) \quad (55)$$

Higher order terms of $\Delta \theta$ and $\Delta \omega$ have been ignored since they are very small.

The steady state response of the magnetic sensor is assumed to be a Fourier series expansion of Nth order harmonic terms:

$$\theta_{d0} = \sum_{k=0}^N a_k \cos(k \cdot \tau) + \sum_{j=1}^N b_j \sin(j \cdot \tau) \quad (56)$$

$$\Delta \theta_d = \sum_{k=0}^N \Delta a_k \cos(k \cdot \tau) + \sum_{j=1}^N \Delta b_j \sin(j \cdot \tau) \quad (57)$$

The solution for system response is represented in vector form such that:

$$\mathbf{C} = \begin{bmatrix} 1 & \cos(\tau) & \cos(2\tau) & \dots & \cos(N\tau) & \sin(\tau) & \dots & \sin(N\tau) \end{bmatrix} \quad (58)$$

$$\mathbf{A} = \begin{bmatrix} a_0 & a_1 & a_2 & \dots & a_N & b_1 & b_2 & \dots & b_N \end{bmatrix} \quad (59)$$

$$\Delta \mathbf{A} = \begin{bmatrix} \Delta a_0 & \Delta a_1 & \Delta a_2 & \dots & \Delta a_N & \Delta b_1 & \Delta b_2 & \dots & \Delta b_N \end{bmatrix} \quad (60)$$

$$(61)$$

where

$$\theta_{d0} = \mathbf{C} \cdot \mathbf{A}$$

$$\Delta \theta_d = \mathbf{C} \cdot \Delta \mathbf{A}$$

The Galerkin procedure is then applied to (54) to develop the final equations that will be used to determine the response of the sensor to different excitation frequencies. The Galerkin method assumes that the system response can be accurately represented by an approximate solution composed of trial functions. The trial functions satisfy the boundary conditions of the problem and are then substituted into the original differential equation. The terms in \mathbf{C} are used as the both the trial and weighting

functions in the implementation of the Galerkin procedure. The resulting differential equation is then integrated over a period of as $0 < \tau < 2\pi$. The solution of integral is a non-zero value that represents the residual error of the approximation. The scalar coefficients of the trail functions are then adjusted iterively so that the residual error in the approximation approaches zero. The adjustments can be made by using the method of weighted residuals as described in [17].

With the implementation of the Galerkin procedure, the differential equation of the system becomes:

$$\int_0^{2\pi} \mathbf{C}^T \left\{ w_0^2 \cdot I \frac{\partial^2 \Delta q}{\partial \tau^2} + \omega_0 \cdot \mu \frac{\partial \Delta q}{\partial \tau} + \left(K_L + 2 \cdot \bar{\bar{K}}_Q + 3 \cdot \bar{\bar{K}}_C \right) \Delta q \right\} d\tau \quad (62)$$

$$= \int_0^{2\pi} \mathbf{C}^T \left\{ R - \left(2w_0 \cdot M \frac{\partial^2 q_0}{\partial \tau^2} + \mu \frac{\partial q_0}{\partial \tau} \right) \Delta \omega \right\} d\tau, \quad (63)$$

which can be simplified to:

$$\mathbf{K}_{mc} \Delta \mathbf{A} = \mathbf{R} - \mathbf{R}_{mc} \Delta \omega. \quad (64)$$

The values for the variables within (64) are:

$$\mathbf{K}_{mc} = \omega_0^2 \mathbf{M} + \omega_0 \mu + \mathbf{K} + 2 \cdot \mathbf{K}_2 + 3 \cdot \mathbf{K}_3 \quad (65)$$

$$\mathbf{R} = \mathbf{F} - \left(\omega_0^2 \mathbf{M} + \omega_0 \Upsilon + \mathbf{K}_L + \mathbf{K}_Q + \mathbf{K}_C \right) \mathbf{A} \quad (66)$$

$$\mathbf{R}_{mc} = (2 \cdot \omega_0 \mathbf{M} + \Upsilon) \mathbf{A} \quad (67)$$

$$\mathbf{M} = \int_0^{2\pi} \mathbf{C}^T M \ddot{\mathbf{C}} d\tau \quad (68)$$

$$\Upsilon = \int_0^{2\pi} \mathbf{C}^T \mu \dot{\mathbf{C}} d\tau \quad (69)$$

$$\mathbf{K}_L = \int_0^{2\pi} \mathbf{C}^T K_L \mathbf{C} d\tau \quad (70)$$

$$\mathbf{K}_Q = \int_0^{2\pi} \mathbf{C}^T \bar{\bar{K}}_Q \mathbf{C} d\tau \quad (71)$$

$$\mathbf{K}_C = \int_0^{2\pi} \mathbf{C}^T \bar{\bar{K}}_C \mathbf{C} d\tau \quad (72)$$

$$\mathbf{T} = \int_0^{2\pi} \mathbf{C}^T T \cdot \cos(\tau) d\tau \quad (73)$$

To begin the solution process an initial guess of the coefficients in \mathbf{A} is entered into (64) and the solution for $\Delta\mathbf{A}$ is found. Since (64) is a system of linear equations and \mathbf{K}_{mc} is full rank, the values for $\Delta\mathbf{A}$ can be found by multiplying both sides of the equation by \mathbf{K}_{mc}^{-1} . The solution for $\Delta\mathbf{A}$ are added \mathbf{A} such that:

$$\mathbf{A}_{k+1} = \mathbf{A}_k + \Delta\mathbf{A}, \quad (74)$$

and another iteration is run. The process is stopped when the value for \mathbf{R} is sufficiently small. To generate the frequency response of the first system the value of ω is increased and the previous solution for \mathbf{A} is used as the initial condition for the next set of iterations.

3.5.2 Mechanics Modeling Example

The device in Appendix (B.1) represents a fabricated the magnetic sensor without the presence of a permanent magnet. The beams within the device have a length, width, and height of $2000 \mu m$, $14 \mu m$, and $200 \mu m$ respectively. Analysis of this structure will provide validation for the mechanics modeling of the inertia and beam elements within the sensor. The equation of motion for the system was developed by entering the dimensions and parameters of the device into the equations derived in Section 3.2.

By inputting the system parameters into equation (22), the inertia of the device was calculated to be $3.0863 * 10^{-12} Kg \cdot m^2$. The stiffness coefficients for the system were derived using the procedure in Section 3.2.1 and were found to be:

$$T_P = \left[17.8640 \cdot R \sin(\theta) + 6.0265 * 10^4 \cdot R^2 \sin^2(\theta) + 1.2141 * 10^{11} \cdot R^3 \sin^3(\theta) \right] R \cos(\theta)$$

$$T_S = \left[24.8088 \cdot R \sin(\theta) + 1.878 * 10^8 \cdot R^2 \sin^2(\theta) \right] R \sin(\theta)$$

$$M_0 = .0215 \cdot R \sin(\theta) + 65.8906 \cdot R^2 \sin^2(\theta) + 5.8605 * 10^7 R^3 \sin^3(\theta)$$

From the model of comb drive behavior in equation (29), the excitation element within the device is modeled to be:

$$T_E(t) = Amp \cdot \cos(2 \cdot \omega \cdot t). \quad (75)$$

The value for Amp of the excitation torque was found by curve-fitting an IHB solution of a Duffing oscillator to the experimental data. A Duffing oscillator contains cubic nonlinearities and no quadratic nonlinearities. A HelmHoltz-Duffing curve fit was not applied due to the coupling of the effects from the quadratic and cubic nonlinearities on the response of the system to parametric excitation. The cubic nonlinearities provide a spring stiffening effect on the system during excitation and cause the response curve to lean to the right, while the quadratic nonlinearities provide a spring softening effect that causes the curve to lean to the left. Since the quadratic and cubic nonlinearities cause the opposite effects on system response, many different combinations of cubic and quadratic coefficients will lead to the same system response. Since the goal of the comparison was not to determine the cubic and quadratic coefficients, but instead the amplitude of the excitation torque and the damping coefficients the application of a Duffing oscillator curve fit can be used to determine those values without address the issue of the multiple solutions for the quadratic and cubic coefficients.

The damping coefficient μ was found by fitting an IHB solution to the experimental data and varying the value of μ until the jump-down from the upper branch occurred at the same frequency as seen in the experiment. The value for μ was determined to be 30.90. The fit of Duffing solution also provided a means determining the linear natural frequency of the device from experiment, since the variations in ω_0 will shift the location of frequency response curve to the left or right. The linear natural frequency was found to be $5500 \frac{rad}{sec}$ by adjusting the value of ω_0 until the curve fit and the experimental results were aligned. Finally, the value for the excitation torque was found by varying the value for T_E until the experimental results for the lower

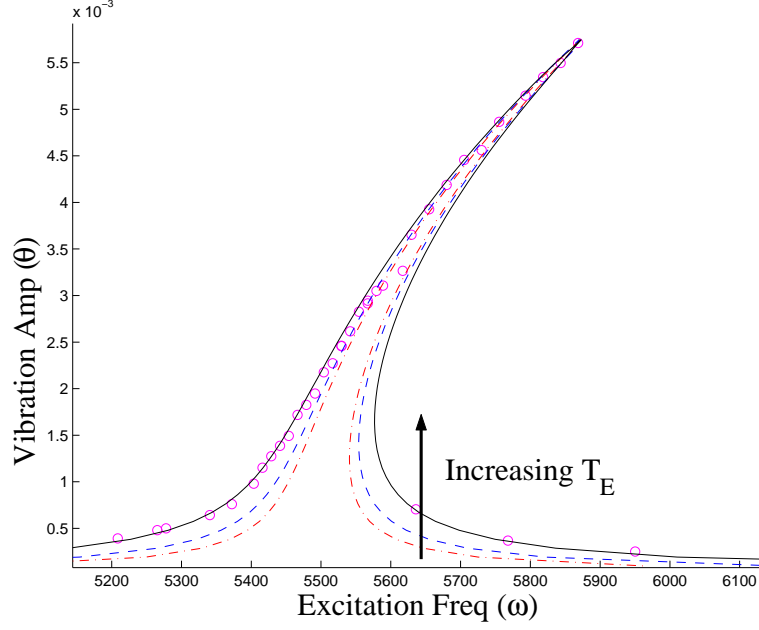


Figure 10: Example for Implementation of T_E Curve Fitting.

steady-state amplitudes coincided as shown in Figure 10. The value for the excitation torque was found to be $2000 \text{ N} \cdot \text{m}$.

By entering the coefficients into the dynamic equation of the sensor (36), the following equation was derived to describe the dynamic behavior of the system:

$$3.0863 * 10^{-12} \ddot{\theta} + 30.90 \dot{\theta} + 1.18 * 10^{-4} \theta + 4.53 * 10^{-4} \theta^2 + 4.74 \theta^3 = 2000 \cdot \cos(2 \cdot \omega \cdot t) \quad (76)$$

Figure (11) shows a comparison of the nonlinear vibration response of a device from experiments to the results predicted by the analytical model. From Figure 11 it can be seen that the analytical model of the sensor without the magnet provides a reasonably accurate prediction of the contribution of the nonlinear terms to the vibration behavior of the sensor. The difference between two curves that is seen as a shift of the entire frequency response curve is related to variations in the linear natural frequency predicted by the model from the experimental results. The value for the linear natural frequency found through a fit of an IHB solution to the experimental results is $\omega_0 = 5500 \frac{\text{rad}}{\text{sec}}$, while the theoretical value for ω_0 is $5150 \frac{\text{rad}}{\text{sec}}$. The error

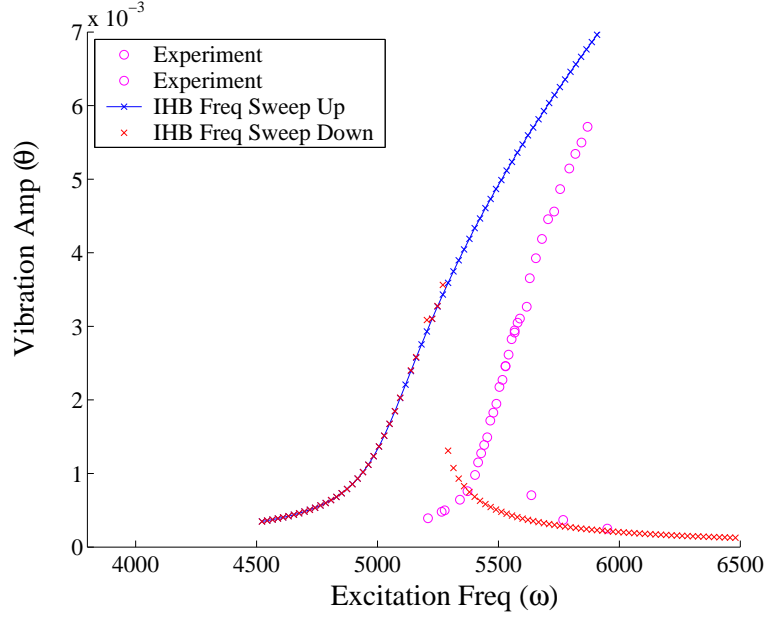


Figure 11: Comparison of Analytical Model to Experimental Data.

between the theoretical and experimental linear natural frequency is 6.36%. The difference is most likely related to an over prediction of the inertia properties of the device in the analytical model that do not account for all possible variations in dimensions of the device due to manufacturing.

The variation in the nonlinear behavior of resonator predicted by the model when compared to experimental results is minimal, which provides validation for modeling of the nonlinear system components presented in previous sections. The overall model of the device compares well with the experimental results and validates that the mechanical model can be used to predict the response of the system to excitation. The mechanical model will be extended to include the effect of the magnet in the sensor based upon the model for magnetic field interactions from the literature and presented in Section 3.2.3.

3.5.3 Magnetic Sensor Example

A device similar in dimension to the one previously modeled was simulated with the addition of a magnet. The properties of the magnetic field interaction were modeled

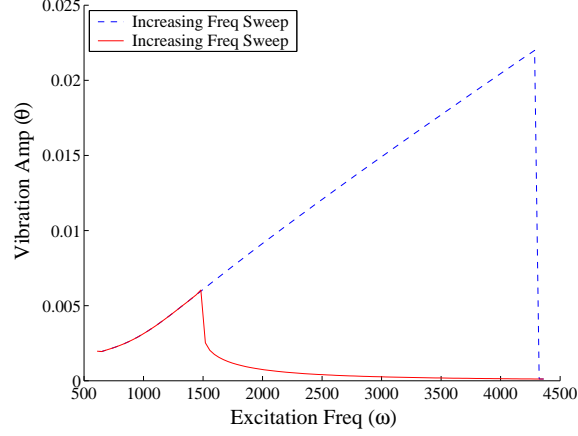


Figure 12: Simulated Response of Magnetic Sensor.

based upon those presented in [28]. The magnet is composed of neodymium-iron-boron and is assumed to be glued to the central disk in the device and cylindrical in shape. The thickness of the magnet is $800 \mu m$, radius of $800 \mu m$, and a density of $7440 \frac{g}{cc}$. The magnetic torque due to the interaction between the earth's magnetic field and that of the magnet is modeled as $T = 7.2 * 10^{-8} N \cdot m$ [28]. The inertia that is added to the resonator because of the magnet is $2.5530 * 10^{-12} N \cdot m$. This value is added to the overall inertia of the system which becomes $5.7955 * 10^{-12} N \cdot m$. The excitation amplitude for T_E in the simulation is $2000 N \cdot m$.

Figure 12 shows the response of the modeled magnetic sensor to excitation when the magnetic field of the magnet is aligned with that of the earth's. This orientation corresponds to the value of α equal to zero for the coefficients used in equation (39). The nonlinear vibration behavior of the system can be clearly seen in the figure due to the angle of the resonant peak and the dependence of the response on the direction of the frequency sweep.

By analyzing the changes in the system variables of equation (39) with changes in the external magnetic field properties, it is possible to better understand the relationship various parameters of the magnetic sensor lead to changes in the resonant behavior of the sensor. Figure 13(a) shows a plot of the change in K_C coefficient of equation (39)

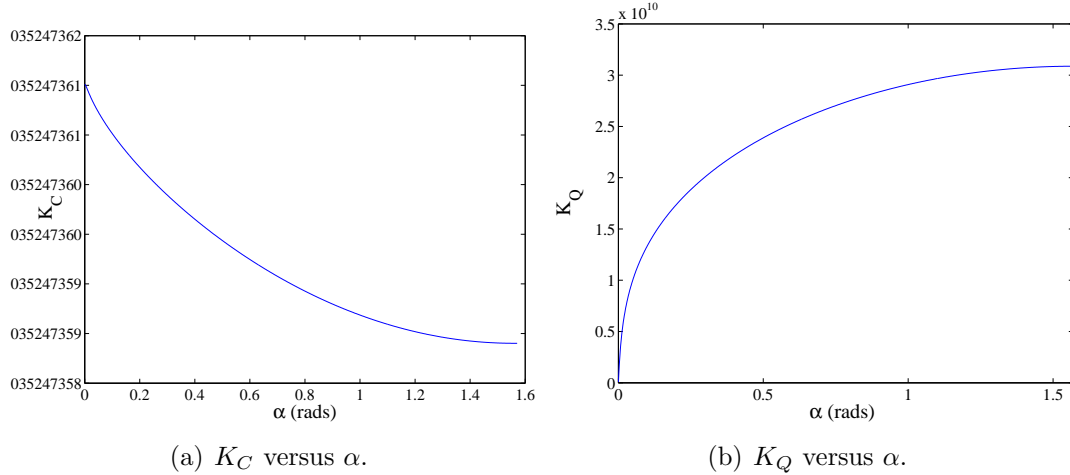


Figure 13: Comparison of System Coefficients versus α .

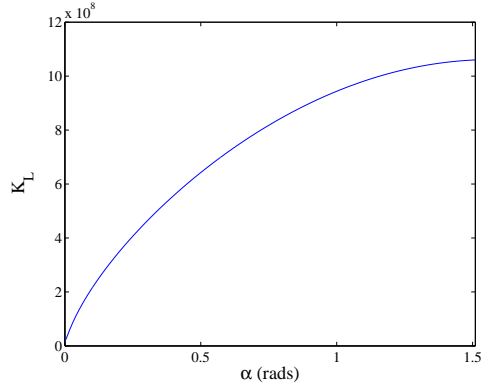


Figure 14: K_L versus α .

for the device. The value for K_C decreases with increases in α , but more importantly the figure shows that the coefficient does not significantly change with changes in α . Figure 13(b) shows the behavior of K_Q with changes in α and the same insensitivity to α is seen. Therefore the coefficients K_Q and K_C will not be used in the detection scheme for the sensor.

Figure 14 shows the change in K_L versus changes in α and it can be seen that the variable is far more sensitive to alteration of the properties of the external magnetic field. The modifications to K_L and therefore to ω_0 will be discussed in the following chapter along with the optimization of sensor beam dimensions.

3.6 Conclusion

Analytical models for the system components within the magnetic sensor have been developed. By combining the analysis of the static rotation of the central disk from magnetic torque and the dynamic behavior of the sensor, a model has been developed that can be used to predict the change in the resonant behavior of the device due to changes in the orientation of an external magnetic field. The model of system mechanics has been shown to compare well with experimental values as shown in Figure 11. It is expected that the overall performance sensitivity of the sensor can be improved as the dimensions of the beams are optimized. The modification of the parameters in the dynamic equation of the sensor will be discussed in later sections of this thesis.

CHAPTER IV

DESIGN OF PASSIVE SENSOR COMPONENTS

To further improve the sensitivity of the sensor, the system parameters that directly affect the linear natural frequency of the sensor shall be determined and optimized in order to maximize the change in the linear natural frequency resulting from changes in α . A study of magnetic sensor parameters will consider how variations in the length, width, and height of the sensor beams will affect the sensitivity that can be achieved by the device. Figure 15 shows a diagram of the beam model and the labels for each of the beam dimensions used. The study will show that increasing the nonlinear behavior of the sensor will increase its performance and can be achieved by the design of the beam dimensions. The optimization of sensor geometry has been termed the passive design since the sensitivity of the device will be improved through the design of beams, which are non-powered sensor components. The methodology used to optimize the dimensions of the beams in the magnetic sensor will also be presented in this chapter along with simulation results to show the optimized design will result in an increased sensitivity of what was previously achieved in [28].

4.1 Parameter Sensitivity Study

From Chapter 3 the equation for the linear natural frequency of the sensor is:

$$\omega_0 = \sqrt{\frac{K_{L0} + K_{L1} \cdot \theta_0 + K_{L2} \cdot \theta_0^2 + K_{L3} \cdot \theta_0^3 + T \cos(\alpha)}{I}}.$$

where K_{L0} , K_{L1} , K_{L2} , and K_{L3} are components of the stiffness of the device and θ_0 is the static equilibrium rotation of the sensor due to the magnetic torque in the sensor.

The sensitivity of the linear natural frequency, ω_0 , and therefore the magnetic

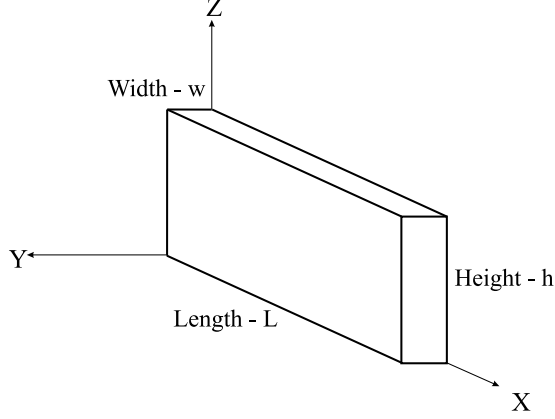


Figure 15: Diagram of Beam Dimensions.

sensor to changes in α is:

$$\left| \frac{\partial \omega_0}{\partial \alpha} \right| = \frac{T \sin(\alpha)}{2\sqrt{I} \sqrt{T \cos(\alpha) + K_{L0} + K_{L1}\theta_0 + K_{L2}\theta_0^2 + K_{L3}\theta_0^3}} \quad (77)$$

Since the linear natural frequency is currently being used as a means of detecting the orientation of the external magnetic field, the sensitivity of the device can be evaluated using equation (77) since it shows how changes in the value of α will result in changes in the linear natural frequency of the device. From (77) it can be seen that the sensitivity of the magnetic sensor can be increased by modifying the physical properties of the magnet within the system. Increasing the magnetic torque of the sensor will result in a scalar increase in the sensitivity of the sensor. The increase in the torque can be achieved by increasing the size of the magnet or through use of a material with increased the magnetic field strength as the permanent magnet in the device.

A second way to increase the sensitivity of the sensor is by modifying the dimensions of the beams in the system to change the coefficients K_{L0} , K_{L1} , K_{L2} , and K_{L3} . By inspection of (77) it is difficult to determine if increasing or decreasing the coefficients will result in a decrease in the denominator of the equation due to the coupling of θ_0 and the beam dimensions with the stiffness coefficients. The change in

sensitivity of the sensor due to variations in the beam parameters should be analyzed through numerical simulation. It was shown in the [28] that the sensitivity decreases in the regions near $\alpha = \pm \frac{\pi}{2}$. Therefore the sensitivity of the sensor to changes in α will be evaluated at $\alpha = \frac{\pi}{2}$ since this location limits the sensitivity that can be realized over the entire operating range by the magnetic sensor. The magnetic torque used during the simulations is $T = 7.6 * 10^{-10}$ [28].

Figure 16 shows how the sensitivity of the natural frequency varies for various combinations of beam heights and widths for a beam with length $2000 \mu m$. From the figure it can be seen that the height and width of the beams should be made as small as possible to improve the sensitivity of the magnetic sensor to changes in the external magnetic field orientation. The reduction in the cross-section of the beam will greatly reduce the linear stiffness of the beam and will result in increases in the static equilibrium angles for a given value of α . This can be seen in Figure 17, which shows the value of θ_0 for corresponding beam widths and heights as those in Figure 16. Increases in the value for θ_0 will cause beams to enter the region of large deflection operation such that the deflection of the beams is approximately the same as the beam width. Beams in this region exhibit highly nonlinear behavior and the nonlinear stiffness plays a significant role in the resistance of the beam to bending. Since sensitivity of the magnetic sensor is primarily based upon the nonlinear behavior of the beams, improvements in sensitivity can be realized through reductions in the width and height of the beams. Increasing the large deflection behavior will result in an increase in the sensitivity of the sensor since changes in α will result in greater changes in the linear natural frequency of the device.

The effect of varying the length of the beams on the sensitivity of the sensor is shown in Figures 18 and 19 along variations in the height and width of the beams. From the two figures it can be seen that an alternative way to increase the sensitivity of the magnetic sensor is increase the lengths of the beams within the sensor. The

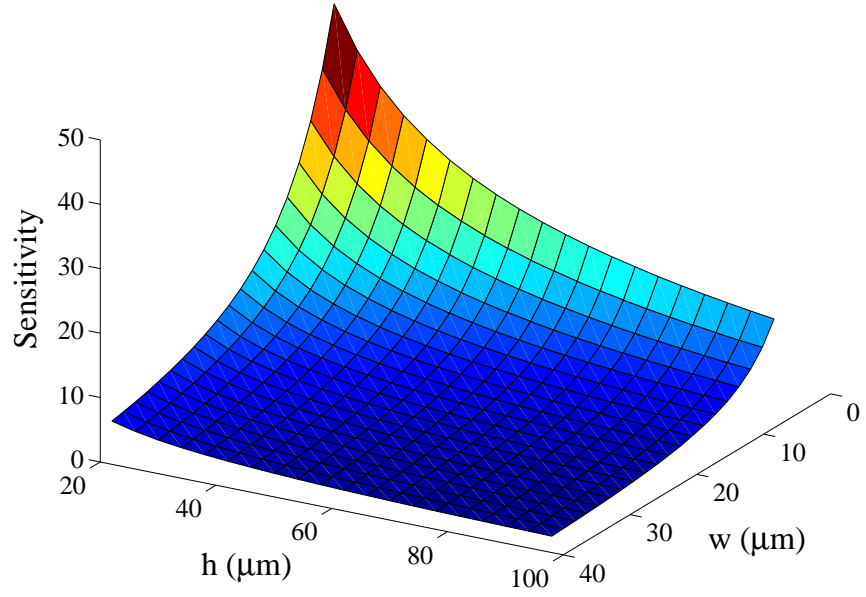


Figure 16: Comparison of System Behavior with Variations in Width and Height: Sensitivity Curve.

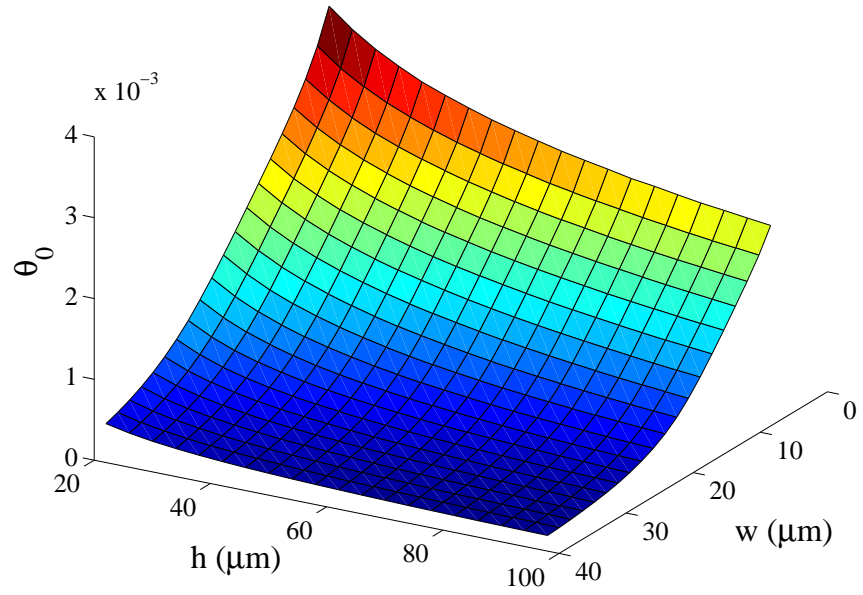


Figure 17: Comparison of System Behavior with Variations in Width and Height: Deflection (θ_0).

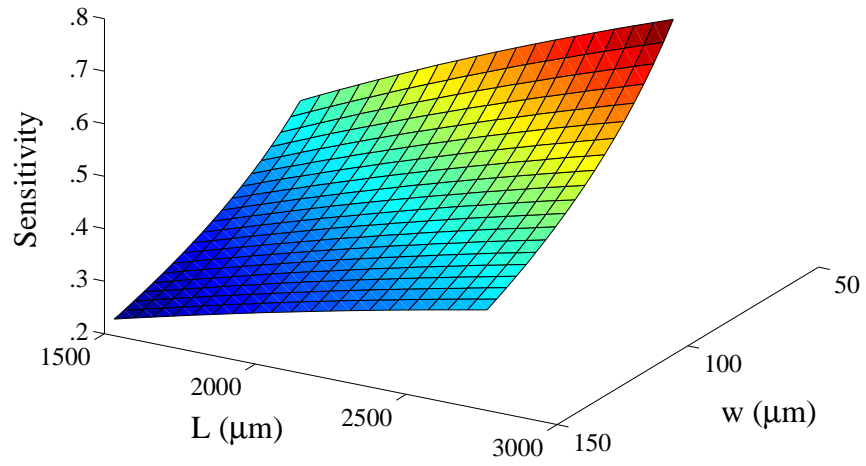


Figure 18: Comparison of System Behavior with Variations in Width and Length: Sensitivity Curve.

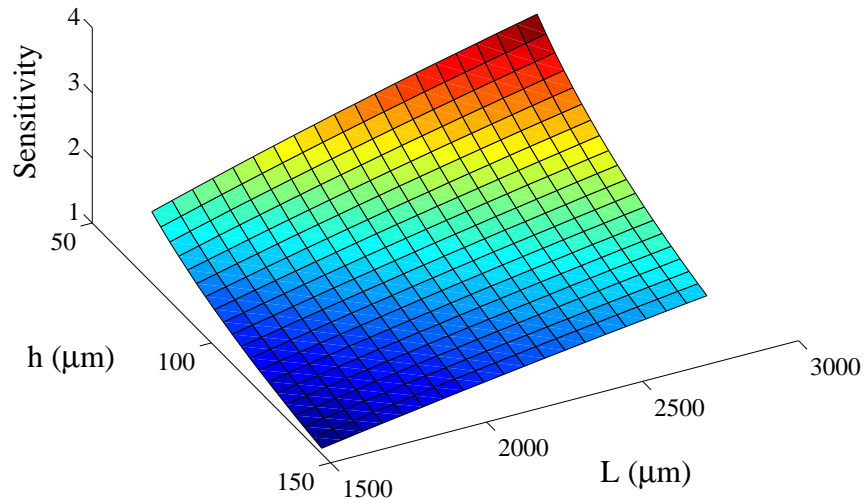


Figure 19: Comparison of System Behavior with Variations in Height and Length: Sensitivity Curve.

increases in the beam length will further reduce the stiffness of the beam and allow it to deflect such that the nonlinear stiffness of the beam will have a greater effect on the restoring torque provided. The increase in the nonlinear behavior will result in an increase in the sensitivity of the sensor similar to the reduction in the beam cross-section.

4.2 Beam Geometry Optimization

An optimization routine was developed in MATLAB to find the optimal values of beam height, width, and length that will maximize the sensitivity of the sensor. Based upon the sensitivity analysis performed in Section 5.3.1, it was expected that the optimal dimensions for the beams within the sensor would have a length as large as can be achieved with the system constraints and a width of as small as allowable. Therefore, the height of the device was expected to be the variable that would be adjusted to satisfy the system constraints. An exhaustive search of the height variable was implemented to search the design space of the variable.

The exhaustive search technique is appropriate for use when the objective function is not convex and there are many local minimums or maximums present within the search space. The presence of local minimums or maximums severely limits the effectiveness of many optimization techniques since multiple iterations of the algorithms are often required with multiple starting points to ensure that the algorithm will find the global optimization. Another benefit of an exhaustive search technique is its ability to find the global solution in a single iteration of the algorithm.

4.2.1 Objective Function

While the main principle of the magnet sensor is to use changes in resonant frequency to sense changes in α , the amount of change that is detectable can be limited by the technique that is used to record the linear natural frequency of the sensor. To have

a systematic approach for evaluating the sensitivity of the sensor that is independent of the frequency detection method for the sensor, the sensitivity is defined by:

$$\text{Sens} = \frac{f(\alpha_2) - f(\alpha_1)}{\alpha_2 - \alpha_1}. \quad (78)$$

The values used to evaluate the sensitivity of the sensor are $\alpha_2 = \frac{\pi}{2}$ and $\alpha_1 = \frac{\pi}{2} - 0.1$. The sensitivity for the sensor is used as the objective function of the algorithm and represents a numerical evaluation of equation (77).

Optimization routines are typically implemented to find the minimum of an objective function and it is common to convert maximization problems into minimization by multiplying the objective function by -1 . Since the goal of the algorithm is to maximize the sensitivity of the sensor, the approach was used to be consistent with the common practices in the optimization field. Therefore, the objective function of the exhaustive search is:

$$\text{Obj} = -\text{Sens}. \quad (79)$$

If the simulation of the magnetic sensor violated any of the optimization constraints, the value for the objective function is:

$$\text{Obj} = 0. \quad (80)$$

4.2.2 Constraints

The first constraint implemented in the optimization algorithm is the structural stress of the beams at their anchor supports. Since the lateral deflection of the beam is much less than the length of the beam, superposition has been used to analyze the effects of shear, tensile stress and bending stress independently. From mechanics of materials, the shear stress on the face of the beam is calculated as:

$$\tau_{yz} = \frac{\sqrt{P^2 + W^2}}{A_c} \quad (81)$$

where P is the lateral force on the face of the beam-anchor interface, W is the weight of the magnet and central disk region that must be supported by a single beam, and

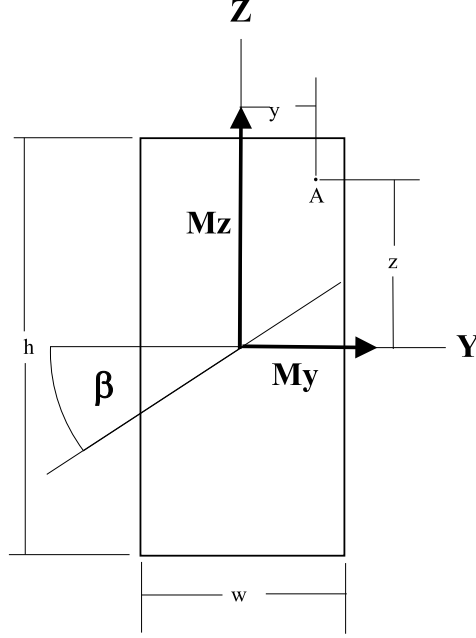


Figure 20: Beam Cross-Section with Bending Moments.

A_c is the cross-sectional area of the beam. The values τ_{zx} and τ_{xy} are zero since forces P and W are applied to the beam-anchor interface only. The axial stress at the beam-anchor interface is calculated based upon the axial stress that develops in the beam due to deflection and rotation such that:

$$\sigma_{axial} = \frac{S}{A_c}. \quad (82)$$

where S is the axial force at the beam-anchor interface.

The bending stress at the interface is the resultant of the effects of the moment on the face caused by disk rotation and the moment resulting from supporting the magnet and central disk area as shown in Figure 20 as M_z and M_y respectively. The bending stress at a position A in the figure is [20]:

$$\sigma_{bend} = \frac{M_y z}{I_z} - \frac{M_z y}{I_y}, \quad (83)$$

where y and z are the distance of the point from the origin and

$$I_y = \frac{1}{12} \cdot w \cdot h^3 \quad (84)$$

$$I_z = \frac{1}{12} \cdot h \cdot w^3 \quad (85)$$

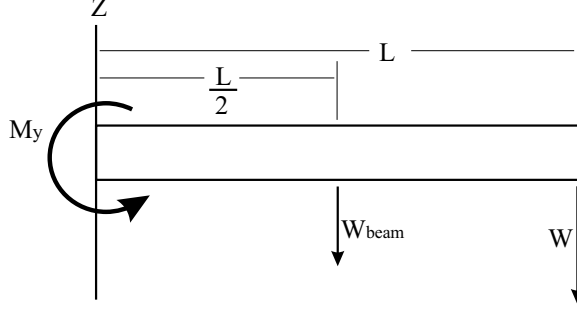


Figure 21: Free-Body Diagram of a Beam in Z-Axis Bending.

The value for M_z is equal to the value for M_A as discussed in Section 3.2.1.2 such that:

$$M_z = M_{AL} \cdot (\theta_0 \cdot R) + M_{AQ} \cdot (\theta_0 \cdot R)^2 + M_{AC} \cdot (\theta_0 \cdot R)^3, \quad (86)$$

where M_{AL} , M_{AQ} , and M_{AC} are the coefficients for the moment at the beam anchor supports as a function of beam deflection. M_y is found by determining the portion of mass from the magnet and center section that must be supported by a single beam.

Linear beam theory is used to determine the value for M_y since the deflection of the beam in the z direction will not approach the large deflection region due to its increased stiffness. The weight of the magnet is modeled as equally distributed among the three beams within the sensor. The equation for M_y is developed based upon the free-body diagram shown in Figure 21:

$$M_y = \frac{WL}{3} + \frac{W_{beam}L}{2} \quad (87)$$

The maximum bending stress in the cross-section is found by locating the point on the perimeter of the cross-section that is furthest from the neutral axis, which represents locations in the beam cross-section where the bending stress is zero. The location of the neutral axis can be found setting (83) equal to zero:

$$0 = \frac{M_z y}{I_y} - \frac{M_y z}{I_z}. \quad (88)$$

Thus, the rotation of the neutral axis from the y-z axis is found by:

$$\tan(\beta) = \frac{y}{z} = \frac{M_y I_z}{M_z I_y} \quad (89)$$

A line search has been implemented in MATLAB to find y_{max} and z_{max} that represents the point furthest from the neutral axis. A bracket search technique is used for the line search due to its simplicity and efficiency.

The bending stress at the point furthest from the neutral axis is:

$$\sigma_{bendmax} = \frac{M_z y_{max}}{I_y} - \frac{M_y z_{max}}{I_z}, \quad (90)$$

which represents the maximum bending stress on the face and is the value used in the evaluation of the stress constraint for a given beam combination. The location of the maximum normal stress on the beam face will occur at the location of the maximum bending stress and is calculated to be:

$$\sigma_x = \sigma_{axial} + \sigma_{bendmax}. \quad (91)$$

The values for the σ_y and σ_z are zero at the interface since the bending moments and axial force only act on the beam-anchor interface.

The maximum stress at the beam-anchor interface is found by calculating the Von Mises stress at the location of the maximum bending stress. The equation for the Von Mises stress is [39]:

$$\sigma_{VonM} = \sqrt{\frac{(\sigma_x - \sigma_y)^2 + (\sigma_y - \sigma_z)^2 + (\sigma_z - \sigma_x)^2 + 6(\tau_{xy}^2 + \tau_{yz}^2 + \tau_{zx}^2)}{2}} \quad (92)$$

which when applied to the beam-anchor interface is simplified to be:

$$\sigma_{VonM} = \sqrt{\frac{2 \cdot (\sigma_x)^2 + 6 \cdot \tau_{yz}^2}{2}} \quad (93)$$

The magnetic sensor will be constructed of polysilicon and due to the small expected dimension of the beam width, less than $10 \mu m$, the properties of thin-films of polysilicon are used to determine the allowable stress at the beam-disk interface. The yield stress of thin-films of polysilicon that are a few microns in height is 698 MPa [22]. A factor of safety of 2 was chosen to allow for unpredictable variations in beam

behavior. Therefore the maximum allowable stress at the beam-anchor interface is:

$$\sigma_{allow} = \frac{\sigma_{yield}}{2} = 349 \text{ MPa} \quad (94)$$

and will be evaluated at the maximum value of θ_0 which occurs at $\alpha = \frac{\pi}{2}$.

The implementation of the stress constraint in the optimization code is:

$$Constraint_1 = \sigma_{VonM} - \sigma_{allow} \quad (95)$$

and is satisfied when $Constraint_1$ is less than zero.

The second constraint placed on the device was chosen to ensure that the frequency of the vibration mode corresponding to motion of the central region of the sensor along the z-axis is no less than 2.5 times greater than the linear natural frequency for the torsional mode of vibration corresponding to $\alpha = \frac{\pi}{2}$. The constraint prevents the excitation of the torsional vibration mode of the device from inducing out of plane vibration in the z-direction that would affect the quality of the sensor oscillation. By placing the constraint at a fraction instead of a whole number, the chance of the torsional vibration mode exciting higher order harmonics of the z-axis vibration is also reduced since the harmonics are integer multiples of the fundamental resonant frequency.

Due to the requirement for a z-direction natural frequency that is significantly higher than the torsional mode, it is expected that the deflection of the beams in the z-direction will be much less than the height and linear beam deflection theory is used to analyze the device behavior. The model of the z-direction motion of the sensor has been simplified to a basic mass-spring resonator as shown in Figure 22. The dynamic equation for the motion in the z of a three beam sensor is:

$$M \ddot{z} + \mu_z \dot{z} + 3K_z z = F, \quad (96)$$

where M is the mass of the central disk and magnet, z is the motion of the center of

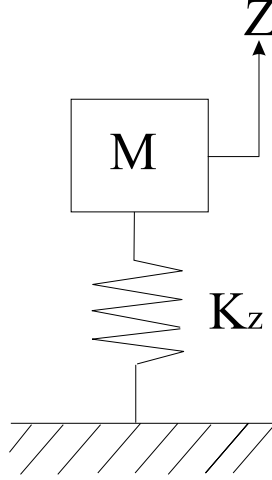


Figure 22: Diagram of Z-direction Sensor Motion.

Table 1: Magnetic Sensor Constraints

Constraints
$\omega_z > 2.5 \cdot \omega_0$
$\sigma_{max} < \frac{\sigma_y}{2} < 349\text{MPa}$
$L = 2000 \mu\text{m}$
$w = 5 \mu\text{m}$

mass, and F is the excitation force. The spring stiffness for each beam is [18]:

$$K_z = \frac{12 \cdot E \cdot I_y}{L^3}, \quad (97)$$

where the value of I_y is the moment of inertia of the beam cross-section as presented in equation (84). The linear natural frequency for vibration in the z-direction is:

$$\omega_z = \sqrt{\frac{3 \cdot K_z}{M_{center}}} \quad (98)$$

The implementation of the frequency constraint within the optimization algorithm is:

$$Constraint_2 = 2.5 - \frac{\omega_z}{\omega_0}, \quad (99)$$

where ω_0 is the linear natural frequency of the torsional vibration mode.

More constraints are placed on the dimensions of the beams within the system through the implementation of upper and lower boundaries on the beam dimensions.

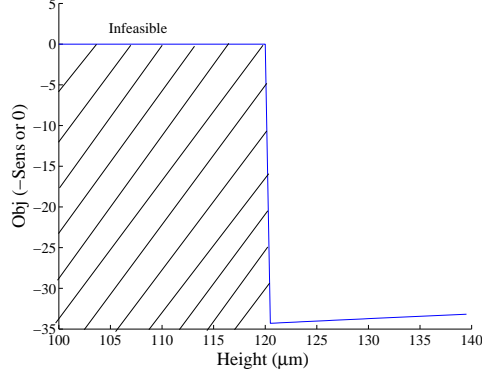


Figure 23: Objective Function Results for Sensor Optimization of Beam Height.

The constraint that was placed upon the width of the beams is based upon the fabrication procedures that are used to create the device in the Microelectronics Research Center of Georgia Tech. Based upon the facilities used to construct the device, a minimum dimension of $5 \mu m$ has been used to limit the minimum width and height of the beams within the sensor.

A secondary goal of the sensor is to reduce the size of the device, despite increasing the sensitivity. The upper limit for the maximum beam length, L , was chosen to be $2000 \mu m$ since the length of the beams within the device are dimension that directly relate to the overall size of the device. The choice in the upper limit was arbitrary and future work may show that a different type of length constraint may be more suitable for use in the magnetic sensor. A full list of all of the constraints placed in the optimization algorithm of the magnetic sensor is shown in Table 4.2.2.

4.3 Results and Conclusion

The exhaustive search algorithm of the design space was executed to determine the beam height would result in the greatest increase of the sensitivity while also satisfying the constraints placed on the system. The algorithm searched through values of height from $100 \mu m$ to $140 \mu m$ since it was expected that the optimal dimension for the beam height would occur within this region based upon previous investigations of

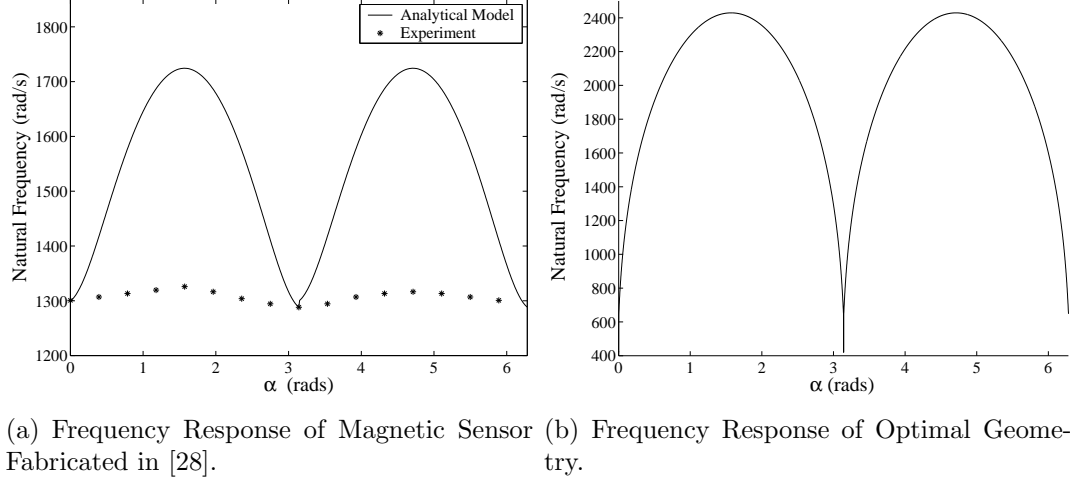


Figure 24: Comparison of System Performance due to Beam Optimization.

beam optimization.

Other system variables were used to describe the magnetic sensor during optimization routine and remained constant throughout the entire search of the workspace. The radius of the central disk that supports the magnet and connects to the three beams in the sensor is $1000 \mu m$. The outer radius of the comb drives within the system is $2400 \mu m$. The magnet model used in the algorithm is cylindrical in geometry with a diameter of $800 \mu m$ and thickness of $800 \mu m$. The strength of the magnetic field interaction is modeled as $7.2 * 10^{-8}$ as presented in [28].

Figure 23 displays a plot of the objective function from the routine as it steps through the work space. It is assumed that the manufacturing tolerance that can be achieved during the fabrication of the magnetic sensor at Georgia Tech is $\pm 0.5 \mu m$. From the results shown in Figure 23, the optimal height of the beams is found to be $120.5 \mu m$. Further investigation of the system at this dimension shows that the requirement that the limiting constraint on the optimal height of the beam is the resonant frequency of the device in the z-direction. Through a more detailed analysis of the coupling between the two vibration modes within the sensor, it may be possible to relax the constraint and allow for greater increase the sensitivity of the device.

Figure 24(b) shows the response of the linear natural frequency for the optimized

system versus changes in the external field orientation α . The sensitivity of the linear natural frequency has the same general shape as the experimental results presented in [28] as shown in Figure 24(a). While the experimental results do not match the resonant frequencies predicted by the model for the device in [28], the modeling results can still be used for comparison since it is expected that the same trend improvement with the optimized device will be seen when it is fabricated.

Some sources of error between the model and experimental results from [28] are the magnetic torque model used within the device and also the ideal clamped-clamped boundary conditions used to model the beams within the sensor. The silicon that is used within the optimized device is much stiffer than the Su-8 used in [28] and the clamped-clamped boundary conditions have been shown through experiment to be valid. The modeling of the nonlinear beam mechanics has also been shown to be an acceptable match to the experimental results as shown in Section 3.5.2. Deviations from the model seen in future experiments will most likely come from the modeling of the magnetic torque in the sensor. The modeling of the magnetic torque was not addressed in this thesis. Nonetheless, predicted improvements in resolution due to the optimized sensor design should result in improvements in the resolution when the devices are constructed and compared with the experimental results from [28].

To quantify the improvement in the sensitivity of the sensor due the redesign and optimization, the resolution of the optimized device is compared with the sensitivity predicted by the model for the sensor presented in [28]. The resolution of the sensor is defined as the number of radians from $\alpha = \frac{\pi}{2}$ that are required in order for a $1 \frac{\text{radian}}{\text{second}}$ change in the linear natural frequency of the device. Table 4.3 provides a comparison of the resolution predicted by the model for the device in [28] and the new magnetic sensor design with optimal beam dimensions.

The improvement in the sensitivity of the sensor has occurred over the entire working range of α and also in regions near $\alpha = \frac{\pi}{2}$. An increase of nonlinear behavior

Table 2: Comparison of Sensor Resolutions.

<i>Device</i>	Resolution (radians)	Improvement
Model of Device in [28]	.0656	0
Optimized Passive Design	.0538	22 %

and therefore the sensitivity of the magnetic sensor via optimization of the beam dimensions of the sensor have been shown to improve the performance of the magnetic sensor.

It has been shown through simulation that driving the beam spring elements in the system into large deflection behavior will result in an increase in the sensitivity of the magnetic sensor to changes in the orientation of external magnetic fields. Improvements to the sensor sensitivity are coupled to increases in the nonlinear behavior and based upon the results from modeling. Improvements to the sensitivity of the magnetic sensor have been realized through the optimization of beam geometry to increase their nonlinear behavior. Through the implementation of the exhaustive search of the design space for the heights of the sensor beams, the optimal beam height was found to be $120.5 \mu m$ with a beam length and width of $2000 \mu m$ and $5 \mu m$ respectively. Other techniques to increase the nonlinear behavior of the sensor will result in for further increases in the sensitivity that can be achieved by the magnetic sensor.

CHAPTER V

DESIGN OF ACTIVE SENSOR COMPONENTS

In this chapter the application of variable force, or shaped, comb drives to the magnetic sensor are proposed to improve the performance of the sensor. The use of shaped comb drives is applied to the magnetic sensor in order to increase the nonlinear dynamics of the device beyond what can be achieved through the passive optimization of the beams in the sensor. The comb drive will modify the dynamic behavior of the sensor and lead to improved sensitivity of the device over what has been achieved through the optimization of the beam dimensions.

5.1 Related Work

Comb drives are frequently used in MEMS devices as a means of exciting devices to resonance and also to detect device behavior such as position or vibration. Figure 25 shows an example of a generic comb drive within a MEMS device. The force in the comb drive acts in a direction parallel with the plates, or comb fingers of the drive. Comb drives that generate forces that vary with insertion depth of the moving comb finger have been developed to as a means of modifying the resonant frequency of gyroscopes [40].

Further comb drive research has shown that shaping the geometry of the comb drive finger will result in force profiles that are polynomial in form [51]. This approach has been applied to resonating MEMS devices as a means of modifying the natural frequency of a system by increasing or decreasing the linear stiffness of system [25]. Since the force generated by the shaped comb drive is dependent upon position, the shaped comb drives act as spring elements in the system dynamics. The concept of

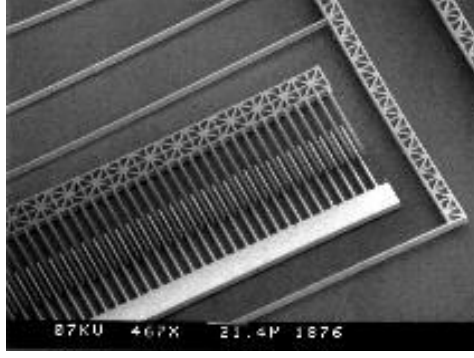


Figure 25: Scanning Electron Microscope Picture of a Comb Drive Actuator [13].

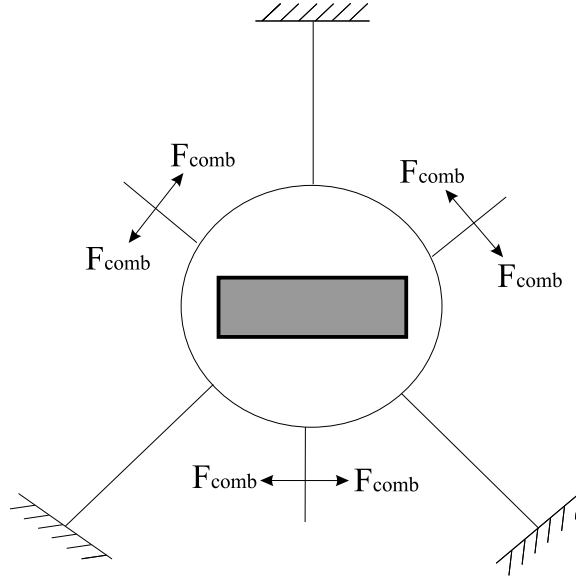


Figure 26: Proposed Addition of Comb Drive Elements to Sensor Design.

using shaped comb drive actuators to further modify the nonlinear stiffness within resonators has been presented in [3]. The authors found that the linear and nonlinear stiffness of a system could be modified independently through the proper design of the shaped comb drives. This approach will be used in the design of the shaped comb drives to modify both the linear and nonlinear behavior of the magnetic sensor.

Figure 26 shows a diagram of how forces from the shaped comb drive elements can be added to the magnetic sensor to modify its behavior. The force of the shaped comb drives are dependent upon the rotation of the magnetic sensor and will modify the system dynamics by acting as springs within the system to provide a restoring

torque when central disk is rotated.

5.2 Principles of Shaped Comb Drives

The development of a model to describe the behavior of the shaped comb drives will be presented in this section. As stated in Section 3.2.4, the approximate driving force between the moving and stationary finger for a comb drive with a constant gap is:

$$F \approx \varepsilon_0 \cdot \frac{h \cdot V^2}{gap}, \quad (100)$$

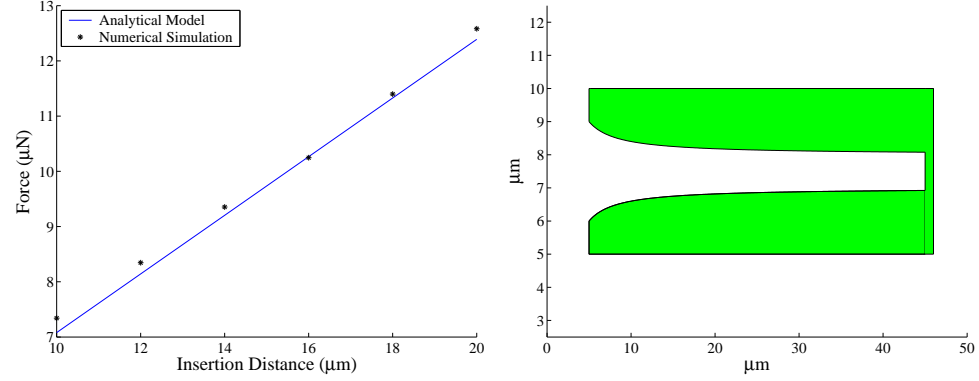
In order to design a comb drive with a variable force that is a function of the position of the moving finger, the gap between the two comb fingers or the voltage across the comb fingers must be vary in relation to insertion depth of the moving finger. Altering the voltage across the combs as a function of the position of the moving finger is undesirable since it would require complex signal processing and a feedback control for operation. Along with improving the sensitivity of the sensor and reducing its size, another design goal for the sensor is to minimize the power requirement of the sensor. Therefore varying the shape of the comb drive is chosen as the technique to generate variable force profile comb drives to reduce the power requirement.

To generate a comb drive with a force profile that varies with the insertion of the moving finger in the form of a polynomial, the gap between the two fingers is modified to be an inverse polynomial of the form [51]:

$$gap(x) = \frac{1}{C_0 + C_1 \cdot x + C_2 \cdot x^2 + C_3 \cdot x^3} \quad (101)$$

where x is insertion depth of the moving comb finger starting at zero from the tip of the stationary finger as shown in Fig. 9. The coefficients C_z in (101) relate to the force of the comb drive in (100) such that:

$$F(x) \approx \varepsilon_0 \cdot h \cdot V^2 \cdot (C_0 + C_1 \cdot x + C_2 \cdot x^2 + C_3 \cdot x^3). \quad (102)$$



(a) Comparison: Analytical Model versus Numerical Simulation.

(b) Comb Drive Geometry.

Figure 27: Linear Comb Drive.

Table 3: System Parameters for a Linear Stiffening Comb Drive.

C_0	1
C_1	.3
Voltage	100 V
h	$20 \mu m$

To design a comb drive that generate a linear force profile, the gap of between the moving and stationary fingers will take the form:

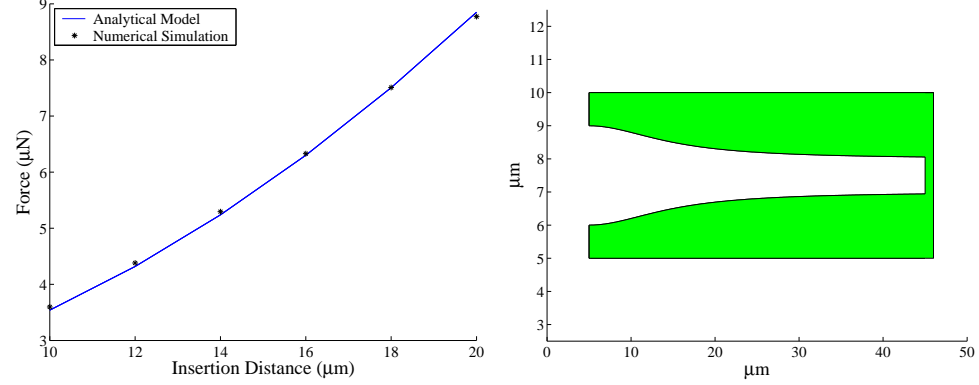
$$gap(x) = \frac{1}{C_0 + C_1 \cdot x} \quad (103)$$

The value of C_1 can be either positive or negative in order to create a linear stiffening or linear softening shaped comb drive [25]. Figure 27(a) shows the a comparison of force predicted by equation (102) for a linear stiffening shaped comb drive with the results from numerical simulation. The geometry of the shaped comb drive can be seen in Figure 27(b). The gap of the comb drive is in the form of(103) and the parameters that specify the geometry of the shaped comb drive are shown in Table 5.2.

Figure 28(a) presents the force profile for the quadratic force profile comb drive shown in Figure 28(b). The gap between the moving and stationary fingers is:

$$gap(x) = \frac{1}{C_0 + C_2 \cdot x^2} \quad (104)$$

where the coefficients that determine system geometry are shown in Table 5.2.



(a) Comparison: Analytical Model versus Numerical Simulation.

(b) Comb Drive Geometry.

Figure 28: Quadratic Comb Drive.

Table 4: System Parameters for a Quadratic Stiffening Comb Drive.

C_0	1
C_2	.01
Voltage	100 V
h	20 μm

Figure 29(a) presents the force profile for the quadratic force profile comb drive shown in Figure 29(b). The gap between the moving and unmoving fingers is:

$$gap(x) = \frac{1}{C_0 + C_3 \cdot x^3}. \quad (105)$$

The coefficients that specify the system geometry are presented in Table 5.2.

From Figures 27(a), 28(a), and 29(b) it can be seen that the comb drive behavior predicted by the analytical model compares well with numerical simulation. Therefore the analytical model will be used to model the behavior of the shaped comb drives within the magnetic sensor simulation. However, there are limits on comb drive dimensions that affect how accurately the model will approximate the behavior of the comb drive, primarily that the gap of the comb drive must be reasonably small. Further limits on the accuracy of the analytical model will be discussed in the next section.

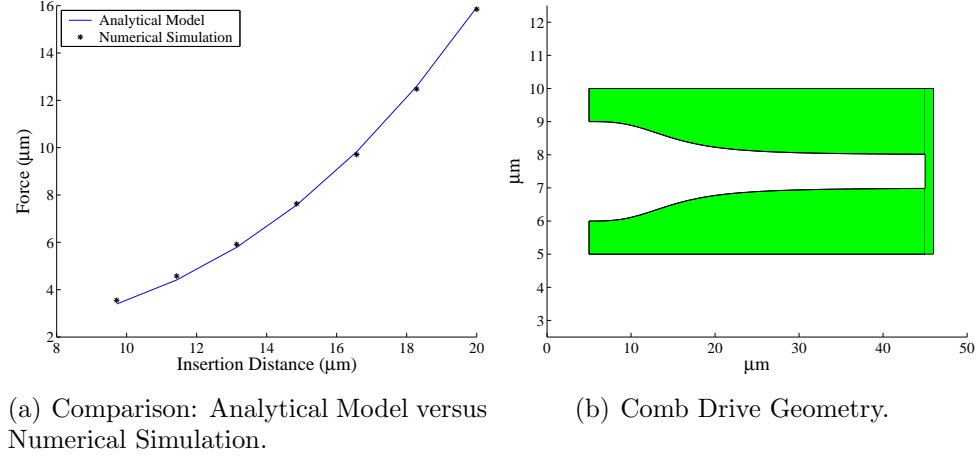


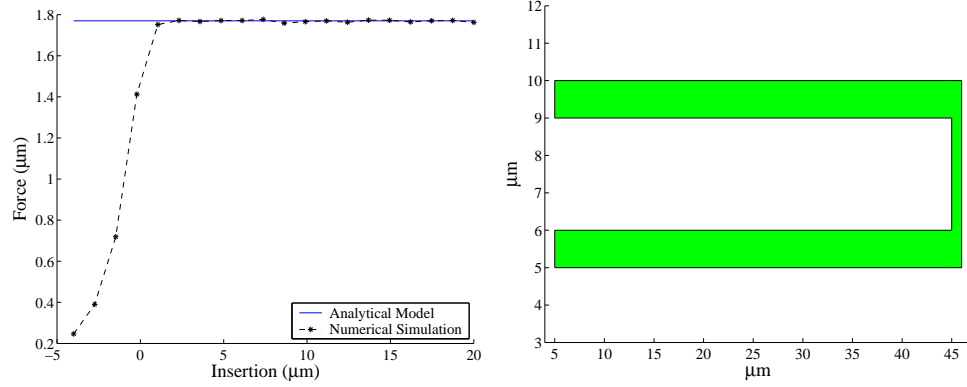
Figure 29: Cubic Comb Drive.

Table 5: System Parameters for a Cubic Stiffening Comb Drive.

C_0	1
C_3	.001
Voltage	100 V
h	20 μm

5.2.1 Analytical Model Limitations

Based upon the numerical simulation of the shaped comb drives, the boundaries were developed to determine the comb drive characteristics that must be enforced in order for the analytical model to represent the behavior of the comb set. The example used to describe the limitations of the model is the constant force comb drive shown in Figure 30(b). It can be seen in Figure 30(a) that the behavior of the shaped comb fingers does not display the same behavior as predicted by the analytical model until the moving finger has been inserted approximately 2 μm . The parameters that describe the device are shown in Table 5.2.1. The insertion up to this position represents a transition region where the in-plane fringing fields from the tips of the moving and stationary fingers are changing, which results in a large change in the electrostatic force of the comb drive. After the moving finger has been inserted beyond the transition region, the one dimensional effects of the comb drive gap become



(a) Comparison: Analytical Model versus Numerical Simulation.

(b) Comb Drive Geometry.

Figure 30: Insertion Distance Limitation of the Analytical Model.

Table 6: System Parameters for a Constant Force Comb Drive.

C_0	1
Voltage	100 V
h	20 μm

the dominant comb parameter that determines the change in the electrostatic force between the moving and stationary comb fingers. The analytical model can then be used to predict the behavior of the shaped comb drive with reasonable accuracy. As the moving reaches full insertion, the fringing fields from the tip of the finger will change again and will cause an increase in the electrostatic force of the comb finger that is not addressed by the model. The shaped comb drives used within the sensor will not be operated at full insertion, therefore only the transition region for the initial insertion of the moving finger is considered when applying the analytical equation to model the comb drive behavior.

Other geometry considerations that affect the validity of equation (102) for use as an analytical model of comb drive behavior are the height of the comb drive and the length of the fingers. The one dimensional model of the comb drive force assumes that the height of the comb drive is much greater than the gap between the moving and stationary fingers. If a poor aspect ratio of gap to height is used, the fringing

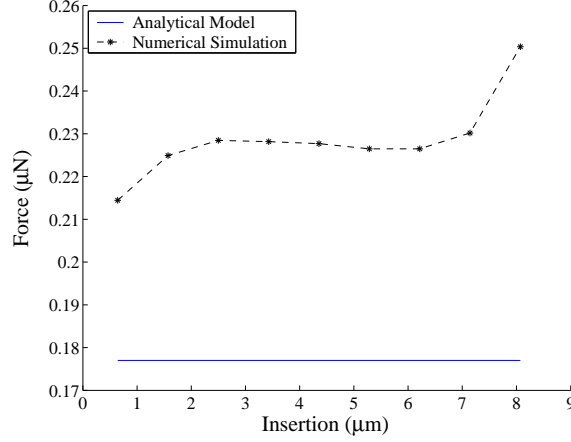


Figure 31: Poor Height Aspect Ratio: Analytical Model versus Numerical Simulation.

fields from out-of-gap interactions between the two bodies are no longer negligible and the gap between the two bodies is no longer the dominate parameter that will determine the electrostatic force between the two bodies. For such a comb drive, the electrostatic force cannot be accurately predicted with equation (100).

Figure 31 shows how the comb drive model compares to the numerical simulation for a comb drive with a gap to height aspect ratio of 2. The force calculated by the model is less than the value from the numerical simulation due to the increased influence of out-of-gap fringing fields on the force profile of the comb drive. By maintaining an gap to height ratio of at least **10** for the shaped comb drives that will be used within the magnetic sensor, the model can be used as an analytical representation of the shaped comb drive element within the device simulations.

The ratio of the gap width to the length of the comb fingers is another factor that must be considered when applying the analytical model to determine comb drive behavior. As the ratio of the gap to the finger length decreases, the analytical model no longer provides a good approximation for the behavior of the comb drive since the moving finger no longer operates over a region where the change in the fringing fields from the moving tip remains fairly constant. This type of behavior can be seen in Figure 32(a) which represents the force on the moving finger for the comb drive

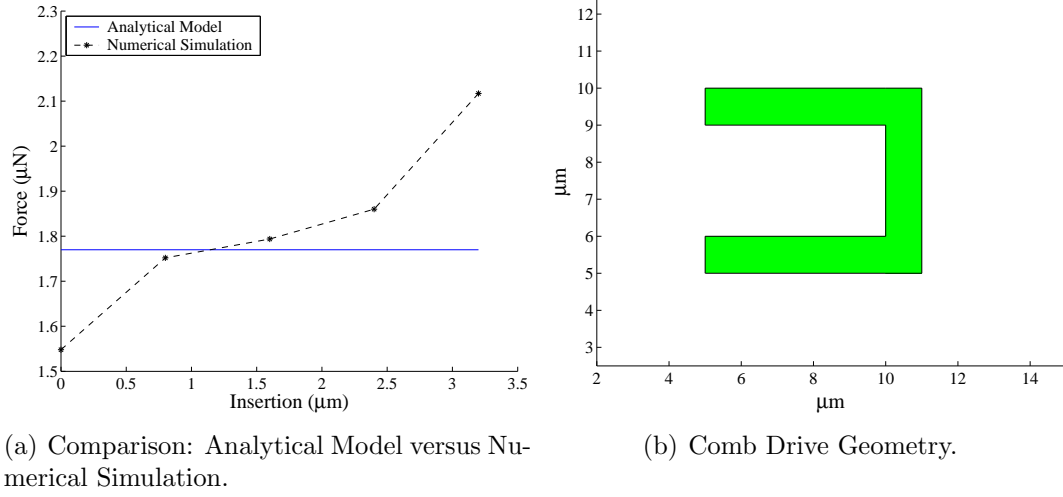


Figure 32: Limitation of the Analytical Model due to Finger Length: Constant Force Profile.

shown in Figure 32(b) with finger length to gap ratio of 5. By maintaining a ratio of at least **40**, as in Figure 30(b) the analytical equation will provide a good prediction of the comb drive behavior as the gap between the two comb drive components will be the dominant parameter that affects behavior of the comb drive.

5.3 Application to the Magnetic Sensor

Through the use of shaped comb drives, the dynamics of the magnetic sensor can be modified to increase the sensitivity of the sensor by increasing the nonlinear behavior of the device. By solving for the electrostatic behavior of the shaped comb drives external to the dynamic equation of the magnetic sensor, the comb drive effects can be represented by spring elements within the system equation in the same manner as the beam elements presented in Section 3.2.1. Figure 33 shows a diagram of the sensor presented as a mass-spring system with the inclusion of the shaped comb drive effects where K_{beam} and K_{comb} terms are the effective stiffness of the beams and shaped comb drives within the magnetic sensor. The dynamic equation incorporating the effects of

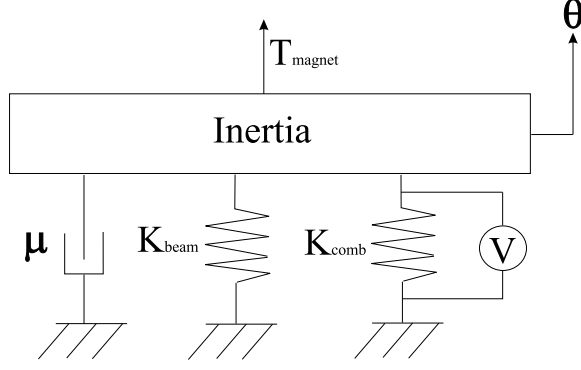


Figure 33: Mass-Spring-Damper Representation of the Magnetic Sensor.

the comb drive will be:

$$I \cdot \frac{d\theta_d^2}{dt^2} + \mu \cdot \frac{d\theta_d}{dt} = \begin{cases} T \sin(\alpha - \theta_d) - (K_L \theta_d + K_Q \theta_d^2 + K_C \theta_d^3) \\ -K_{CombL} \theta_d - K_{CombQ} \theta_d^2 - K_{CombC} \theta_d^3 \end{cases} \quad (106)$$

where K_L , K_Q , and K_C are stiffness coefficients from the beams within the sensor and K_{CombL} , K_{CombQ} , K_{CombC} are the stiffness coefficients from the shaped comb drives. The comb drives provide a lateral resistance force to the rotation of the sensor and are therefore incorporated as a modification to the lateral stiffness, P , of the beams within the magnetic sensor model. Their contribution to dynamics of the sensor are therefore modeled as

$$T_P = (P + F_{comb}) \cdot R \cdot \sin(\theta_d + \theta_0), \quad (107)$$

where P is the lateral stiffness coefficients from the beam and F_{comb} is the effective lateral stiffness due to the shaped comb drives.

5.3.1 Comb Drive Shape Sensitivity Study

A study of the shaped comb drive coefficients was performed to understand how modifications to the different stiffness coefficients in the system would affect the sensitivity of the sensor. The study was performed with the assumption that the shaped comb drives would represent a change in the lateral stiffness of the beams as

derived in equation (37). The values of K_L , K_Q , and K_C , which represent the lateral stiffness coefficients of the beams in the sensor were modified by scalar multiples.

Section 4 showed that increases in the static equilibrium angle θ_0 is directly correlated with increases in sensitivity of the magnetic sensor. Therefore it was expected that a negative value for K_{CombL} would improve system sensitivity since this would allow the value of θ_0 to increase due to a decrease in the linear stiffness of the system. It was also expected that increasing the nonlinearity of the system through K_{CombQ} and K_{CombC} would result in an increase in performance. However, it was not obvious as to whether changes to the cubic stiffness or the quadratic stiffness would have the greatest effect on the system sensitivity.

The magnitude of the magnetic torque used within the simulations is $T_{mag} = 7.96 * 10^{-10} \text{ N} \cdot \text{m}$. The beams used for the sensitivity study have a length, width, and height of $2000 \text{ } \mu\text{m}$, $5 \text{ } \mu\text{m}$ and $52 \text{ } \mu\text{m}$ respectively. The coefficients used to describe the lateral stiffness of a single beam are:

$$\begin{aligned} K_L &= 0.1823 \\ K_Q &= 2.0320 * 10^4 \\ K_C &= 7.9802 * 10^9 \end{aligned}$$

Figure 34(a) shows the variations in the linear natural frequencies for systems containing linear profile comb drives. Improvements to the sensitivity of the system in the region least sensitive to changes in α near $\frac{\pi}{2}$ cannot be clearly seen in Figure 34(a). By displaying the change in natural frequency versus α as shown in Figure 34(b), the effects of changes in the linear stiffness in the sensitivity of the sensor can be more easily seen. The regions that experience the largest change in sensitivity from the application of the linear comb drives are located near $\alpha = 0$ and $\alpha = \pi$. Even in the region near $\alpha = \frac{\pi}{2}$, where the change in the sensitivity of the sensor is minimal, an increase in the change in frequency can be seen.

Table 7: Comparison of Sensitivity with Shaped Comb Drive Contributions

α	K_L Multiplier	K_Q Multiplier	Δf	% Improvement
0	1	1	.334	0.0
0	.5	1	.494	.160
0	1	1.5	.398	.060
0	.5	1.5	.588	.254
$\frac{\pi}{2}$	1	1	.059	0.0
$\frac{\pi}{2}$.5	1	.089	.030
$\frac{\pi}{2}$	1	1.51	.068	.009
$\frac{\pi}{2}$.5	1.5	.101	.042

From Figure 35(a) it can be seen that increases in the quadratic nonlinearity of the lateral stiffness of the sensor will increase the natural frequency of the sensor over the entire range $0 < \alpha < \pi$ while maintaining the same natural frequency at $\alpha = 0$ radians and $\alpha = \pi$ radians. The improvement of the sensitivity of the sensor due to the application of the quadratic comb drive as shown in Figure 35(b) is similar that of applying a linear comb drive in the region near $\frac{\pi}{2}$, but the change is less in the regions $\alpha = 0$ radians and $\alpha = \pi$ radians. Figures 36(a) and 36(b) show that modifications of the cubic stiffness of the system will not result in a significant change in the resonant behavior of the system. Therefore it is not advisable to design shaped comb drives with a cubic force profile.

The combination of softening linear and stiffening quadratic profiles in the same comb drive will result in greater improvement in the system performance than the application of a single type of force. A comparison of the improvements in the sensitivity of the sensor due to the presence of the shaped comb drives is shown Figure 37. Table 5.3.1 presents the change in natural frequency at two different values of α and shows that the combination of the linear and quadratic force profiles within the same system will result in an improvement in the sensitivity of the system that is greater than what can be achieved through the individual application each force profile. This behavior is due to the coupling between the increase of nonlinear behavior of the

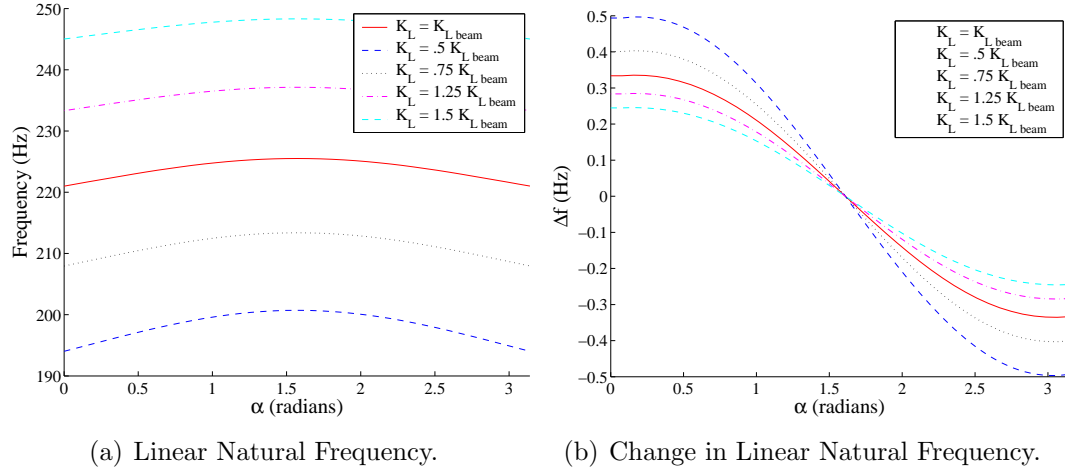


Figure 34: Variations in Linear Stiffness.

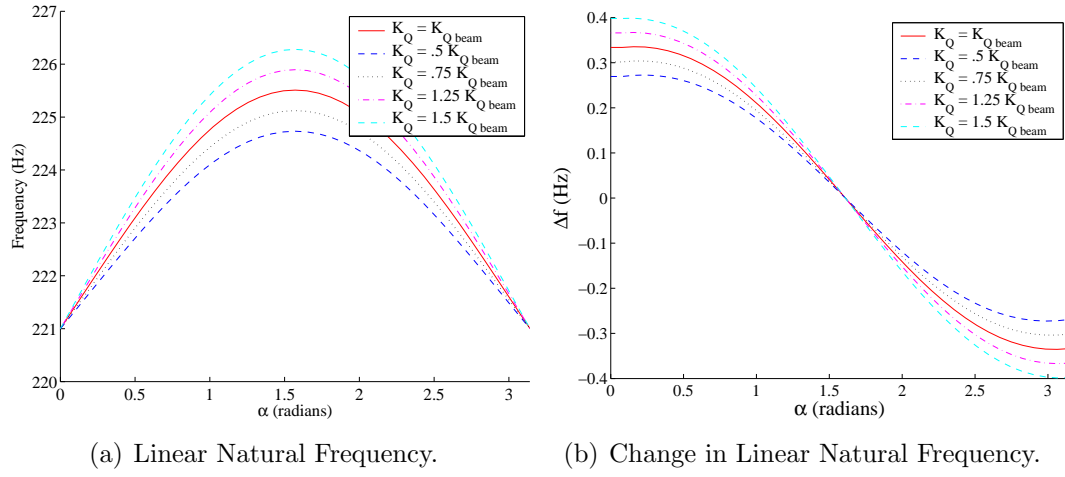


Figure 35: Variations in Quadratic Stiffness.

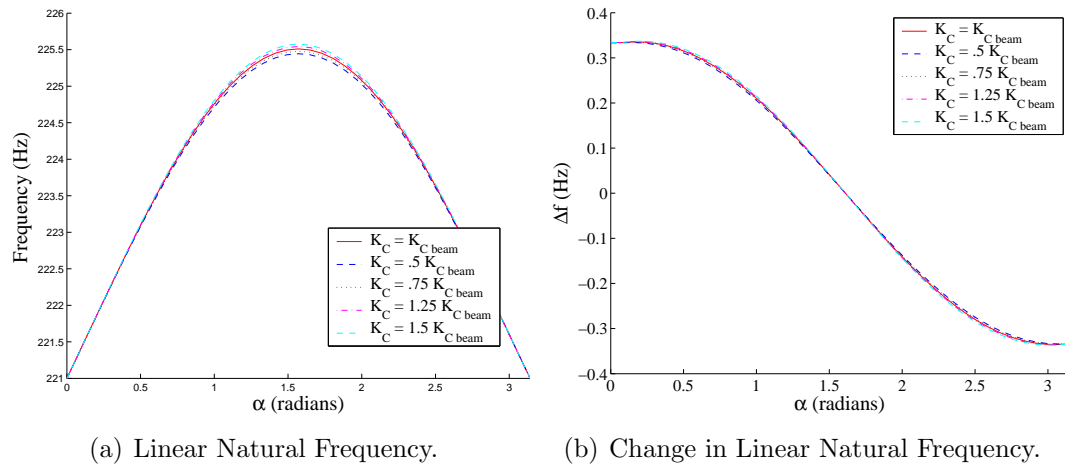


Figure 36: Variations in Cubic Stiffness.

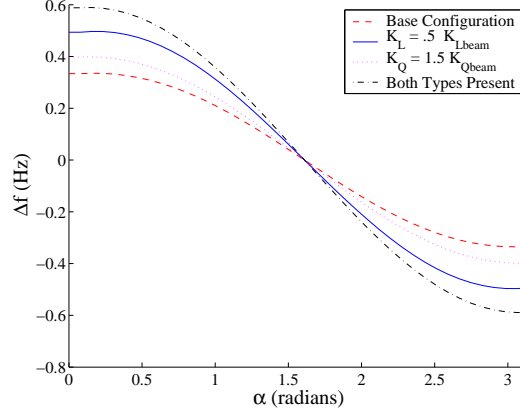


Figure 37: Comparison of Changes in Natural Frequency for Multiple Comb Drive Combinations.

system from the increase of the quadratic stiffness and the reduction the linear stiffness, which will all the system to quicker enter the region of where the effects of the nonlinear stiffness are on the same order as the effects due to the linear stiffness.

If the method used to detect the frequency of the system is able to detect changes in the natural frequency at a resolution of 1 Hz, then the application of a cubic and linear comb drive would result in an increase in the resolution of the sensor from ± 0.7156 radians to ± 0.5061 radians. It is expected that the use of frequency detection techniques with resolutions higher than 1 Hz would show further improvements in the calculated resolution of the magnetic sensor. Based upon the results of the sensitivity study, the application of comb drives containing both negative K_L and positive K_Q stiffness would achieve the best improvement in the sensitivity and overall performance of the magnetic sensor. With the application of shaped comb drives that are able to modify the sensor dynamics to achieve even larger values of K_Q and lower values of K_L , further performance increases in the magnetic sensor can be expected over the improvements shown in this example.

5.4 Design of a Variable Shaped Comb Drive

Now that the characteristics of the shaped comb drives and the limits of the applicability of the model are known, shaped comb drives can be designed and added to the model of the magnetic sensor as a means of improving the performance of the device. In order to incorporate the shaped comb drives into the optimization of the magnetic sensor, an algorithm was developed to optimize the comb drives that will represent a sub-optimization problem within the optimization problem for the entire magnetic sensor.

The gap profile of the shaped comb drives has been optimized to ensure that each comb finger within the comb drive set has its maximum potential for modifying the system behavior while maintaining the fabrication and operating constraints that are placed on the drives. An optimization routine was developed in MATLAB to determine the optimal gap values of C_1 and C_2 that would simultaneously maximize the quadratic force profile and minimize the negative linear force profile of the shaped comb drive. The *Fmincon* function in MATLAB was used to optimize the gap geometry of for each of the comb fingers within the comb drive and also maintain the geometric constraints. The MATLAB function mimics Newton's method for unconstrained optimization and is based on an implementation of sequential quadratic programming, SQP [35].

The SQP technique is an effective method of solving nonlinear optimization problems with nonlinear constraints and transforms the system into a series of quadratic problems with linear constraints. The quadratic problem formulations and linearization of the constraints are both done within the MATLAB function. The SQP method is well suited for optimizing the comb finger sets due to the presence of nonlinearities within the system. Another benefit of the method is its robustness to infeasible start points that violate system constraints. This will allow for the maximum force profile to be found for comb finger sets with a variety of constraints by using the same

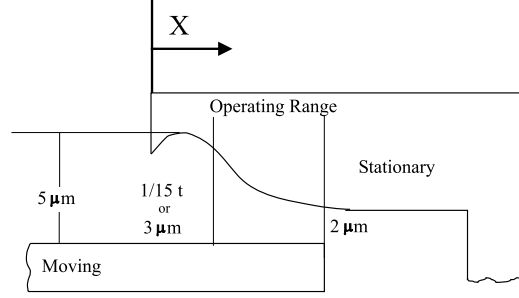


Figure 38: Gap Constraints for a Shaped Comb Finger.

starting point for the initial guess of the optimal shaped comb finger dimensions.

5.4.1 Shaped Comb Finger Constraints

A diagram of the gap constraints for each comb finger can be seen in Figure 38 and each constraint will be described in the following section. By increasing the number of comb finger sets in the comb drive, the force that can be applied by a comb drive increases and the torque that can be applied by the comb drive greatly increases as the additional comb finger sets are located farther and farther from the center of rotation of the magnetic sensor. While it would be advantageous to allow for comb drives with great lengths to increase the moment arm of each comb finger set, the maximum length constraint was implemented to place an upper limit on the size of the sensor. The first constraint implemented in the algorithm is that the length of the comb drive cannot be greater than $2000 \mu m$, which was also used as the constraint for the maximum beam length during the optimization of the magnetic sensor in Chapter 4. It is expected that future design iterations will decrease the length in order to further reduce the size of the magnetic sensor.

The gap between the moving and stationary comb fingers at the start and end of the operating range of the each comb finger set is the second constraint implemented in the shaped comb drive optimization algorithm. The operating range of each comb finger set represents the path that will be taken by the moving comb finger during sensor operation. The start of the operating range represents the initial insertion of

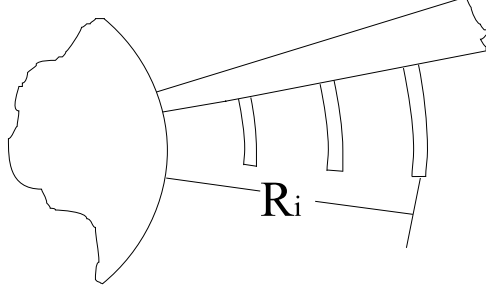


Figure 39: Diagram of Radius Evaluation for Comb Fingers.

the moving comb fingers from fabrication and was chosen to be $10 \mu m$ for all comb finger sets within the comb drive. The reactive ion etching process that is used to fabricate the device requires that the minimum gap between two objects within the sensor is $\frac{1}{15}$ of the height of the sensor. Therefore the constraint on gap at the start of the operating range for all of the comb finger sets is $\frac{1}{15}$ of the height or $3 \mu m$, whichever is greater. The constraint that the minimum gap at the start of the operating range must be at least $3 \mu m$ has been imposed to ensure that there will be a change in the gap of at least $1 \mu m$ across the operating range of the comb finger set.

The end of the operating range of each comb finger set is found by simulating the static response of the sensor to a magnetic torque. The maximum static equilibrium angle, θ_{0max} , of the device when the external magnetic field is at an orientation $\alpha = \frac{\pi}{2}$ is used to determine the end of the operating range since θ_0 is at its maximum at for this value of α . Since each comb finger set in the comb drive is located at a different distance from the center of rotation of the disk, the same value for θ_{0max} will result in different operating ranges for each set. The end of the operating range for each comb finger set is based upon the distance of the moving comb finger from the center of rotation of the sensor and θ_{0max} such that:

$$\text{OperatingRange}_{end} = R_i \cdot \theta_{0max}, \quad (108)$$

where R_i is the radial distance of the moving finger in each comb finger set from the center of the rotation as shown in Figure 39. The constraint imposed upon the system

for the gap at the end of the operating range is that it must be greater than $2 \mu m$ to ensure that there is no side-instability in the comb finger set. Side-instability could lead to device failure if two fingers in a comb finger set come into contact during operation, which will cause a short across the comb drive.

The width of the comb fingers will be designed as $10 \mu m$. The maximum gap that is allowed is based upon the initial gap at an insertion of zero and is chosen to be:

$$gap_{max} = \frac{1}{C_0} + 2.5\mu m, \quad (109)$$

to ensure that the minimum feature size constraint of $5 \mu m$ is maintained.

5.4.2 Objective Function

The objective function and constraints are implemented to optimize each comb finger set separately and determine the geometry that will result in the largest possible quadratic stiffness coefficient and most negative linear stiffness coefficient for each comb finger set within the shaped comb drive. Maximization of the quadratic stiffness is achieved by maximizing the C_2 coefficient used to determine the gap profile of each shaped comb finger. The most negative linear stiffness is realized by minimizing the C_1 coefficient of the gap profile for each finger. Through the combination of a negative C_1 and a positive C_2 in a single shaped comb finger, both terms can attain more extreme values than if they were each applied to separate comb fingers.

The objective function to be minimized during the optimization the each shaped comb finger is:

$$obj = (Ci_1 - C_1)^2 + (Ci_2 - C_2)^2, \quad (110)$$

where Ci_1 and Ci_2 are the initial coefficient guesses of -1 and 10 respectively. The initial guess that is used for C_2 is much larger than what can be achieved and the guess for C_1 is much less than can be achieved with the application of the constraints. This approach ensures that the initial guess for the gap profile of each comb finger is

infeasible and can be used to optimize all of the comb finger sets within the shaped comb drive. As the value for C_1 and C_2 approach the values for the initial guesses, the objective function will decrease in value since it evaluates the difference between the two sets of coefficients. By minimizing the objective function, the maximum value for C_2 and the minimum value of C_1 for each shaped finger will be found. This will result in maximizing the quadratic stiffness coefficient while also minimizing the negative linear stiffness coefficient of each shaped finger. The order of the coefficients for the linear and quadratic stiffness terms is different due the difference in the magnitude of the two terms. The extra weighting of C_2 is acceptable since modifications of quadratic stiffness were shown in Section 5.3.1 to result in a greater increase in the sensitivity of the magnetic sensor.

5.4.3 Optimization Routine

The final portion of the comb drive algorithm combines the profiles found with the gap optimization for each comb finger to determine the total torque and force profiles for the comb drive as a whole. The constant torque that is applied by the comb drive due to existence of C_0 has been shown to be negligible when compared with other effects in the magnetic sensor so its contribution to the comb drive dynamics is ignored. The coefficients for the comb drive are found by adding the coefficients from each individual comb finger set such that:

$$T_L = \sum_{i=1}^n C_1(i) \cdot \varepsilon \cdot h \cdot V^2 \cdot (R_{\text{comb}}(i))^2 \quad (111)$$

$$T_Q = \sum_{i=1}^n C_2(i) \cdot \varepsilon \cdot h \cdot V^2 \cdot (R_{\text{comb}}(i))^3 \quad (112)$$

where the total torque that can be generated by the shaped comb drive is:

$$Torque = T_L \cdot \theta + T_Q \cdot \theta^2. \quad (113)$$

The values for T_L , T_Q are calculated based upon the force of each comb finger set in the shaped comb drive by multiplying the shaped comb drive force from equation (102) by

the radial distance, R_i of each comb finger set. The torque coefficients are converted to lateral motion coefficients to allow for implementation within the sensor model as a modification of the lateral stiffness coefficient for the beams within the magnetic sensor. The conversion from torque coefficients to lateral stiffness coefficients is:

$$K_{CombL} = T_L \cdot R^{-2} \quad (114)$$

$$K_{CombQ} = T_Q \cdot R^{-3} \quad (115)$$

It is assumed that the number of shaped comb drives spring within the sensor is equal the number of beams in the device so effects of shaped comb drives will be included in the system model as a modification of lateral stiffness coefficients such that:

$$K_{Lsys} = K_{Lp} + K_{CombL}$$

$$K_{Qsys} = K_{Qp} + K_{CombQ}$$

where K_{Lsys} and K_{Qsys} substituted into the equations for the restoring torques in the sensor calculated in (40), (41), and (42) in Chapter 3 in place of the lateral stiffness coefficients of the beams K_{Lp} and K_{Qp} .

After the force profile of the shaped comb drive has been calculated, the algorithm is run again to correct for the change in the operating range that will occur due to the modification of the stiffness of the system. The changes in the operating range will allow for further optimization of the stiffness coefficients of the comb drive. Once the change in the comb drive forces between iterations is significantly small, the algorithm terminates and the optimal solution for the comb finger set dimensions and the force profile of shaped comb drive has been found. The lateral stiffness coefficients for the comb drive and the geometry of each comb finger set within the comb drive are the two outputs that are sent back to the main program after the optimization routine is completed. Figure 40 shows a flowchart of the steps within the algorithm that are taken to convert the input of the magnetic sensor parameters and the voltage of the

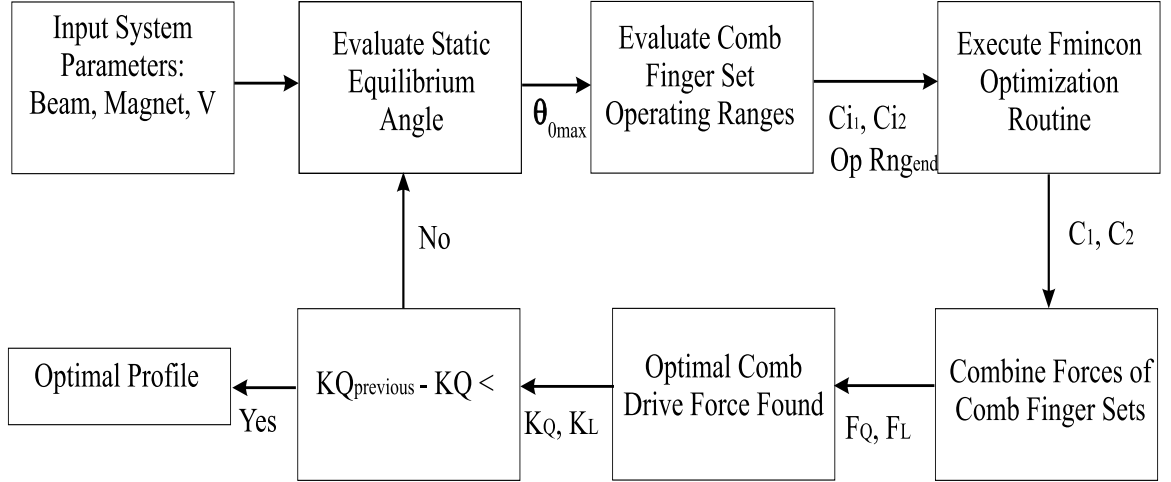


Figure 40: Flowchart of Comb Drive Optimization Code.

Table 8: Shaped Comb Drive Objective Function and Constraints

Objective Function
$\text{obj} = (Ci_1 - Ci_1)^2 + (Cd_2 - C_2)^2$
Constraints
Maximum Gap $< 5 \mu m$
Minimum Gap: Start of Operating Range $> \frac{1}{15} h$ or $3 \mu m$
Minimum Gap: End of Operating Range $> 2 \mu m$

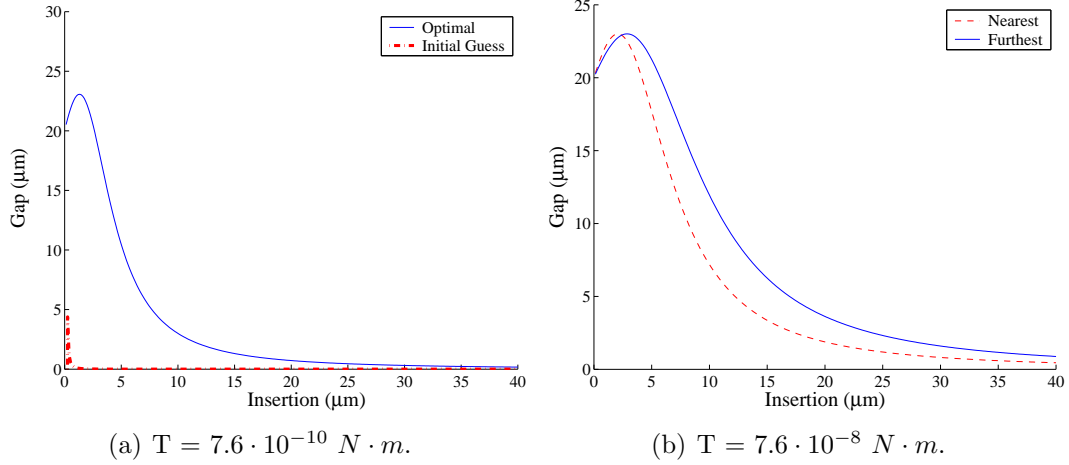


Figure 41: Optimal Gap Profile for Sensor in Section 4.

Table 9: Comparison of Sensitivity with Shaped Comb Drive Contributions

Coefficient Source	K_L	K_Q	K_C
Beam	0.1823	$2.0320 \cdot 10^4$	$7.9802 \cdot 10^9$
Shaped Comb Drive	-0.1428	$8.9273 \cdot 10^5$	0
Change	78%	439.3%	0%

shaped comb drive into the optimal geometry profiles of each comb finger and the optimal force profile of comb drive. The objective function and system constraints are shown in Table 5.4.3.

Figure 41(a) shows the optimal gap profile for a comb drive attached to an example device with beam dimensions of length, width and height of $2000 \mu\text{m}$, $5 \mu\text{m}$, and $52 \mu\text{m}$ respectively. The magnitude of the magnetic torque T used within the example is $7.96 \cdot 10^{-10}$ and the value for C_0 is 0.05. Through the implementation of the *fmincon* optimization routine in MATLAB, the the optimal value of C_1 for all of the comb finger sets is found to be -0.01015 and the optimal value of C_2 is 0.003845. The initial guess for desired geometric profile corresponding to C_1 and C_2 for the optimal comb drive profile is also shown in the Figure 41(a) and violates the geometric constraints placed on the system since the gap is less than $2 \mu\text{m}$ at an insertion distance of less than $1 \mu\text{m}$.

The optimal force coefficients for a shaped comb drive with a voltage of 25V and 18 shaped comb fingers are presented in Table 5.4.3 along with the beam stiffness coefficients that will be modified by their use. The maximum quadratic stiffness that can be achieved without the negative linear stiffness is $F_Q = 6.5787 * 10^4$ which is a 26% reduction in the quadratic stiffness that can be achieved by the shaped comb drive with the inclusion of the linear stiffness.

It can be seen in Figure 41(a) that the optimal geometric profiles for all of the comb finger sets within the comb drive are the same for this example. This result is due to the gap at the start of the comb finger operating range acting as the limiting constraint on the profile of each comb finger set. For a sensor with a stronger permanent magnet or in the presence of a larger external magnetic field where T increases from $7.6 * 10^{-10}$ to $7.6 * 10^{-8} \text{ N} \cdot \text{m}$, the limiting constraint on the comb finger geometries is no longer the gap at the start of the operating range, but is instead the gap at the end of the operating range. The effect of the different value for T can be seen in Figure 41(b) where the gap profile of the comb finger set nearest the center of rotation and the farthest from the center of rotation are shown. The comb finger set nearest to the center of rotation has a smaller operating range than that of furthest set and is able to achieve a smaller overall gap and a larger quadratic force coefficient. This example is shown to point out that under specific operating conditions, the optimization of every comb finger set in the comb drive individually will allow for the comb drive to cause a greater change in system performance than if all of the comb finger sets were given the same uniform dimensions.

5.5 Results and Conclusion

The optimization algorithm presented in Chapter 4 was modified to include the shaped comb drive elements within the design problem. Figure 42 shows a flow chart of the optimization algorithm that was implemented within MATLAB. The sub

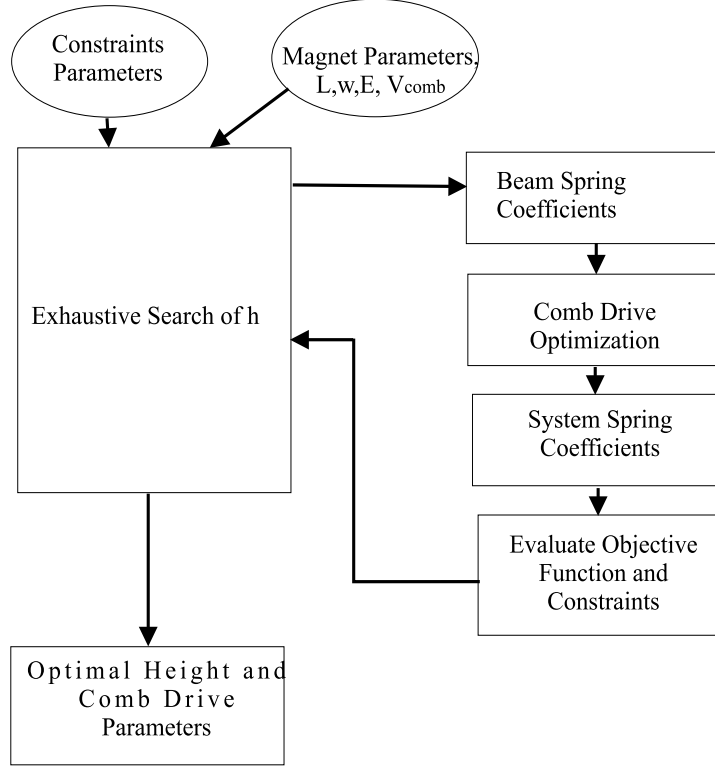


Figure 42: Flowchart of Sensor Optimization.

optimization algorithm shown in Figure 40 is represented as the Comb Drive Optimization block in Figure 42. The comb drive optimization is a sub-problem within the magnetic sensor optimization and therefore inclusion of the shaped comb drive elements into the previous code did not require a change in the methodology of the brute force search previously implemented to determine the optimal system dimensions.

Figure 43(a) shows the objective function for the optimization problem for a system with a voltage of 25 V across the shaped comb drives. The figure has the same shape as the objective function in Chapter 4 and has optimal beam dimensions with a length, width, and height of $2000 \mu m$, $5 \mu m$, and $126 \mu m$ respectively. The same constraint for the z-axis motion of the sensor limits minimum height of the beam geometry as in Chapter 4. The optimal beam height has increased due to the modified stiffness of the magnetic sensor due to the application of the shaped comb drives. The modified stiffness results in an increase in the resonant frequency for the in-plane

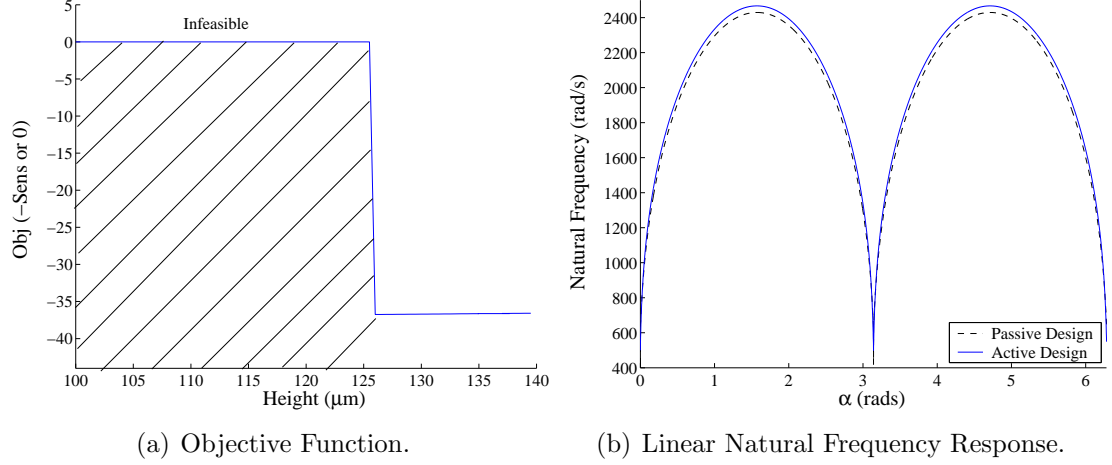


Figure 43: Geometric Optimization with Shaped Comb Drives.

vibration of the sensor and the height of the beams must be increased to maintain an out-of-plane vibration frequency that is 2.5 times higher.

Figure 43(b) shows a comparison of the sensitivity of the optimized magnetic sensor with and without the implementation of shaped comb drives. The voltage applied across the shaped comb drives is 25 V and there are 18 comb fingers within each shaped comb drive. From Table 6.4 it can be seen that the improvement in sensor resolution has increased with the application of shaped comb drives beyond what was achieved through beam optimization. Increasing the voltage across the shaped comb drives should result in further increases in the sensitivity of magnetic sensor due to the shaped comb drives.

Table 10: Comparison of Sensor Resolutions.

<i>Device</i>	Resolution (radians)	Improvement
[28]	.0656	0
Optimized Passive Design	.0538	22%
Optimized Active Design	.0508	29 %

Increases in the voltage applied across the comb drive will result in larger changes in the quadratic stiffness and also decreases in the linear stiffness of the active comb drives, both in a linear fashion. The scalar multiple of the coefficients that can be

used to determine the increase in the shaped comb drive coefficients due to changes in the voltage will change with changes in the voltage such that:

$$Scalar = \frac{V_2^2}{V_1^2} = \frac{(V_1 + \Delta V)^2}{V_1^2} = 1 + \frac{2V_1\Delta V + \Delta V^2}{V_1^2}. \quad (116)$$

In summary, this chapter has shown that the application of shaped comb drives can improve the sensitivity of the magnetic sensor. Through the optimization of the beam dimensions of the sensor and the inclusion of additional stiffness elements to the device, the sensitivity of the sensor to changes in the orientation of the earth's magnetic field has been shown through simulation to increase when compared to the device constructed in [28]. The improvement that can be realized is directly related to the voltage that is applied across the comb drive. Further increases in the voltage applied across the comb drive should result in further improvements in the sensitivity of the magnetic sensor greater than what has been presented here since the shaped comb drives will have provide a larger modification to the quadratic and linear stiffness of the system.

CHAPTER VI

SYSTEM CHARACTERIZATION THROUGH NONLINEAR VIBRATION

This chapter will consider how to improve the sensitivity of the magnetic sensor through the vibration characteristics of the device. Even though the optimization of the magnetic sensor design has been shown to improve sensor performance, the detection scheme used to determine the resonant frequency of the sensor is another component that must be considered when determining its overall sensitivity. While the type of frequency detection scheme was not considered for the development of the mechanical components of the sensor, an analysis of the vibration characteristics of the sensor will give insight on how to design frequency sensing devices and electronics to maximize the sensitivity that can be realized with the magnetic sensor. Several factors must be considered when determining how to effectively measure the frequency of the sensor. They are: the presence of noise within the system, the effect of shock impulses on device performance, and also the effect of damping on the quality factor of the sensor.

In this chapter, it is proposed that increasing the amplitude of the excitation force such that a resonator will exhibit nonlinear vibration behavior and the characterization of the system through its nonlinear vibration behavior will result in improved sensitivities of the resonator. The use of the nonlinear frequency response will be shown to reduce the error in the sensing signal due to noise in the system and also eliminate the effect of damping on the ability of the sensor output to show shifts in the linear natural frequency, which is typically used in MEMS sensors.

6.1 Related Work

Decreasing the size of sensors from the macro- to micro-scale increases the effect of the noise on the quality of the vibration since the magnitude of system noise approaches the same order as the resonant behavior of the device. The effects of temperature changes, molecule absorption, drive power, and self-heating are just a few sources of noise with MEMS devices that can degrade the quality of the resonant signal and the ability of the frequency detection scheme to detect changes in the sensor behavior [48].

A great deal of research has been performed to reduce the degradation of frequency information due to the presence of noise with system. Han focused on changing the proof-mass of the accelerometer to reduce the effect of mechanical noise within the system [23]. Riehl reduced the effect of noise on the resonant frequency signal quality by adding of capacitors to the resonating device in [41]. The addition of signal processing electronics to the electrical sensing of the resonant behavior is another technique that has been presented to reduce the effect of noise on the sensitivity of sensors. By applying noise filters and optimizing the sensitivity of the electrical circuit to match the sensitivity of the mechanical components the authors were able to reduce the noise levels present within the sensor [6]. A disadvantage of the addition of new components to a system in order to reduce the effect of noise on signal quality is in the increased cost of fabrication for devices of increasing complexity.

Other problems that limit the sensitivity of the resonant sensors are related to the mechanics of the resonator, primarily the quality factor, or Q-factor, of the resonator, which is a measure of damping present in the device. It is well known that in order to improve the performance and sensitivity of a device, the damping of the device should be decreased as much as possible. Some sources of damping and energy loss in MEMS devices are air damping, heat loss to the environment, self-heating, and vibration transmission to anchor supports [50].

For most MEMS devices, the primary source of damping is due to energy transmission to the air surrounding the device. The operation of MEMS oscillators under low pressure and vacuum conditions has been shown to greatly increase the sensitivity of the device many magnitudes higher than what can be achieved at ambient pressure [11]. Another technique that has been presented to improve the quality factor of MEMS resonators is the implementation of a feedback control loop within the frequency detection electronics [1]. The chief disadvantage of the controller addition to the sensor is the added complexity in fabrication and the increased power requirement of the device with the addition of the control system.

A passive technique to modify the behavior of the system would be preferred in the magnetic sensor in order to maintain a low power requirement. Therefore, a mechanically-based solution to improve the quality factor would be best. The ideal approach would be to use a resonant sensing technique that would be able to simultaneously deal with system noise and low Q-factor without the need for adding extra components to a system. Both issues can be addressed by changing the type of signal that is being detected by the electronics within the resonator rather the type of system that is being analyzed.

One technique that has been implemented to simultaneously deal with the noise and quality factor issues without modifications to the system itself is to detect the behavior of the higher order harmonics present within the system instead of the fundamental resonant frequency. This approach has been implemented in [32] to determine the resonant frequency and Q-factor in a system with a large amount of parasitic signal losses near the fundamental resonant frequency. While the technique does provide a means of detecting the resonance of a device in a system with a significant amount of noise and very low quality factor near the fundamental resonant frequency, it does not provide a means for greatly improving the quality factor of the device.

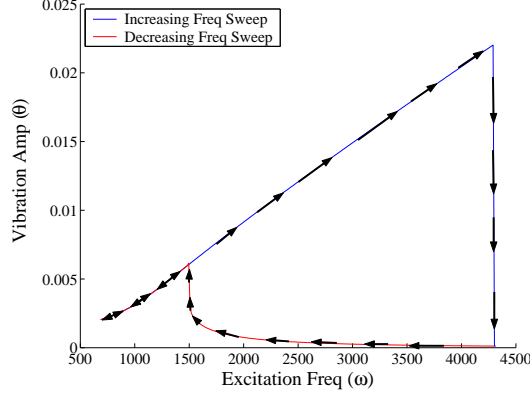


Figure 44: Frequency Sweeping and Correlation to Jump Phenomena.

Another alternative method of detection which has been shown to improve the Q-factor of resonant signal is to increase the amplitude of the harmonic excitation force [32], [24]. By increasing the magnitude of the excitation force, the change in the system response near the linear natural frequency is greatly increased. Further increasing the magnitude of the excitation force will result in nonlinear vibration of the system which will be shown to be more effective at isolating the frequency response information from noise and the effects of Q-factor than with conventional detection of linear vibration frequencies.

6.2 Nonlinear Vibration Analysis

The equation for the magnetic sensor is repeated here for use in the discussion of nonlinear vibration in the following sections. The dynamics equation of the sensor from Chapter 3 is:

$$I \cdot \frac{d^2\theta}{dt^2} + \mu \cdot \frac{d\theta}{dt} + K_L \cdot \theta + K_Q\theta^2 + K_C\theta^3 = T_E(t) + T_{mag}(\alpha, \theta_0, \theta_d), \quad (117)$$

A device undergoing nonlinear vibration will no longer have a single resonant peak as with linear vibration, but will have a different system response due to direction of sweeping the excitation frequency through the region of resonance. The cause for the change in system response is that the initial conditions of the system are coupled

with the forced response of the system to harmonic excitation. For certain frequencies of excitation, the system has two steady-state amplitudes of vibration for which the system will be stable. An increasing frequency sweep through the resonant region of the device will result in a jump-down of the steady-state system response from one stability curve to the next and a large reduction in the amplitude of vibration. A jump-up frequency can be seen in the response during a decreasing sweep through the resonant region of the device that will result in a large increase in the response of the system over a small change in excitation frequency. Figure 44 shows an example of a generic nonlinear system that has been excited into nonlinear vibration and the jump-up and jump-down responses can be seen along with the required direction of the frequency sweep to elicit each type of behavior.

The magnitude of the change in the jump-up frequency of the sensor has shown to track the change in the linear natural frequency of the sensor. Therefore jump-up frequency of the sensor can be used to detect changes in the orientation of external magnetic fields instead of the linear natural frequency to take advantage of the benefits of nonlinear vibration such as noise insensitivity and independence from system damping. Figure 45(a) shows a comparison of the changes in the linear natural frequency to the change in the jump-up frequency for a magnetic sensor with beams of length, width, and height of $2000\ \mu m$, $14\ \mu m$, and $200\ \mu m$ in a magnetic field such that the magnetic torque is $7.96 * 10^{-10}\ N \cdot m$.

It can be seen in Figure 45(a) that changes in both the linear natural frequency and the jump-up frequency are the same for variations in external magnetic field orientation α over the majority of the region from $\alpha = 0$ to $\frac{\pi}{2}$. The change in the jump-down frequency that corresponds to an increasing the excitation frequency to sweep through the dynamic response range of the sensor is also shown in Figure 45(b). The shift in the jump-down frequency due to changes in α are not as significant as the change in the jump-up frequency and this response should not be used to characterize

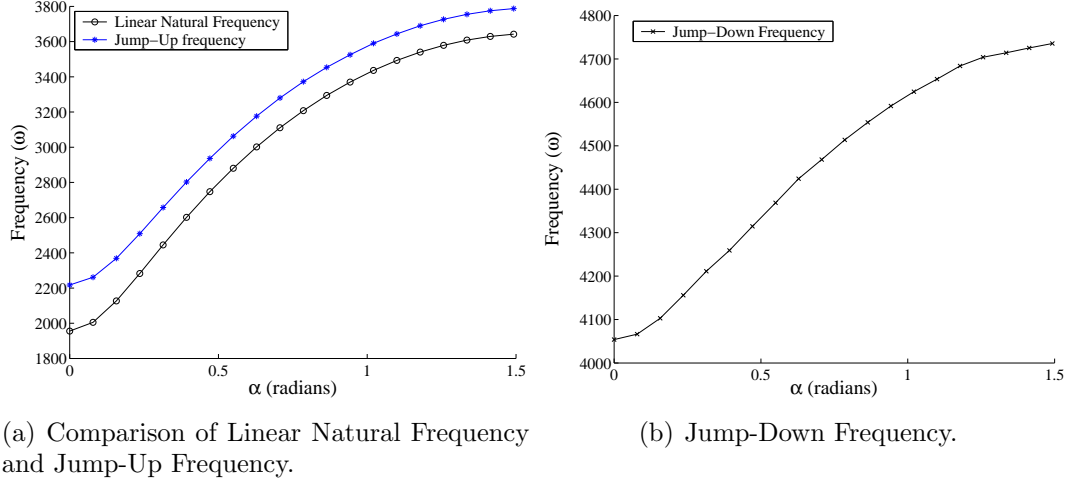


Figure 45: Frequency versus Orientation of External Field.

the system instead of the linear natural frequency.

6.3 Insensitivity to Noise

If the system was instead characterized based upon the linear natural frequency of the device, small amounts of noise will have a greater affect on the ability of the frequency detection scheme to detect the linear natural frequency of the device when the magnitude of the noise present in the system is of the same order as the change in the resonant behavior. In such a device, the sensitivity of the detection scheme would directly affect the overall sensitivity of the sensor since noise in the system would reduce the effective resolution of the sensor. The examples presented here are for a magnetic sensor with beams with lengths of $2000 \mu m$, widths of $7 \mu m$, and height of $100 \mu m$. The nonlinear vibration response to harmonic excitation can be seen in Figure 46(a) and corresponds to magnitude of the excitation torque of $2000 N \cdot m$. Figure 46(b) shows the linear vibration response of the same system with excitation torque of $100 N \cdot m$.

Figures 47(a) and 47(b) show the steady-state response of the system undergoing linear vibration at excitation frequencies 1 and 2 of Figure 46(b). The locations represent the system near resonance at an excitation frequency of $1135 \frac{rad}{s}$ radians

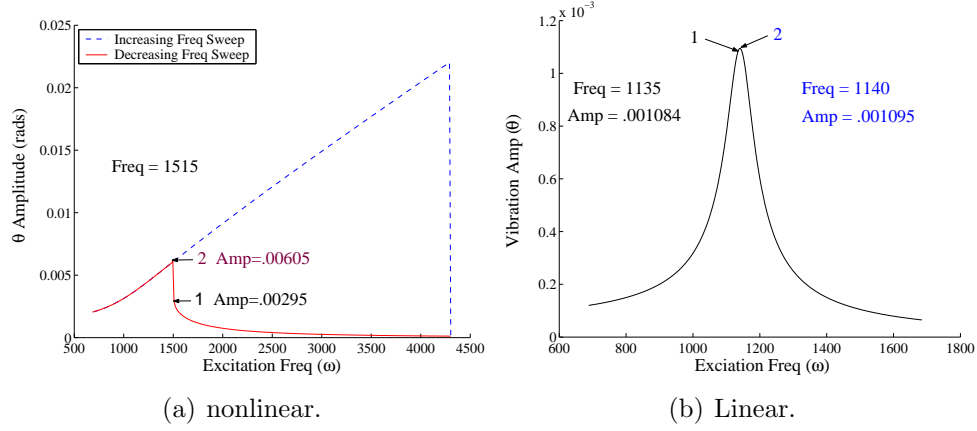


Figure 46: Vibration Response of Example to Parametric Excitation.

and at the linear natural frequency of $1140 \frac{rad}{s}$. The random noise seen in the system is on the order of $\pm 1.5 * 10^{-2}$ and is introduced into response of the system such that:

$$\theta(t) = SS(t) + 1.5 * 10^{-2} \cdot (.5 - random),$$

where SS is the steady state response of the system for the fundamental frequency and the first four harmonics and random is the *rand* function in MATLAB. While the variations in the amplitude of vibration of the system cannot be clearly seen in the system responses, the FFT analysis of the responses in Figures 48(a) and 48(b) shows the presence of the fundamental harmonic in the response.

The boundaries of uncertainty shown in Figures 50(b) and 50(a) were determined by running the simulation for 1000 runs with different random numbers and recording the magnitude for the vibration amplitude at the resonating frequency. The maximum peak that was found by the FFT and was set as the upper limit for the boundary of uncertainty and the minimum peak was set as the lower boundary. The boundary of uncertainties for each of the excitation frequencies overlap, the location of the linear natural frequency cannot be determined with confidence and the amplitude of vibration that is seen at the resonant frequency may be lower than at a nearby excitation frequency.

Based upon the results from the simulation, the use of linear vibration cannot

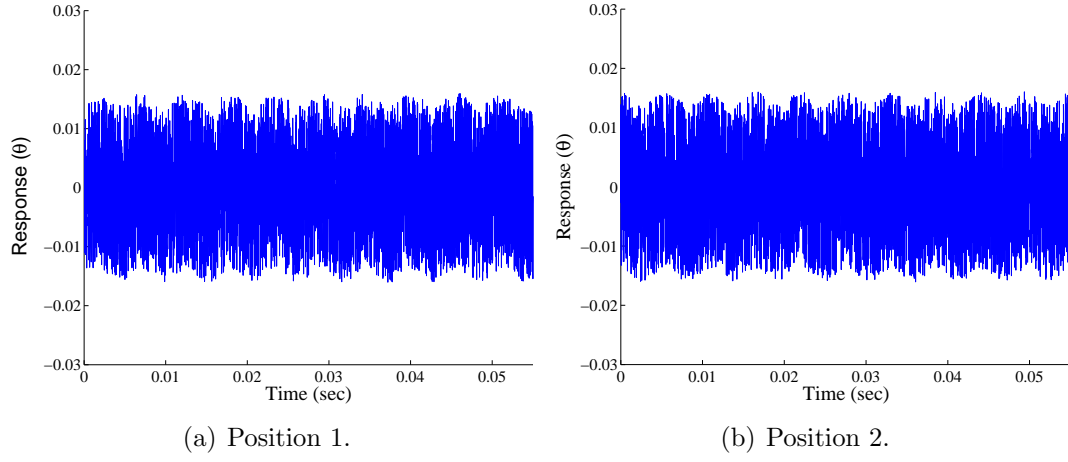


Figure 47: Steady-State Response near Resonance with Noise.

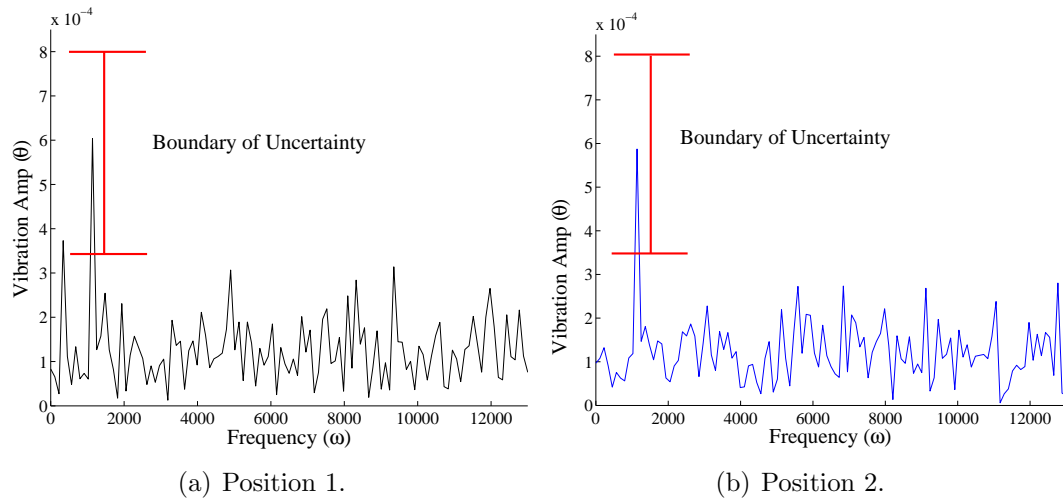


Figure 48: FFT of Linear Vibration near Resonance with Noise.

be used to determine a shift in resonance of the system due to the presence of noise in the system and the resolution that can be realized through the linear vibration characterization is reduced. Even though real world devices are not expected to operate in such noisy environments as the example, there are still regions in the linear vibration of all devices where the change in the linear vibration amplitude will be on the same order as the noise in the system. The ability of the frequency characterization method to detect changes in the harmonic behavior of the resonator would become the limiting factor that would affect the final resolution of a sensor if noise within the vibration signal is greater than the change in the response of the system.

By utilizing the jump-up of frequency in the nonlinear vibration of the sensor to characterize the system behavior instead of the linear natural frequency, improvement in the sensitivity can be realized since the frequency measurement will be insensitive to noise within vibration response of the device. The following example shows that the use of nonlinear vibration to characterize the system will allow for increased resolution over the use of linear vibration to characterize the resonant behavior of devices.

It is important to note that in the region near the jump-up point for the nonlinear vibration of the system, the steady-state vibration of the system varies dramatically as the excitation frequency decreases. Since the nonlinear vibration response is dependent upon the initial conditions of the system, an impulse in the system such as a shock load could cause the vibration response to jump from the lower curve to the upper one. However, a large change in the system conditions substantially greater than typical noise sources is required in order to bump the solution from one stability curve to the other since the system will return to the nearest stability curve in the presence of transient noise. Due to the small change in system behavior typical to noise sources, only changes in the excitation frequency will result in a jump from the

lower stability curve to the upper one.

For points 1 and 2 in Figure 46(a) near the jump-up frequency, the vibration amplitude changes from $2.95 * 10^{-3}$ radians to $6.05 * 10^{-3}$ radians, which is a change of 200% and is significantly larger than the variations of the harmonic amplitudes that can be expected due to typical mechanical noise sources within the sensor. In order for the noise within the system to affect the detection of the jump, it would have to be on the same order as the amplitude of the jump. Figures 49(a) and 49(b) show the steady-state response for the system at each location. The random noise seen in the system is the same the noise in the linear vibration example and is on the order of $\pm 1.5 * 10^{-2}$ and is introduced into response of the system such that:

$$\theta(t) = SS(t) + 1.5 * 10^{-2} \cdot (.5 - random),$$

where SS is the steady state response of the system for the fundamental frequency and the first four harmonics and random is the *rand* function in MATLAB. The insensitivity of the jump frequency to large amounts of noise can be seen in Figures 50(a) and 50(b) which show the FFT of the system as it jumps from position 1 of the lower frequency response curve to position 2 of the upper frequency response curve. Since the boundaries of uncertainty do not overlap, the presence of noise will not affect the ability of the detection scheme to detect changes in the system behavior as it jumps up from position 1 on the lower stability curve position 2 on the upper stability curve.

6.4 Insensitivity to Quality-Factor

The nonlinear vibration characterization technique also removes the dependence of resolution on the damping and energy loss mechanisms within the system. It is well known that energy loss due to damping will reduce the Q-factor of a device and therefore the resolution that can be achieved by the device. Figure 51 shows how variations in the value of μ , which relates to damping, will affect its dynamic response of a linearly vibrating system. From the figure it can be seen that increasing in the

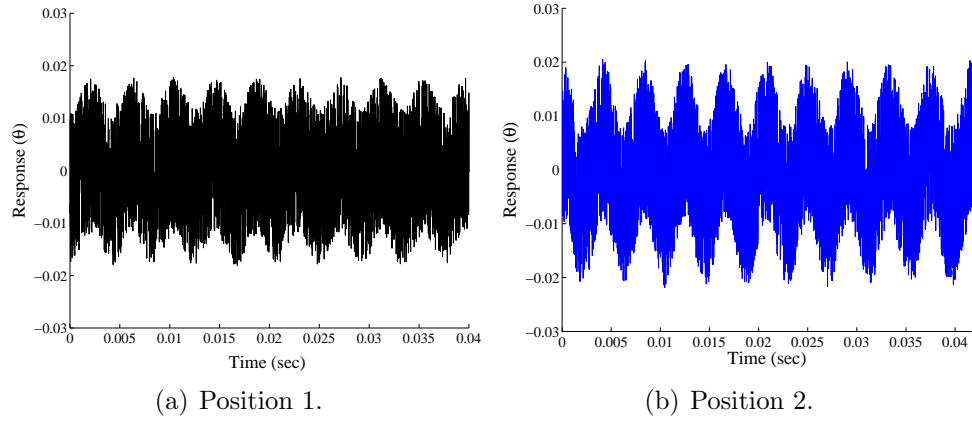


Figure 49: Steady-State Response near the Jump-Up Frequency with Noise.

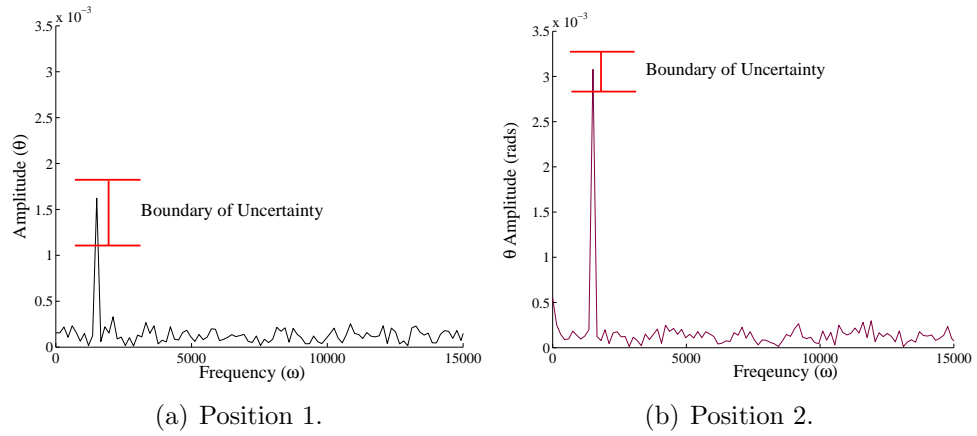


Figure 50: FFT of nonlinear Vibration near the Jump-Up Frequency with Noise.

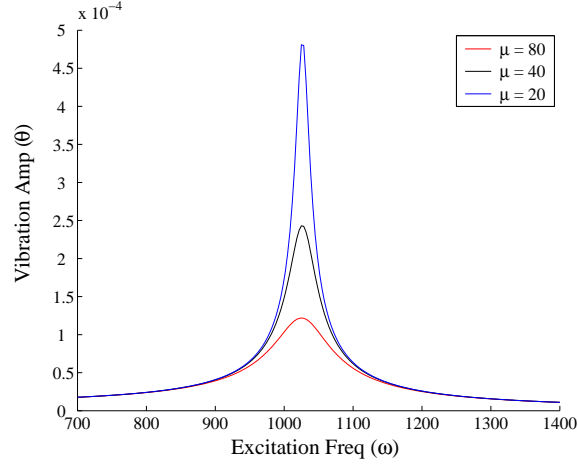


Figure 51: Effect of Damping on Linear Vibration Behavior.

system damping will flatten out the resonant peak. This will result in more excitation frequencies that have a similar dynamic response. With the addition of noise to the vibration signal it will be more difficult to detect the linear natural frequency and the resolution that can be achieved by the sensor will be reduced.

By using the jump-up frequency instead of the linear natural frequency to characterize the sensor, the effects of damping do not have to be considered since the jump-up frequency is independent of the system damping. Since the damping coefficient no longer is an element of the device that must be considered, there is no benefit to adding complexity to a resonator design to package it within a low pressure environment or within a vacuum. An example is given here for systems with variations in damping to show the independence of the jump-up frequency to damping within the device. The value for μ , which represents the system damping, was varied between the three cases to demonstrate its insignificance to the jump-up frequency. The same system used to display insensitivity to noise in the previous section is used as the example of the effect of variations in the damping of the system through changes in the damping value μ from equation (117), which is the dynamic equation for a HelmHoltz-Duffing Oscillator as well as the magnetic sensor.

Table 6.4 shows the jump-up frequency for the three different systems shown in

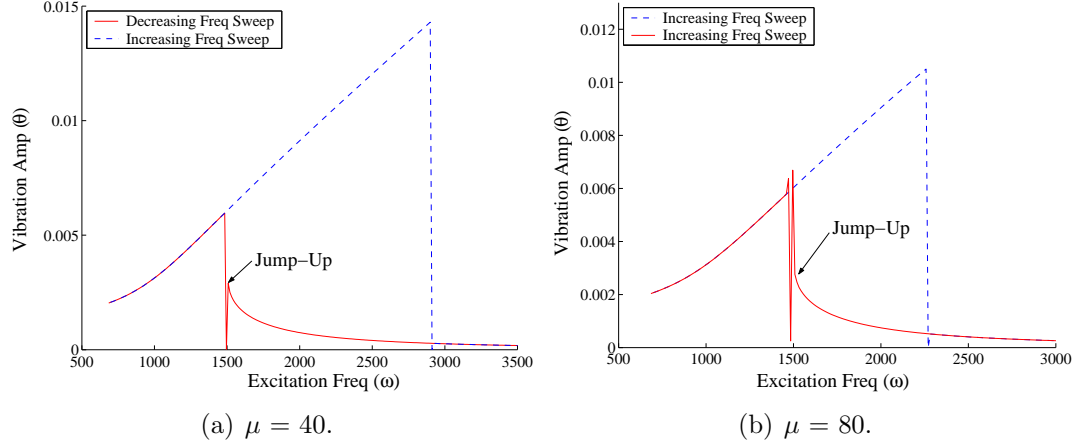


Figure 52: Nonlinear Vibration Response of Example System with Variations in Damping.

Table 11: Comparison of Jump-Up Frequencies.

μ	Jump-Up
20	1507.8
40	1507.8
80	1507.8

Figures 46(a), 52(a), and 52(b) with μ equal to 21, 41, and 81 respectively. It is also seen in the figures that the jump from the lower stability curve to the upper stability curve is over a very short change in excitation frequency. When compared to a measurement of the Q-factor of the system, the jump condition begins to approach the idealized value of infinity due to the nearly instantaneous change in system behavior at the jump-up frequency. Therefore the use of the jump-up frequency to characterize the system results in an effective Q-factor that approaches infinity. The benefits of such a high Q-factor are clear: the system would be less sensitive to noise and the effects of damping within the system without adding complexity to a device.

6.5 Technique Applicability

Nonlinear vibration characterization technique does not require the addition of complex system components in order to improve the quality of the sensor, but instead

only requires increase in the amplitude of vibration for the system. Therefore this technique can be applied in most types of present sensors without altering the mechanics or designs with the addition of extra components such as signal processing circuits or vacuum packaging. The exact implementation of the technique, such as excitation required to drive system to nonlinear vibration, must be determined on a case-by-case basis.

This technique cannot be generically applied to all forms of resonant sensors since there are a variety of ways that the resonance of the system is used to detect changes in the environment. The technique can be applied for use within the magnetic sensor since it is expected that the device will be operated to find an instantaneous orientation of an external magnetic field instead of a continuous measurement. A frequency sweep to find the jump-up frequency could then be implemented and changes in the jump-up frequency can be equated to changes in the orientation of the external magnetic field. Nonlinear vibration characterization requires a frequency sweep of the system to characterize a system and is not applicable to sensors that require continuous frequency knowledge since they do not have time to run a frequency sweep.

A second sensor requirement for nonlinear vibration characterization is that the effect nonlinearity has on system's behavior should be noticeable for reasonable excitation amplitudes. This technique may not be applicable for sensors that are designed such that the linear behavior of the device dominates the effects of nonlinearities on the system response. Such a device would require very large excitation amplitudes in order for the nonlinear system properties to become of the same magnitude as the linear behavior so they will affect the vibration characteristics of the system. It is much more effective to design a system to have sufficient nonlinearities so that this technique will apply as opposed to the application of this technique to a system that has been designed to only operate in regions of linear behavior.

6.6 Conclusions

Nonlinearities are present in many MEMS resonant sensor but have not been utilized to improve the resolution that can be achieved by the sensors. This approach can be applied to a wide variety of sensors without requiring a redesign of the devices, only increases in the amplitudes of the excitation forces used to drive the sensor into resonance. By applying the use of the jump-up frequency to detect shifts in the linear natural frequency of the sensors, the nonlinear behavior that is inherent in many sensors can be exploited to improve the resolution of the sensor.

Noise within a system that uses the conventional linear vibration detection scheme can make it difficult to detect the shifts in the linear natural frequency that is related to changes in the environment. The nonlinear frequency detection technique can be used as a way to improve the resolution of resonant sensors since the location of the jump-up frequency can be detected even when large amounts of noise are present in the system. The application of this technique to sensors in noisy environments should allow the devices to increase their resolution without the need to add complex components to filter the vibration information or isolate the sensor from the noise. It has also been shown that damping within the system does not affect the sensitivity of the nonlinear vibration characterization technique as with conventional methods that characterize systems through their linear vibration. Damping greatly affects the resolution of MEMS resonators that use linear vibration detection and the use of the nonlinear vibration detection scheme will allow for increases in resolution without the need to package the sensors in a vacuum environment. The application of nonlinear vibration detection may lead to increases in sensor resolutions that will speed up the development of MEMS sensors from prototype stages to sensor that can be sold commercially.

CHAPTER VII

CONCLUSIONS AND FUTURE WORK

7.1 Conclusions

Sensors remain an important part of society and are integrated in areas such as manufacturing processes, automobiles, and household appliances to name a few examples. Advances in the sensitivity of sensors and device fabrication should lead to further advances in technological development of society. This thesis has lead to improvements in the modeling of a MEMS resonator for use as a magnetic sensor through a development of an analytical model to represent the nonlinear system components and their effects on the sensitivity of the magnetic sensor. The improved model provides a better understanding of how modifications of sensor parameters will affect the behavior of the device and allows for improved optimization of the magnetic sensor design.

Through the optimization of the sensor to increase the effects of nonlinearities on device behavior, the sensitivity of the magnetic sensor should be increased. The application of shaped comb drives to the magnetic sensor provided a means of increasing the nonlinearity of the sensor by simultaneously reducing the linear behavior of the system stiffness and increasing the quadratic nonlinear behavior of the sensor. The methodology presented within this thesis to exploit nonlinearities of the sensor can be applied to other MEMS devices where the nonlinearities affect the device behavior. By developing nonlinear models of other devices and determining how the nonlinearities relate to the system response, improved performance may be realized by exploiting the nonlinear behavior of the devices.

The final contribution of this thesis is the proposal of a frequency sensing technique to improve the performance of resonant sensors through nonlinear vibration characterization of system behavior. The implementation of nonlinear vibration to detect changes in the sensor behavior is not limited for use with the magnetic sensor and can be applied to other types of MEMS resonators that require the static measurement of the vibration behavior. The use of the jump-up frequency to detect shifts in the linear natural frequency of resonators should result in devices that are insensitive to large amounts of noise and resolutions that are independent of the amount of damping present in the resonating system.

7.2 Future Work

There are several areas of research that worth investigating in order to provide further improvement in the design of the magnetic sensor and to expand the application of nonlinear system behavior to other MEMS devices.

Further research to improve the strength of the magnet used within the sensor should result in increases in the sensitivity of the system over what has been proposed within this thesis. Increasing the magnetic torque will result in larger deflection of the beams during sensor operation and should increase sensitivity of the sensor beyond what can be achieved through the optimization of the mechanical elements of the sensor and the application of shaped comb drives.

Exploration of new types of MEMS fabrication techniques for use in the creating the magnetic sensor could result in improved performance if the minimum gap and minimum feature size of the beam is reduced. Reduction of the minimum gap would allow for the design of more powerful shaped comb drives that would allow for improved performance or also allow for reduction in the voltage required to generate forces. While the optimization of the magnetic sensor was done with the assumption that the device would be fabricated with the facilities located at Georgia Tech, future

work can be done on the optimization of the design for construction utilizing other manufacturing facilities and procedures.

Manufacturing for the shaped comb drives was also not considered for the redesign of the magnetic sensor within this thesis. The fabrication of variable gap comb drives could lead to difficulties in manufacturing that may lead to additional design constraints that must be considered when optimizing the comb finger sets within the shaped comb drives. Additional work in the development of the magnetic sensor should determine the amount of power and the maximum voltage that can be used by the shaped comb drives. While it is expected that the additional consideration of the power requirement of the sensor should lead to an improved optimization of the shaped comb drives and may result in further improvements in the sensor sensitivity.

The final area that could benefit from further research is the implementation of nonlinear vibration characterization to other devices to further validate the advantages of characterizing system behavior with this technique. The use of the jump-frequency to detect changes in system behavior due the environment could result in increased resolutions for pressure sensors, temperature sensors, and magnetic sensors to name a few examples. New frequency detection schemes and devices should be investigated in order to generate designs that are able to take full advantage of the nonlinear vibration of the oscillators without a loss in frequency detection performance. Further research in the design of the excitation elements could lead to increases in the driving force for the system and also reductions in the power required to drive the system into large deflection.

APPENDIX A

BEAM DEFLECTION CODE

The following is a list of Maple commands used to solve for P in Section 3.2.1.2 for use to determine a relationship between P , S , M_0 and δ_y .

```
restart;
y_x:=- (P*x+Mo-P*L)/S+C1*sinh(t*x)+C2*cosh(t*x);
Y_prime:=diff(y_x,x);
BC_xL_slope:=subs({x=L},Y_prime);
BC_x0_slope:=subs({x=0},Y_prime);
BC_x0_slope:=eval(BC_x0_slope);
Rot:=(delta)/(R^2-(delta)^2)^.5;
BC_x0_slope:=eval(BC_x0_slope)-Rot;
BC_xL:=- (P*L+Mo-P*L)/S+C1*sinh(t*L)+C2*cosh(t*L);
solve({BC_x0_slope,BC_xL,BC_xL_slope},{C1,C2,Mo});
```

The solutions for $C1$, $C2$, and Mo must then be stored as variables in the workspace.

The example for $C1$ is shown

```
C1:= (expression);
Y:=- (P*x+Mo-P*L)/S+C1*sinh(t*x)+C2*cosh(t*x);
Ymax_x0:=subs({x=0},Y);
Ymax_x0:=eval(Ymax_x0);
```

The following command solves for P as a function of R , δ , and S .

```
solve({Ymax_x0-delta},P);
```

```

Dy_Dx:=diff(Y,x);
Dy_Dx_2:=(Dy_Dx)^2;
int_dy_dx:=int(Dy_Dx_2,x=0..L);
S_:=A*E/(2*L)*int_dy_dx+(R1-sqrt(R1^2-delta^2))*A*E/L;
S_:=solve({S_-S},P);

```

By defining P in the workspace similar to how $C1$ was defined, it is possible to display a form of P that can be copied directly into MATLAB or other math computation codes.

APPENDIX B

EXAMPLE DEVICE DIMENSIONS

B.1 Resonator without Magnet

Figure (53) shows a drawing of the resonator used in Section 3.5.2 to compare the analytical model of the MEMS resonator with an experimental device. The device is similar to the magnetic sensor considered in this thesis, but without the magnet. The primary dimensions of the resonator are:

Table 12: Significant Device Dimenions

<i>Dimension</i>	Value
Beam Length	2000 μm
width	14 μm
height	200 μm
Disk Radius	1000 μm
Comb Drive Radius	2400 μm
ρ silicon	2.33 $\frac{g}{cc}$
E	131 GPa

B.2 Resonator with Magnet

The dimensions of the device used in Section 3.5.3 to analyze the behavior of the magnetic sensor are:

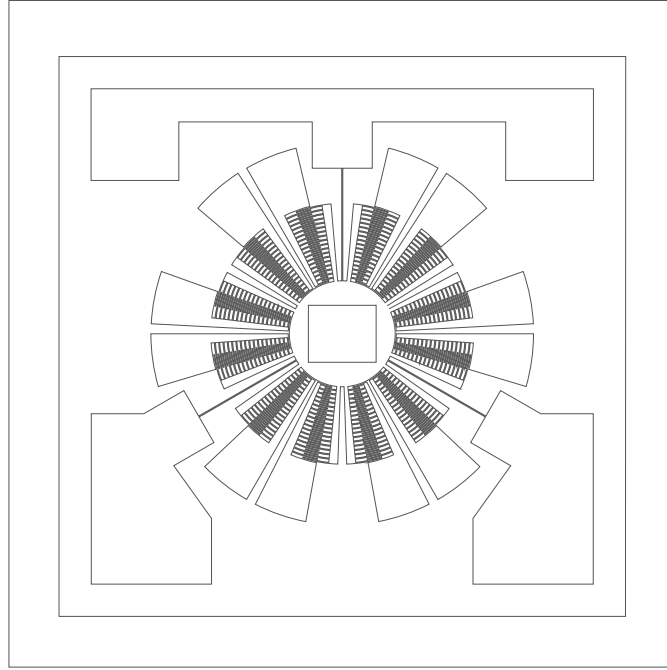


Figure 53: Autocad Drawing of Magnetic Sensor.

Table 13: Significant Device Dimenions

<i>Dimension</i>	Value
Beam Length	2000 μm
width	16 μm
height	200 μm
Disk Radius	1000 μm
Comb Drive Radius	2400 μm
ρ silicon	2.33 $\frac{g}{cc}$

APPENDIX C

OPTIMAL SHAPED COMB DRIVE PARAMETERS

Table C presents the comb finger parameters for the optimal shaped comb drive presented in Chapter 5. The equation used to translate the system parameters into the shape of the comb drive gap is:

$$gap = \frac{1}{c0 + c1 \cdot x + c2 \cdot x^2 + c3 \cdot x^3} \mu m$$

where x represents the insertion depth of the moving finger. Both values for x and the gap are in microns.

Table 14: Gap Parameters for an Optimized Shaped Comb Drive.

Radius (μm)	c0	c1	c2
1065	0.05	-0.00707	0.001904
1115	0.05	-0.00694	0.001840
1165	0.05	-0.00682	0.001779
1215	0.05	-0.00670	0.001721
1265	0.05	-0.00659	0.001666
1315	0.05	-0.00648	0.001614
1365	0.05	-0.00639	0.001564
1416	0.05	-0.00629	0.001517
1465	0.05	-0.00620	0.001472
1515	0.05	-0.00611	0.001428
1565	0.05	-0.00603	0.001387
1615	0.05	-0.00596	0.001348
1665	0.05	-0.005898	0.001310
1715	0.05	-0.00579	0.001273
1765	0.05	-0.00570	0.001238
1815	0.05	-0.00562	0.001204
1865	0.05	-0.00553	0.001172
1915	0.05	-0.00546	0.001141
1965	0.05	-0.00539	0.001111
2015	0.05	-0.00531	0.001082

APPENDIX D

MAGNETIC SENSOR OPTIMIZATION CODE WITH SHAPED COMB DRIVE

The following code was implemented in MATLAB to determine the height for the magnetic sensor beams and the corresponding optimal gap profiles for the shaped comb drives. The results from the code were discussed in Chapter 5.

Main Program Code:

```
clear all

global cd0 cd1 cd2 cd3 V e h pos1 pos2 ming maxg ming2

% Variables used to evaluate sensitivity

resWN=1;

resAlpha1=pi/2-.1;

resAlpha2=pi/2;

% Variables are the dimensions of the beam system

DensM=7440; %kg/m^3 Density of permanent magnet

Rm=800*10^-6; %m permanent magnet radius

Tm=800*10^-6; %m permanent magnet thickness

Vm=pi*Rm^2*Tm; % Volution of permanent magnet

R2=2000*10^-6; % External radius of comb drive supports

T=7.2*10^-8; % Magnitude of magnetic torque

comb=0;

R1=1000*10^-6; %Radius of central disk

rho=2330; %density of silicon
```



```

E=131e9; % elastic modulus of silicon
V=25; % Voltage across shaped comb drive
e=8.85*10^-12; % Permittivity of free space
L=2000e-6; % beam length
w=5e-6; % beam width

% for the purpose of this code, height and thickness are equivalent.
% h and t are also related to the height/thickness of the sensor
% beams

for hh=1:131
    t=(.1*(hh-1)+45)*10^-6;
    height(hh)=t
    iteration = 0;
    FL=0; % Initial shaped comb drive force profile
    FQ=0; % Initial shaped comb drive force profile
    FC=0; % Initial shaped comb drive force profile
    Fprev=120;
    OPTIONS=OPTIMSET('Display','off','LargeScale','off');
    while (abs(FC-Fprev)> 1e-3)
        Fprev=FC;
        iteration = iteration +1;
        % input comb drive parameters
        Arm= 40e-6;% Distance from central disk to first moving comb
            % finger center
        gap0=20; % gap at X=0

```

```

Center= (2*gap0+2*5)*10^-6; % Distance between centers of
                                % the comb drives

% This section calculates the equivalent moment arms for the
% Torque
Rlinear=0;
Rquad=0;
Rcub=0;
i=0;
n=0;
r=0;
rmax=2000e-6;
while (r < rmax)
    i=i+1;
    r=Radius + Arm + .5*Center + (i-1)*Center;
    RR(i)=r;
    n=n+1;
end
n=n; % Number of comb drive sets allowed in the comb drive.
    % the value for n should be 18.

% Initial guesses for optimal gap profiles
cd0 = 1/gap0;
cd1 = -.1;
cd2 = 10;
cd3 = 0;

```

```

% Determine stiffness coefficients due to the sensor beams
Coeff = beamcoeffind(L,t,w,E,R1);

% Deterimine the operating range of each comb drive
error = 1; % The tolerance of the computation in microns. Used
% as a safety factor for unpredictable device motion to prevent
% the gap from becoming less than 2 micron
Insertion = frequency(Rm,Tm,Vm,DensM,E,R1,R2,rho,t,w,L,T,n, ...
RR,Coeff,FL,FQ,FC) + error;

% Set values for gap profile constraints
maxg = gap0+3;
if (ceil(t/15) > 2)
    ming=ceil(t/15);
else
    ming=3;
end
pos1 = 10;
ming2 = 2;

% Determine the Maximum coefficients for each comb drive set
for kk=1:n
    pos2 = Insertion(kk)+pos1; % end of operating range
    pos22(kk)=pos2; % begin of operating range
    x0 = [cd0,cd1,cd2,cd3]; % initial guess.
    % but the program should figure it out
    Lbnd = [0.05 -2 0 0];
    Ubnd = [cd0 0 inf 0];
end

```

```

[x,f]=fmincon('GapF',x0,[],[],[],[],Lbnd ...
,Ubnd,'GapCon',OPTIONS);
c0(kk)=x(1);
c1(kk)=x(2);
c2(kk)=x(3);
c3(kk)=x(4);

end

% Convert from microns to meters
C0=c0*10^6;
C1=c1*10^12;
C2=c2*10^18;
C3=c3*10^24;

% Sum all of the contributions of each comb finger
% torque together.
T0=0;
TL=0;
TQ=0;
TC=0;
for j=1:n
    T0=C0(j)*RR(j)*t*e*V^2+T0;
    TL=e*t*V^2*C1(j)*RR(j)^2+TL;
    TQ=e*t*V^2*C2(j)*RR(j)^3+TQ;
    TC=e*t*V^2*C3(j)*(RR(j))^4+TC;
end

% Calculate equivalent lateral stiffness to be added to terms
% from the beam lateral stiffness
FL=TL/R1^2;

```

```

    FQ=TQ/R1^3;
    FC=TC/R1^4;
    Diff=FQ-Fprev;
end

% Evaluate new system stiffness coefficients
Ca=Coeff(1)+FL;
Cb=Coeff(2)+FQ;
Cc=Coeff(3)+FC;
Ma=Coeff(4);
Mb=Coeff(5);
Mc=Coeff(6);
Cax=Coeff(7);
Cbx=Coeff(8);
Ccx=Coeff(9);
I=1/12*t*w^3;
Inertia=(1/2*rho*t*pi*R1^4+rhom*pi*Rm^2*Tm*(1/12*(3*Rm^2+Tm^2)) ...
+(1/10*rho*t*pi*(R2^4-R1^4)));
Icomb=0;
% Eval inertia of comb fingers
for j=1:18
    Icomb=8/15*rho*t*pi*((R1+40e-6+(40e-6)*(j-1))^4 - ...
    (R1+20e-6+40e-6*(j-1))^4);
end
Inertia=Inertia+Icomb;
% Check system constraints
C=systemCon(t,E,L,w,Coeff,R1 ,T, R2, Vm, DensM, rho, Rm ,Tm);
if ((C(1)*C(2)) >0)

```

```

options=optimset('tolx',eps/4);

% eval natural frequency at position 1

% Eval theta0max

theta=abs(fzero('nonlinearTT_x_M',resAlpha1/2,options,resAlpha1, ...
Ca,Cb,Cc,Cax,Cbx,Ccx,Ma,Mb,Mc,R1,T));

K10=3*Ma*R1+3*Ca*R1^2;

K11=6*(Cax*R1^2+Mb*R1^2+Cb*R1^3+ 1/6*T*sin( resAlpha1));

K12=9*(Ccx*R1^4-1/36*Ma*R1+Cb*R1^3-7/18*Ca*R1^2+Mc*R1^3 ...
+Cc*R1^4-1/108*T*cos( resAlpha1));

K13=(-1.5*Mb*R1^2-5*Cb*R1^3-1.5*Cax*R1^2-1/6*T*sin( resAlpha1));

WnI1=sqrt((T*cos( resAlpha1)+K10 +K11*theta + K12*theta^2 ...
+K13*theta^3)/Inertia);

% eval natural frequency at position 2

% Eval theta0max

theta=abs(fzero('nonlinearTT_x_M',resAlpha2/2,options, ...
resAlpha2,Ca,Cb,Cc,Cax,Cbx,Ccx,Ma,Mb,Mc,R1,T));

K10=3*Ma*R1+3*Ca*R1^2;

K11=6*(Cax*R1^2+Mb*R1^2+Cb*R1^3+ 1/6*T*sin( resAlpha2));

K12=9*(Ccx*R1^4-1/36*Ma*R1+Cb*R1^3-7/18*Ca*R1^2+Mc*R1^3 ...
+Cc*R1^4-1/108*T*cos( resAlpha2));

K13=(-1.5*Mb*R1^2-5*Cb*R1^3-1.5*Cax*R1^2-1/6*T*sin( resAlpha2));

WnI2=sqrt((T*cos( resAlpha2)+K10 +K11*theta + K12*theta^2 ...
+K13*theta^3)/Inertia);

% This section makes sure that resolution is met

Fdes=resWN/(resAlpha2-resAlpha1);

Ftemp=( WnI2- WnI1)/(resAlpha2-resAlpha1);

```

```

        'pass'
        obj(hh)=-Ftemp
        step=hh
    else
        'fail'
        obj(hh)=0
    end
end
end
figure(2);hold on;
plot(height,obj)

```

frequency.m

```

function Insertion = frequency(Rm,Tm,Vm,DensM,E,R1,R2,rho,t,w, ...
L,T,n,RR,Coeff,FL,FQ,FC)
% Convert Coeff to beam stiffness coefficients
T=T;
Ca=Coeff(1)+FL;
Cb=Coeff(2)+FQ;
Cc=Coeff(3)+FC;
Ma=Coeff(4);
Mb=Coeff(5);
Mc=Coeff(6);
Cax=Coeff(7);
Cbx=Coeff(8);
Ccx=Coeff(9);
Inertia=(1/2*rho*t*pi*R1^4+rhom*pi*Rm^2*Tm*(1/12*(3*Rm^2+Tm^2))+

```

```

(1/10*rho*t*pi*(R2^4-R1^4)));
Icomb=0;
% Eval inertia of comb fingers
for j=1:18
    Icomb=8/15*rho*t*pi*((R1+40e-6+(40e-6)*(j-1))^4 - ...
    (R1+20e-6+40e-6*(j-1))^4);
end
Inertia=Inertia+Icomb;

% Determine maximum theta0 that will be experienced by the system.
% this occurs at alpha = pi/2.
alpha=pi/2;
options=optimset('tolx',eps/4);
Thetamax=fzero('nonlinearTT_x_M',alpha/2,options,alpha,Ca,Cb, ...
Cc,Cax,Cbx,Ccx,Ma,Mb,Mc,R1,T);

% Determine the insertion distance for each of the comb drives in
% microns. RR is in meters so it must be converted to microns.
for i=1:n
    Insertion(i)=Thetamax*RR(i)*10^6;
end

```

System Constraints:

```

function C= systemCon(t,E,L,w,XX,R1 ,T, R2, Vm, DensM, rho, Rm ,Tm)
% This function contains the constraint equations for the system
Ca=XX(1);
Cb=XX(2);

```



```

Cc=XX(3);
Ma=XX(4);
Mb=XX(5);
Mc=XX(6);
Cax=XX(7);
Cbx=XX(8);
Ccx=XX(9);
MLL=XX(10);
MLQ=XX(11);
MLC=XX(12);
alpha = pi/2;
options=optimset('tolx',eps/4);
Thetamax =fzero('nonlinearTT_x_M',alpha/100,options,alpha,Ca,Cb, ...
Cc,Cax,Cbx,Ccx,Ma,Mb,Mc,R1,T);

A=t*w;

Masscomb=0;
% Eval weight of comb fingers
for j=1:18
    % Rout=(R1+80e-6+(80e-6)*(j-1))*1000
    % Rin=(R1+60e-6+80e-6*(j-1))*1000
    Masscomb=8/15*rho*t*pi*((R1+40e-6+(40e-6)*(j-1))^2 - ...
(R1+20e-6+40e-6*(j-1))^2);
end
% Eval weight of central region
MassC=DensM*Vm+R1^2*pi*t*rho + 1/10*rho*pi*t*((2430e-6)^2-(R1)^2) ...

```

```

+Masscomb;

% Axial stress at Tip
S=Cax*Thetamax*R1+Cbx*(Thetamax*R1)^2;
Kax=S/A;

% Shear stress at the Tip
Fy = Ca*Thetamax*R1+Cb*(Thetamax*R1)^2+Cc*(Thetamax*R1)^3;
Kshear=sqrt(Fy^2+(Masscomb*9.81)^2)/A;

%Moment at tip
Mz=MLL*(Thetamax*R1)+MLQ*(Thetamax*R1)^2+MLC*(Thetamax*R1)^3;

% Moment to support the magnet and disk in the center
My=(1/3)*(MassC*9.81)*L+L/2*rho*9.81*L*t*w;
tanB=(My*w^2)/(Mz*t^2);
B=atan(tanB);

j=0;
z1=0;
L1=((w/2+z1*tanB)^2+(t/2-z1)^2)^.5;
A=t/2;
z3=z1+A;
L3=((w/2+z3*tanB)^2+(t/2-z3)^2)^.5;
psi=1*10^-12;
a=1;
while a>psi
    j=j+1;
    % bisection variable to keep decreasing distance between
    % max and min points along search direction
    a=A/(2^j);

```

```

    if L1<L3
        z1=z1+a;
        L1=((w/2+z1*tanB)^2+(t/2-z1)^2)^.5;
    else
        z3=z3-a;
        L3=((w/2+z3*tanB)^2+(t/2-z3)^2)^.5;
    end
end

z=t/2-z1;;
y=w/2+z1*tanB;
Kz=My*(z)/(1/12*w*t^3);
Ky=Mz*y/(1/12*w*t^3);
sigmax=abs(Ky+Kz+Kax);
Stress=sqrt((2*sigmax^2+6*Kshear^2)/2);
% Eval Stress Constraint
StressMax=349e6;
C(1)=(Stress-StressMax)/StressMax;

% Evaluate the linear natural frequency of the torsional mode of
% vibration
Inertia=1/2*rho*t*pi*R1^4+DensM*pi*Rm^2*Tm*(1/12*(3*Rm^2+Tm^2)) ...
+1/10*rho*t*pi*(R2^4-R1^4);
Icomb=0;
% Eval weight of comb fingers
for j=1:18
    % Rout=(R1+80e-6+(80e-6)*(j-1))*1000
    % Rin=(R1+60e-6+80e-6*(j-1))*1000

```

```

Icomb=8/15*rho*t*pi*((R1+40e-6+(40e-6)*(j-1))^4 - ...
(R1+20e-6+40e-6*(j-1))^4);
end
Inertia=Inertia+Icomb
K10=3*Ma*R1+3*Ca*R1^2;
K11=6*(Cax*R1^2+Mb*R1^2+Cb*R1^3+ 1/6*T*sin( pi/2));
K12=9*(Ccx*R1^4-1/36*Ma*R1+Cb*R1^3-7/18*Ca*R1^2+Mc*R1^3 ...
+Cc*R1^4-1/108*T*cos(pi/2));
K13=(-1.5*Mb*R1^2-5*Cb*R1^3-1.5*Cax*R1^2-1/6*T*sin( pi/2));
Wn=sqrt((T*cos(pi/2) + K10 + K11*Thetamax + K12*Thetamax^2 ...
+ K13*Thetamax^3)/Inertia)

% Eval natural frequency of vibration for the
zCa=(E*(w*t^3))/L^3;
Wz = sqrt(3*zCa/MassC)
Wmax=2.5;
C(2) = (Wmax - Wz/Wn)/Wmax
C=C

```

Objective Function for Shaped Comb Drives

```

function f= GapF(x)
% this function contains the objective function to be optimized
global cd0 cd1 cd2 cd3
c0=x(1);
c1=x(2);
c2=x(3);
c3=x(4);
f = (cd1-c1)^2 + (cd2-c2)^2;

```

Shaped Comb Drive Constraints

```
function [C,Ceq]= GapCon(x)

% This function contains the constraint equations for the system
c0=x(1);
c1=x(2);
c2=x(3);
c3=x(4);

global pos1 pos2 ming maxg ming2
% minimum gap at a specified location
C(1) = c0 + c1*pos1 + c2*pos1^2 + c3*pos1^3 - 1/ming;
C(2)= -x(1);
% C(3)= -x(2);
C(4)= -x(3);
C(5)= -x(4);
C(6)= c0 + c1*pos2 + c2*pos2^2 + c3*pos2^3 - 1/ming2;
for i=1:maxg
    C(i+6) = 1/maxg - (c0 + c1*(i/2) + c2*(i/2)^2 + c3*(i/2)^3);
end
C;

% gap must be greater than zero
Ceq=[];
```

APPENDIX E

INCREMENTAL HARMONIC BALANCE CODE

The following code was used within MATLAB to determine the response of a nonlinearly vibrating system using the incremental harmonic balance method. The coefficients

$K3_bar$, $K2_bar$, $K1_bar$, C_bar , and F_bar

are found in the differential equation used to describe the system.

```
% Generate equation for IHB
syms a0 a1 a2 a3 a4 a5 b1 b2 b3 b4 b5 tau w0 K3_bar K2_bar ...
K1_bar C_bar F_bar
% The general form of the equation is
%  $M\_bar \ddot{x} + C\_bar \dot{x} + k1\_bar x + k2\_bar x^2 + k3\_bar x^3 = \dots$ 
%  $F\_bar \cos(\Omega t)$ 
M_bar=1;
Cs=[cos(0) cos(tau) cos(2*tau) cos(3*tau) cos(4*tau) cos(5*tau) ...
sin(tau) sin(2*tau) sin(3*tau) sin(4*tau) sin(5*tau)];
A=[a0;a1;a2;a3;a4;a5;b1;b2;b3;b4;b5];
S=[Cs];
Sd=diff(S,tau);
Sdd=diff(Sd,tau);
St=[[ 1]
[ cos((tau))]
```

```

[ cos(2*(tau))]
[ cos(3*(tau))]
[ cos(4*(tau))]
[cos(5*(tau))]
[ sin((tau))]
[ sin(2*(tau))]
[ sin(3*(tau))]
[ sin(4*(tau))]
[sin(5*(tau))]];

Q=S*A;

K2_bar=K2_bar*Q;

K3_bar=K3_bar*Q*Q;

M=int(St*M_bar*Sdd,tau,0+pi/2,2*pi+pi/2);

C=int(St*C_bar*Sd,tau,0+pi/2,2*pi+pi/2);

K=int(St*K1_bar*S,tau,0+pi/2,2*pi+pi/2);

K2=int(St*K2_bar*S,tau,0+pi/2,2*pi+pi/2);

K3=int(St*K3_bar*S,tau,0+pi/2,2*pi+pi/2);

F=int(St*F_bar*cos(tau),tau,0+pi/2,2*pi+pi/2);

Rf=int(St*cos(tau),tau,0+pi/2,2*pi+pi/2);

Kmc=w0^2*M+w0*C+K+2*K2+3*K3;

R=F-(w0^2*M+w0*C+K+K2+K3)*A;


pts=300

adjust=0;

a1=0;

for i=1:pts

    if (a1 < 1e-6)

```

```

        a1=1e-3;a0=0;a2=0;a3=0;a4=0;a5=0;
        b1=0;b2=0;b3=0;b4=0;b5=0;
    else
        a1=a1;
    end
    w0=1000/pts*(i)+685

    IHBwU(i)=w0;
    % Implement iteration loop
    cont=1;
    while(cont == 1)
        Rh=eval(R);
        Kmch=eval(Kmc);
        Delta=Kmch-1*Rh;
        Delta(2);
        cont=lt(1e-4,abs(Delta(2)));
        a0=a0+Delta(1);
        a1=a1 +Delta(2) ;
        a2=a2+Delta(3);
        a3=a3+Delta(4);
        a4=a4+Delta(5);
        a5=a5+Delta(6);
        b1=b1+Delta(7);
        b2=b2+Delta(8);
        b3=b3+Delta(9);
        b4=b4+Delta(10);
        b5=b5+Delta(11);
    end
end

```



```

        sqrt(a1^2+b1^2);
    end
    A0(i)=a0;
    A1U(i)=sqrt(a1^2+b1^2);
    A2U(i)=a2;
    A3U(i)=a3;
    A5U(i)=a5;
    B2U(i)=b2;
    B3U(i)=b3;
    B4U(i)=b4;
    B5U(i)=b5;
    RRR(:,i)=Rh;
end

```

REFERENCES

- [1] G. Abadal, Z.J Davis, B. Helbo, and et al. Electromechanical model of a resonating nano-cantilever-based sensor for high-resolution and high-sensitivity mass detection. In *Nanotechnology*, volume 12, pages 100–104, Toledo, Spain, 2001.
- [2] D.E. Adams. Nonlinear design-for-control: Deploying nonlinearity for useful purposes. In *Proceedings of the ASME Design Engineering Technical Conference*, volume 6c, pages 2871–2877, Pittsburgh, PA, Sept. 2001.
- [3] S.G. Adams, F.M. Bertsch, K.A. Shaw, and N.C. MacDonald. Independent tuning of linear and nonlinear stiffness coefficients. *Journal of Microelectromechanical Systems*, 7(2):172–180, 2003.
- [4] A.D. Belegundu and T.R. Chandrupatla. *Optimization Concepts and Applications in Engineering*. Pearson Education, 1999.
- [5] V. Beroulle, Y. Bertrand, L. Latorre, and P. Nouet. Micromachined cmos magnetic field sensor with low-noise signal conditioning. In *15th IEEE International Conference on Micro Electro Mechanical Systems*, pages 256–259. IEEE, 2002.
- [6] V. Beroulle, Y. Bertrand, L. Latorre, and P. Nouet. Noise optimization of a piezoresistive cmos mems for magnetic field sensing. In *Eleventh International Conference on Very Large Scale Integration of Systems-on-Chip*, pages 461–472, Montpellier, France, 2002.
- [7] K.E. Bisshopp. Approximations for large deflection of a cantilever beam. *Quarterly of Applied Mathematics*, 30(4):521–526, 1973.
- [8] T. Bourouina, A. Garnier, H. Fujita, T. Hiramoto, E. Orsier, and J.-C. Peuzin. Mechanical characterization of magnetostrictively actuated micro-resonators. In *Proceedings of the SPIE*, volume 3893 of *Design, Characterization, and Packaging for MEMS and Microelectronics*, pages 411–420, Gold Coast, Australia, 1999. SPIE.
- [9] O. Brand, M. Hornung, D. Lange, and H. Baltes. Cmos resonant sensors. In *Proceedings of the SPIE*, volume 3514, pages 238–250, Santa Clara, Ca, Sept. 1998. The International Society for Optical Engineering.
- [10] W. Brenner, Gh. Haddad, H. Rennhofer, M. Rennhofer, A. Vujanic, and G. Popovic. New types of silicon torsion microspring and their characterization. In *Proceedings of SPIE*, volume 4019, pages 462–470, Paris, France, May 2000. International Society for Optical Engineering.

- [11] D. Chen, D. Cui, Z. Yu, L. Wang, Z. Cui, and S. Xia. Thermally-excited sin beam resonant pressure sensor. In *Proceedings of SPIE*, volume 4408, pages 548–554, Cannes, France, 2001.
- [12] Y.K. Cheung, S.H. Chen, and S.L. Lau. Application of the incremental harmonic balance method to cubic non-linearity systems. *Journal of Sound and Vibration*, 140(2):273–286, 1990.
- [13] Comb drive actuators, March 2004.
- [14] Z. Cui, D. Chen, and S. Xia. Modelling and experiment of silicon resonant pressure sensor. In *Analog Integrated Circuits and Signal Processing*, volume 32, pages 29–35, Cannes, France, 2002.
- [15] M.J. Daneman, N.C. Tien, O. Solgaard, A.P. Pisano, K.Y. Lau, and R.S. Muller. Linear microvibromotor for positioning optical components. *Journal of Microelectromechanical Systems*, 5(3):159–165, Sept. 1996.
- [16] A.A. Ferri. On the equivalence of the incremental harmonic balance method and the harmonic balance - newton raphson method. *Journal of Applied Mechanics*, 1986.
- [17] C.A.J. Fletcher. *Computational Galerkin Methods*. Springer - Verlag, 1984.
- [18] R. FrischFay. *Flexible Bars*, chapter 3, pages 83–89. Butterworth & Co, 1962.
- [19] A. Garnier, T. Bourouina, I. Fujita, T. Hiramoto, E. Orsier, and J.-C. Peuzin. Magnetic actuation of bending and torsional vibrations for 2d optical-scanner application. *Sensors and Actuators, A:Physical*, A84(1-2):156–160, Aug. 2000.
- [20] J.M. Gere. *Mechanics of Materials*. Brooks/Cole Thompson Learning, 2001.
- [21] J.H. Ginsberg. *Advanced Engineering Dynamics, 2nd Ed.* Cambridge University Press, 1998.
- [22] S. Greek, F. Ericson, S. Johansson, and J.-A. Schweitz. In situ tensile strength measurement and weibull analysis of thick and thin film micromachined polysilicon structures. *Thin Solid Films*, 292(1-2):247–254, 1997.
- [23] K.-H. Han and Y.-H. Cho. Self-balanced high-resolution capacitive microaccelerometers using branched finger electrodes with high-amplitude sense voltage. In *Fifteenth IEEE International Conference on Micro Electro Mechanical Systems*, pages 714–717, Las Vegas, NV, Jan. 2002. IEEE.
- [24] J.A. Harley, E.M. Chow, and T.W. Kenny. Design of resonant beam transducers: An axial force probe for atomic force microscopy. In *Micro-Electro-Mechanical Systems: ASME Intl. ME Congress and Exposition*, pages 247–252, Anaheim, Ca, 1998. ASME.

- [25] B.D. Jensen, S. Mutlu, S. Miller, K. Kurabayashi, and J.J. Allen. Shaped comb fingers for tailored electromechanical restoring force. *Journal of Microelectromechanical Systems*, 12, June 2003.
- [26] J.D. Kraus. *Electromagnetics*. McGraw-Hill, 1984.
- [27] T.G. Leblois and C.R. Tellier. Some investigations on doubly-rotated quartz resonant temperature sensors. *Sensors and Actuators, A: Physical*, 99(3):256–269, June 2002.
- [28] T.C. Leïchl  , M. von Arx, S. Reiman, I. Zana, W. Ye, and M.G. Allen. A low-power resonant micromachined compass. *in Review*, 2004.
- [29] T.C. Leïchl  , W. Ye, and M.G. Allen. A sub- μ w micromachined magnetic compass. In *Proceedings IEEE MicroElectroMechanicalSystems*, Kyoto, Japan, January 2003.
- [30] J.E. Lenz. A review of magnetic sensors. *Proceedings of the IEEE*, 78(6), June 1990.
- [31] J.-S. Lin and I. Kanellakopoulos. Nonlinearities enhance parameter convergence. *IEEE Transactions on Automatic Control*, 43(2):204–222, 1998.
- [32] V.J. Logesswaran, F.E.H. Tay, M.L. Chan, F.S. Chau, and Y.C. Liang. A 2f method for the measurement of resonant frequency and q-factor of micromechanical transducers. In *Proceedings of the SPIE*, volume 4755, pages 584–593, Cannes, France, 2002.
- [33] H. Luo, G.K. Fedder, and L.R. Carley. A 1mg lateral cmos-mems accelerometer. In *Proceedings IEEE 13th Annual International Conference on Micro Electro Mechanical Systems*, pages 505–507. IEEE, 2000.
- [34] N.D. Masters and L.L. Howell. A self-retracting rully compliant bistable micromechanism. *Journal of Microelectromechanical Systems*, 12(3):279–281, June 2003.
- [35] Matlab ver. 6.5. The Mathworks, Inc., 2002.
- [36] M. Napoli, B. Bamieh, and K. Turner. Mathematical modeling, experimental validation and observer design for a capacitively actuated microcantilever. In *Proceeding of the 2003 American Control Conference*, volume 5, pages 3732–3737, Denver,Co, June 2003. American Automatic Control Council, IEEE.
- [37] A.H. Nayfeh and D.T. Mook. *Nonlinear Oscillations*. John Wiley & Sons, Inc., 1979.
- [38] C.T.-C Nguyen. Frequency-selective mems for miniaturized low-power communication devices. *IEEE Transactions on Microwave Theory and Techniques*, 1999.

- [39] R.L. Norton. *Machine Design: An Integrated Approach*. Prentic-Hall, 1996.
- [40] C.C. Painter and A.M. Shkel. Active structural error suppression in mems vibratory rate integrating gyroscopes. *IEEE Sensors Journal*, 3(5):595–606, 2003.
- [41] P.S. Riehl, K.L. Scott, R.S. Muller, R.T. Howe, and J.A. Yasaitis. Electrostatic charge and field sensors based on micromechanical resonators. *Journal of Microelectromechanical Systems*, 12(5):577–589, Oct. 2003.
- [42] A. Salvatori. The superharmonic bifurcational and chaotic behavior of a nonlinear s.d.o.f. dynamical system. In *Fourteenth Engineering Mechanics Conference*. ASCE, 2000. <http://www.ce.utexas.edu/em2000>.
- [43] Y.H. Seo, K.-H. Han, and Y.-H. Cho. New plasma hall effect magnetic sensors: Macrosensors versus micro sensors. *Sensors and Actuators, A:Physical*, 2001.
- [44] G. Stemme. Resonant silicon sensors. *Journal of Micromechanics and Microengineering*, 1(2), 1991.
- [45] Su-8: A thick photo-resist for mems, 2003.
- [46] M. Tabib-Azar. *Microactuators: Electrical, Magnetic, Thermal, Optical, Mechanical, Chemical & Smart Structures*. Kluwer Academic Publishers, 1998.
- [47] K.L. Turner and W. Zhang. Design and analysis of a dynamic mem chemical sensor. In *Proceedings of the American Control Conference*, volume 2, pages 1214–1218, Arlington, Va, 2001. American Automatic Control Council.
- [48] J.R. Vig and Y. Kim. Noise in microelectromechanical system resonators. *IEEE Transactions on Ultrasonics, Ferroelectrics and Frequency Control*, 46(6):1559–1595, Nov. 1999.
- [49] N. Yamaki and A. Mori. Non-linear vibrations of a clamped beam with initial deflection and initial axial displacement, part i: Theory. *Journal of Sound and Vibration*, 71(3):333–346, 1980.
- [50] K.Y. Yasumura, T.D. Stowe, E.M. Chow, T. Pfafman, and T.W. Kenny. A study of microcantilever quality factor. In *Technical Digest: Solid-State Sensor and Actuator Workshop*, pages 65–70, Hilton Head, SC, June 1998.
- [51] W. Ye, S. Mukherjee, and N.C. MacDonald. Optimal shape design of an electrostatic comb drive in microelectromechanical systems. *Journal of Microelectromechanical Systems*, 7(1):16–26, March 1998.
- [52] J.K. Yee, H.H. Yang, and J.W. Judy. Dynamic response and shock resistance of ferromagnetic micromechanical magnetometers. In *15th IEEE International Conference on Micro Electro Mechanical Systems*, pages 308–311, Las Vegas, NV, 2002. IEEE: Robotics and Automation Society.